

AD-A276 159



(2)

EXPERIMENTAL AND THEORETICAL STUDIES OF HYDROGENATED  
AMORPHOUS SEMICONDUCTOR ALLOYS AND SUPERLATTICES

FINAL REPORT

by

Zvi S. Weisz and Manuel Gomez

University of Puerto Rico,  
Rio Piedras, PR 00931

February 4, 1994

for

U.S. ARMY RESEARCH OFFICE

GRANT NUMBER: DAAL03-89-G-0114

**S** DTIC  
ELECTE  
FEB 24 1994  
**A**

94-05999



DTIC QUALITY INSPECTED 8

APPROVED FOR PUBLIC RELEASE;  
DISTRIBUTION UNLIMITED.

94 2 26 207

## REPORT DOCUMENTATION PAGE

Form Approved  
OMB No. 0704-0188

Public reporting burden for this collection of information is estimated to average 1 hour per response, including the time for reviewing instructions, searching existing data sources, gathering and maintaining the data needed, and completing and reviewing the collection of information. Send comments regarding this burden estimate or any other aspect of this collection of information, including suggestions for reducing this burden, to Washington Headquarters Services, Directorate for Information Operations and Reports, 1215 Jefferson Davis Highway, Suite 1204, Arlington, VA 22202-4302, and to the Office of Management and Budget, Paperwork Reduction Project (0704-0188), Washington, DC 20503.

1. AGENCY USE ONLY (Leave blank)		2. REPORT DATE	3. REPORT TYPE AND DATES COVERED	
		Feb. 1994	Final 15 Sep 89-14 Dec 93	
4. TITLE AND SUBTITLE			5. FUNDING NUMBERS	
Experimental and Theoretical Studies of Hydrogenated Amorphous Semiconductor Alloys and Superlattices			DAAL03-89-G-0114	
6. AUTHOR(S)				
Zvi S. Weisz and Manuel Gomez				
7. PERFORMING ORGANIZATION NAME(S) AND ADDRESS(ES)			8. PERFORMING ORGANIZATION REPORT NUMBER	
Univ. of Puerto Rico Rio Piedras, PR 00931				
9. SPONSORING / MONITORING AGENCY NAME(S) AND ADDRESS(ES)			10. SPONSORING / MONITORING AGENCY REPORT NUMBER	
U.S. Army Research Office P.O. Box 12211 Research Triangle Park, NC 27709-2211			ARO 25715.6-MS-SAH	
11. SUPPLEMENTARY NOTES				
The views, opinions and/or findings contained in this report are those of the author(s) and should not be construed as an official Department of the Army position, policy, or decision, unless so designated by other documentation.				
12a. DISTRIBUTION / AVAILABILITY STATEMENT			12b. DISTRIBUTION CODE	
Approved for public release; distribution unlimited.				
13. ABSTRACT (Maximum 200 words)				
<p>We developed the photocarrier grating technique for carrier mobility-lifetime products (<math>\mu\tau</math>) measurements. Applying this technique to hydrogenated amorphous silicon (a-Si:H), we obtained <math>\mu\tau</math> values ranging from <math>10^{-8}</math> to <math>10^{-5}</math> <math>\text{cm}^2/\text{V}</math> for the majority and <math>10^{-10}</math> - <math>10^{-8}</math> for the minority carrier. This served as a basis for quality evaluation of materials prepared by different methods. We established that the dominant recombination mechanism is the "defect pool" mechanism. Using the semiconductor-electrolyte system, we studied the density of localized states in a-Si:H and compared it to crystalline silicon. We found in a-Si:H an overall density of bulk states of <math>10^{18} \text{ cm}^{-3}</math>. In crystalline Si only surface states were found, of an overall density of <math>10^{12} \text{ cm}^{-2}</math>. The surface states are centered around 0.2 eV below the conduction band edge. The transport properties of two other disordered systems that may be relevant to a-Si:H were studied theoretically. These systems consists of metal cermets and of small colloidal suspensions.</p>				
14. SUBJECT TERMS			15. NUMBER OF PAGES	
			16. PRICE CODE	
17. SECURITY CLASSIFICATION OF REPORT		18. SECURITY CLASSIFICATION OF THIS PAGE	19. SECURITY CLASSIFICATION OF ABSTRACT	20. LIMITATION OF ABSTRACT
UNCLASSIFIED		UNCLASSIFIED	UNCLASSIFIED	UL

**EXPERIMENTAL AND THEORETICAL STUDIES OF HYDROGENATED  
AMORPHOUS SEMICONDUCTOR ALLOYS AND SUPERLATTICES**

**FINAL REPORT**

by  
**Zvi S. Weisz and Manuel Gomez**

**University of Puerto Rico,  
Rio Piedras, PR 00931**

**February 4, 1994**

for  
**U.S. ARMY RESEARCH OFFICE**

**GRANT NUMBER: DAAL03-89-G-0114**

Accession For	
NTIS	CR & I
DTIC	TAB
Unannounced	
Justification	
By	
Distribution /	
Availability Codes	
Dist	Avail and/or Special
A-1	

**APPROVED FOR PUBLIC RELEASE;  
DISTRIBUTION UNLIMITED.**

## **EXPERIMENTAL AND THEORETICAL STUDIES OF HYDROGENATED AMORPHOUS SEMICONDUCTOR ALLOYS AND SUPERLATTICES**

### **A. STATEMENT OF THE PROBLEMS STUDIED**

The electronic properties, band structure, and the distribution of localized states in semiconductors, thin-film hydrogenated amorphous Si and its alloys, and disordered systems.

### **B. SUMMARY OF THE MOST IMPORTANT RESULTS**

#### **Study of Bulk and Surface Recombination in a-Si:H**

Using our combined photoconductivity and diffusion length measurement technique we have derived bulk mobility-lifetime products and the surface recombination velocity of both types of carriers in undoped hydrogenated amorphous silicon (a-Si:H) deposited by glow discharge decomposition of silane. The study was based on comparison of the experimental data with the classical theory of semiconductors. The measurements were carried out as a function of light intensity with two types of illumination; a He-Ne (7328 Å) laser, and a He-Cd (4420 Å) laser. The results, at a light intensity of  $25 \text{ mW/cm}^2$ , have shown that for the same photon flux the He-Ne laser yields a photoconductivity 15 times larger than the one achieved with the He-Cd laser. On the other hand, the corresponding ratio for the minority carrier mobility-lifetime product was lower only by a factor of two. These results were interpreted assuming surface recombination velocities of the order of 10-100 cm/sec and a moderate improvement in the quality of the material with film thickness. We have also found that the surface recombination velocity may be quite different for the two surfaces of a film, indicating that growth conditions play an important role in the electronic structure of the surface. From the illumination intensity dependence we were able to derive information regarding the states distribution on these surfaces.

Measurements of the above photoelectronic properties as a function of temperature has revealed information on the temperature shift of the electrons' and holes' quasi-Fermi levels. For example, we have found that while the photoconductivity is almost insensitive to temperature variations around room temperature, the mobility-life time product of the minority carriers has an activation energy of  $E_a=0.11 \text{ eV}$ . Under some assumptions on the material parameters, these results may yield the density of states in some energy intervals of the pseudogap of the materials.

Within the framework of the present study we have developed the theory of the photocarrier grating (PCG) technique and utilized it to interpret our experimental results on a-Si:H. This has enabled the derivation of the mobility-lifetime ( $\mu\tau$ ) products of both types of carriers in undoped and doped a-Si:H. Previous experimental works using this technique were limited to the derivation of the  $\mu\tau$  products of the minority carriers only. Furthermore, we were able to develop a criterion under which the application of the PCG technique yields indeed the value of the minority carriers  $\mu\tau$  product. We also showed that this criterion is not always met. Hence, we made the PCG a routine tool for the evaluation of the microscopic photoelectronic properties of a-Si:H.

In our studies we have also used the photocarrier grating technique for the first time in the high electric-field regime. The results were shown to confirm the so far unproven theoretical predictions for this regime. We have demonstrated that by application of the PCG technique in the high field regime, accurate values for the ratio of the two carriers  $\mu\tau$  products can be deduced. This is in contrast with the fact that their sum cannot be derived accurately from the measurement of photoconductivity because one cannot determine accurately the carrier generation rate. Combining the ratio determined by the high-field PCG, with the low field data, yields then accurate values for the mobility - lifetime products of both carriers.

In the low electric-field regime the many reports concerning the utilization of the PCG technique have assumed that ambipolar transport takes place in the PCG when it is applied to a-Si:H. This assumption, which is decisive in the interpretation of the experimental results in terms of the ambipolar diffusion length, has not been tested so far. In our work we developed the first corresponding ambipolarity criterion and have demonstrated that while ambipolarity is maintained in device quality a-Si:H it does not apply to lightly doped or poor quality a-Si:H materials. The results were shown to confirm our theoretical suggestion that the observed ambipolarity in a-Si:H is due to trapping effects.

The relation between the inhomogeneity along the direction of the film growth and the surface recombination velocity has been studied in device quality a-Si:H films. It is found that the material is electronically inhomogeneous "deep" into the bulk up to a typical depth of the order of 1000 Å. Hence, the surface recombination velocity in a-Si:H is not a true surface property as in crystalline semiconductors. This result is important for modeling electronic devices, since these are typically only a few thousand angstroms thick.

Using the deposition temperature as a control parameter for variation of the dangling bond concentration and the relative position of the dark Fermi level, the photoconductivity and the ambipolar diffusion length were measured on samples prepared

by sputtering and glow discharge at different temperatures. This has enabled us to differentiate between different suggested models for the energetic position of the recombination centers, as well as the recombination kinetics in a-Si:H. It was found that the "defect-pool" model yields the best description of the system..

Finally, we were able to achieve the first combined application of the Metal Oxide Semiconductor and the Photocarrier Grating configurations. This combination enabled us the first *simultaneous* study of the two carriers mobility-lifetime products and their light intensity exponents as a function of the position of the Fermi level, in *undoped* a-Si:H. We found that anticorrelations and correlations prevail between these two sets of quantities. The conclusion we derive from these behaviors is also that the defect pool model accounts for the phototransport data much better than any other model.

We have studied the Raman spectrum in a-Si:H as a function of film thickness in order to follow variations in the degree of order in the amorphous network. The results indicate an improvement of the order with sample thickness. There are considerable differences between the optical phonon modes at the surface and in the bulk which we attribute to the fact that the surface layer is less ordered than the bulk. These results are in agreement with our former observation of improvement of the photoelectronic properties with the film thickness. More recently we have studied a-Si<sub>x</sub>C<sub>1-x</sub>:H alloys and found quite surprisingly that the silicon network order increases with carbon content. Furthermore, due to the possibility of bandgap tuning by carbon content and/or variation of laser wavelength excitation, we found a resonant Raman effect.

### **The Semiconductor/Electrolyte Interface**

#### **Non-Parabolicity in the Lowest Conduction Band of CdS.**

Pulse measurements on the semiconductor/electrolyte system were used to induce and study space-charge layers at the semiconductor surface. Measurements on CdS show that the free-electron-like lowest conduction band in hexagonal CdS is highly non-parabolic. A simple model for the structure of this band, which assumes parabolicity up to 0.125 eV above the band edge and a linear dependence of the energy on the wavevector at higher energies, accounts well for the experimental results. The density-of-states function that emerges from these results is compatible with reported theoretical calculations.

In addition, the measurements indicate that surface states are practically absent at the CdS surface in contact with the electrolyte. They also shed light on the process of charge leakage across the CdS/electrolyte interface, leakage that occurs mostly when strong accumulation layers are induced.

### Surface States at the Silicon/Electrolyte Interface.

Pulse measurements on the Si-electrolyte interface were used to study surface states at the silicon surface. We find that for CP-4 etched silicon, surface states exist in the upper half of the energy gap, with a total density of about  $10^{12} \text{ cm}^{-2}$ . Addition of a minute amount of hydrofluoric acid to the electrolyte reduces their density by one order of magnitude. It has been reported that the surface recombination velocity on an oxidized surface is considerably lowered by an HF treatment, suggesting a corresponding reduction in the density of surface recombination centers. Our results, however, constitute the first direct evidence for such a reduction. It appears that Si-H bonds are formed at the interface, just as has been reported for an HF-treated free Si surface. Very likely, the formation of such bonds leaves, on both types of surface, considerably fewer dangling bonds and hence considerably fewer surface states.

### Study of Density of States in a-Si:H.

Pulsed measurements on the solid-electrolyte system, which proved very useful in the study of crystalline semiconductors, have been found to be equally effective when applied to hydrogenated amorphous Si films. Here, as well, the a-Si:H/electrolyte interface is essentially blocking to current flow and, as a result, surface space-charge layers, ranging from large depletion to very strong accumulation conditions, have been induced and studied. Measurements in the depletion range under illumination yielded directly the total density of *occupied* states in the entire energy gap. This is very useful in obtaining a quick and reliable assessment of the quality of the amorphous films. In high-grade films we find that the total density of occupied states is around  $10^{18} \text{ cm}^{-3}$ . The data in the accumulation range, on the other hand, provide useful information on *unoccupied* states near the conduction band edge. The blocking nature of the amorphous Si/electrolyte interface was utilized also to apply a sweep-out technique for an accurate determination of  $\mu\tau$ , the product of the electron mobility and lifetime, even when this value is very low. In a rather poor-quality film, for example, we find  $\mu\tau$  to be  $5 \times 10^{-8} \text{ cm}^2/\text{V}$ .

### Cermets and Metallic Colloidal Suspensions

#### Tunneling and Percolation Behaviour in Granular Metals.

The nature of the percolation process in granular metals was examined for the first time by a computer simulation of a system of metallic grains embedded in an insulating matrix. Assuming that the intergrain conduction is due to quantum mechanical tunneling it was found that a percolation-like critical behavior of the conductivity is obtained, but that a percolation *universal* behavior will be found only in a very special case. In contrast, the

behavior of the electrical noise does not deviate substantially from the universal one. Comparison of these results with experimental observations suggests that in the metallic range, both transport properties are controlled by the continuous metallic network rather than by intergrain tunneling. We propose that the metallic network resembles the previously studied system of "inverted random voids".

#### Local Fields Around Clusters of Prolate Spheroids.

$T_-$ -matrix formalism was used to calculate local electric fields around clusters of prolate spheroids in the long wavelength regime. The calculations are performed as a function of interparticle distance as well as the angle of orientation. The observed red shifts in the resonant wavelengths of the characteristic peaks are shown to obey an exponential relationship as a function of interparticle separation and a sinusoidal relationship as a function of angle of rotation of the spheroid. The behavior of the cluster was examined and the two effects, of separation and rotation, were compared.

The results of these calculations were applied to cermet materials and metallic colloidal suspensions in alkali halide crystals and their effect on enhanced Raman scattering was discussed.

#### C. LIST OF PUBLICATIONS

1. Non-Parabolicity in the Lowest Conduction Band of CdS, S.Z. Weisz, J. Penalbert, A. Many, S. Trokman and Y. Goldstein. *J. Phys. Chem. Solids*, **51**, 1067, (1990).
2. Tunneling and Percolation Behavior in Granular Metals, I. Balberg, N. Wagner, Y. Goldstein and S.Z. Weisz., *Mat. Res. Soc. Symp. Proc.*, **195**, 233, (1990).
3. Acurate Determination of the Two Carriers Steady State Mobility-Lifetime Products in Hydrogenated Amorphous Silicon. I. Balberg and S.Z. Weisz. *J. Appl. Phys.* **70**, 2204, (1991).
4. Indentification of Non-Ambipolar Transport in the Application of a Photocarrier Grating to Hydrogenated Amorphous Silicon. I. Balberg and S.Z. Weisz. *J. Appl. Phys. Lett.* **59**, 1726 (1991).
5. High-Energy LMM Auger Transitions. S.Z. Weisz, M. Gomez, O. Resto, A. Many, and Y. Goldstein. *Journal of Surface and Interface Analysis*, **19**, 264 (1992).
6. Theoretical and Experimental Developments in the Determination of the Minority Carrier Properties in Low Mobility Semiconductors. I. Balberg and S.Z. Weisz. *Proc. of the 14th Int'l. Conf. on the Physics of Semiconductors*, Beijing (World Scientific, Singapore, 1993), p. 1747.

7. Lineshapes and Yields of High-Energy Auger Lines. S.Z. Weisz, M. Gomez, O. Resto, M.H. Farias, Y. Goldstein and A. Many. *J. Phys.: Condens. Matter*, **5**, A169 (1993).
8. Surface States at the Silicon/Electrolyte Interface. A. Many, M. Wolovelsky, Y. Goldstein, S.Z. Weisz and M. Gomez. *J. Phys.: Condens. Matter*, **5**, A133 (1993).
9. Studies of a-Si:H Using the Solid/Electrolyte System. Y. Goldstein, A. Many, J. Penalbert, W. Munoz, M. Gomez and S.Z. Weisz. *Mat. Res. Soc. Symp. Proc.* **297**, 351 (1993).
10. Inhomogeneity in the Network Disorder of Device Quality a-Si:H. I. Balberg, R. Katiyar, G. Morell and S.Z. Weisz. *Proc., Mat. Res. Soc. Symp. Proc.* **297**, 321 (1993).
11. T-matrix Approach for Calculating Local Fields Around Clusters of Rotated Spheroids. W. Vargas, L. Cruz, L.F. Fonseca, and M. Gomez. *Appl. Optics* **32**, 2164 (1993).
12. Yields, Sensitivities and Natural Lineshapes of High-Energy Auger Lines: II. Ta, W, Pt, and Bi. Y. Goldstein, A. Many, S.Z. Weisz, M. Gomez, O. Resto and M.H. Farias. *Journal of Electron Spectroscopy and Related Phenomena* (In press).
13. The dependence of the two Carrier Mobility-Life Time Products on the Positions of the Fermi Level in a-Si:H. Y. Lubianiker, I. Balberg, S.Z. Weisz and M. Gomez. *Journal of Non-Crystalline Solids* (In press).
14. Study of Density of States in a-Si:H Using the Solid/Electrolyte System. A. Many, Y. Goldstein, S.Z. Weisz, J. Penalbert, W. Munoz, and M. Gomez. *Journal of Non-Crystalline Solids* (In press).
15. Mobility-Lifetime Products in Glow Discharge and RF Sputter Deposited a-Si:H. H. Farias, A. Roche, S.Z. Weisz, H. Jia, J. Shinar, Y. Lubianiker and I. Balberg. *Proc., Mat. Res. Soc. Symp. Proc.* (April 1994, in press).
16. Existing Frequency-Dependent Raman Scattering in a-Si:H. G. Morell, R.S. Katiyar, S.Z. Weisz and I. Balberg. *Mat. Res. Soc. Symp. Proc.* (April 1994, in press).
17. Infrared and Raman Studies on a-Ge<sub>1-x</sub>Sn<sub>x</sub>H Thin Films. E. Ching Frado, R.S. Katiyar, W. Munoz, O. Resto and S.Z. Weisz. Submitted to *Phys. Rev. B*.

#### D. LIST OF PARTICIPATING SCIENTIFIC PERSONNEL

Zvi S. Weisz, Project Director

Manuel Gomez-Rodriguez, Additional Principal Investigator

Ram S. Katiyar

## NON-PARABOLICITY IN THE LOWEST CONDUCTION BAND OF CdS

S. Z. WEISZ,<sup>†</sup> J. PENALBERT,<sup>†</sup> A. MANY,<sup>‡</sup> S. TROKMAN<sup>‡</sup> and Y. GOLDSTEIN<sup>‡</sup>

<sup>†</sup>Department of Physics, University of Puerto Rico, Rio Piedras, PR 00931

<sup>‡</sup>Racah Institute of Physics, The Hebrew University, Jerusalem, Israel

(Received 26 February 1990; accepted 15 March 1990)

**Abstract**—Pulse measurements on the CdS/electrolyte system are used to induce and study space-charge layers at the CdS surface. Such measurements show that the free-electron-like lowest conduction band in hexagonal CdS is highly non-parabolic. A simple model for the structure of this band, which assumes parabolicity up to 0.123 eV above the band edge and a linear dependence of the energy on the wavevector at higher energies, accounts well for the experimental results. The density of states function that emerges from these results is compatible with reported theoretical calculations.

In addition, the measurements indicate that surface states are practically absent at the CdS surface in contact with the electrolyte. They also shed light on the process of charge leakage across the CdS/electrolyte interface, leakage that occurs mostly when strong accumulation layers are induced.

**Keywords:** CdS, band structure, surface, quantum wells.

### INTRODUCTION

Band structure calculations for hexagonal CdS [1, 2] indicate the presence of a nearly-spherical, free-electron-like lowest conduction band extending up to about 1.8 eV above the band edge. While these calculations provide a broad, overall picture of the band structure, little detail can be gleaned about the precise shape of the lowest conduction band. Experimental results such as those derived from optical measurements are also lacking. In this paper we make use of the semiconductor/electrolyte (S/E) system to study the surface space-charge layer of CdS. The higher reaches of the lowest conduction band become occupied in very strong accumulation layers. Such layers can be induced in the S/E system provided pulsed [3-5] rather than d.c. biases are employed. Electrochemical processes are then largely circumvented, permitting the derivation of the physical characteristics of the surface with minimal involvement of the rather complex surface chemistry. Similarly to the case of ZnO [6, 7] and Si [5], accumulation layers of surface electron densities as high as  $10^{14} \text{ cm}^{-2}$  can be induced and studied at the CdS surface. Analysis of the data obtained for this range indicates that the lowest conduction band is highly non-parabolic, and provides a fairly good idea as to the shape of the band up to about 1.5 eV above the conduction-band edge.

The S/E interface is not perfectly blocking and some charge leaks between the two phases, especially when strong accumulation layers are induced at the CdS surface. The pulse measurements yield a detailed characterization of the leakage process. They also indicate that surface states are practically absent at

the CdS surface when in contact with the electrolytes used.

### THE SPACE-CHARGE LAYER AND THE SEMICONDUCTOR/ELECTROLYTE INTERFACE

In this section we review briefly the characteristics of the semiconductor surface space-charge layer [8] and consider several features of the semiconductor/electrolyte system, stressing those points that are directly related to our present work. We consider a homogeneous, non-degenerate, *n*-type semiconductor having fully ionized donors. For depletion and accumulation layers (one-carrier system), the surface space-charge density (per unit area) can be expressed as

$$Q_x = -qN_s \quad (1)$$

where  $q$  is the absolute magnitude of the electronic charge and  $N_s$  is the surface electron density. By definition,  $N_s$  is zero under flat-band conditions, positive for accumulation layers and negative for depletion layers. The space-charge capacitance is given by

$$C_x = |Q_x/V_s| \quad (2)$$

where  $V_s$  is the potential barrier height at the surface. The effective charge distance  $L_c$ , which represents the effective width of the space-charge layer, is given by the expression

$$C_x = \kappa\epsilon_0/L_c \quad (3)$$

where  $\kappa$  is the relative dielectric constant of the semiconductor and  $\epsilon_0$  is the permittivity of free space. First integration of Poisson's equation leads to [8]

$$N_s = \pm (\kappa\epsilon_0 n_s k_B T/q^2)^{1/2} F_s \quad (4)$$

where the positive sign applies to accumulation layers, the negative sign to depletion layers;  $n_b$  is the electron bulk concentration,  $k_B$  is Boltzmann's constant and  $T$  the absolute temperature.

In the general case, the function  $F$ , is given by [3]

$$F_i = \sqrt{2} \left\{ \int_0^\infty [N(E)/n_b] \left[ v_i + \ln \left( \frac{1 + \exp(E/k_B T + w_b - v_i)}{1 + \exp(E/k_B T + w_b)} \right) \right] dE - v_i \right\}^{1/2}. \quad (5)$$

where  $N(E)$  is the density of states in the conduction band,  $w_b = W_b/k_B T$ ,  $W_b$  being the energy separation between the Fermi level and the conduction-band edge in the bulk (positive for the  $n$ -type sample being considered), and  $v_i = qV/k_B T$  is the so-called dimensionless barrier height.

For parabolic conduction bands the function  $F$ , assumes the simpler form

$$F_i = \sqrt{2} \left\{ (4/3)\pi^{-1/2} \exp(w_b) \int_0^\infty x^{1/2} \times [1 + \exp(x + w_b - v_i)]^{-1} dx - v_i - 1 \right\}^{1/2}. \quad (6)$$

For strong accumulation layers, however, in which the conduction-band edge lies well below the Fermi level, taking the conduction band as parabolic may not always be a good approximation. This is definitely the case in CdS and one should use eqn (5), substituting for  $N(E)$  the actual density of states in the (non-parabolic) conduction band.

Another important factor that needs to be considered in strong accumulation layers is associated with the spatial confinement of the electron gas. When the effective charge distance  $L_c$  becomes comparable to or less than the de Broglie wavelength of a conduction electron, quantization effects set in. The classical calculations reviewed above may no longer be adequate, the less so the stronger the accumulation layer (larger  $N_i$ , smaller  $L_c$ ). One should then solve self-consistently Poisson's and Schrödinger's equations [6, 7, 9, 10]. Unfortunately, such calculations have not been carried out for CdS. However, the similarity of the values of the dielectric constant and the effective mass (at the bottom of the band) in CdS ( $\kappa = 9.02$  and  $m/m_0 = 0.205$ , where  $m_0$  is the free-electron mass) and ZnO ( $\kappa = 8.5$ ,  $m/m_0 = 0.25$ ) permits the use of the ZnO calculations [6, 7] for CdS without introducing too large an error.

For non-degenerate surface conditions, corresponding to depletion and weak accumulation layers, only the bottom of the band is involved and this can safely be taken as parabolic. Equation (6) then reduces, to a good approximation, to the simpler expression

$$F_i = \sqrt{2} \{ \exp(v_i) - v_i - 1 \}^{1/2}. \quad (7)$$

The semiconductor/electrolyte system considered here consists of a semiconductor surface in contact with an indifferent electrolyte such as an aqueous solution of a salt [KCl or Ca(NO<sub>3</sub>)<sub>2</sub>]. By biasing the electrolyte with respect to the semiconductor, charge can be induced electrostatically at the semiconductor surface. This is made possible by the essentially blocking nature of the S/E interface, which largely prevents charge transfer between the two phases. Such blocking is due to the fact that in the electrolyte the negative ions (such as Cl<sup>-</sup>) usually lie well below, and the positive ions (such as K<sup>+</sup>) well above, the semiconductor band edges [11]. Hence, in an  $n$ -type semiconductor being considered, for a negatively biased electrolyte, the negative ions pile up against the interface without being able to transfer electrons into the conduction band, and a depletion layer is induced. In the reverse polarity, positive ions pile up against the interface and an accumulation layer is induced. The induced charge is in general distributed between the surface space-charge region and surface states (if present). In the absence of a foreign layer (such as an oxide) at the semiconductor interface, the applied bias drops across three adjacent regions [8, 12]: the space-charge layer at the semiconductor surface, and the Helmholtz and Gouy layers in the electrolyte. Of these three layers, the latter two are much thinner than the first, at least under pulsed bias conditions, so that practically the entire applied bias drops across the semiconductor space-charge layer. This is evidenced by space-charge capacitance measurements on metal/electrolyte interfaces [3]. Hence the measured bias represents to a very good approximation the change  $\delta V$ , in barrier height  $V$ , across the semiconductor space-charge layer.

In practice, the interface is not perfectly blocking and to a lesser or greater extent some charge leaks across the S/E interface. The leakage charge is usually insignificant when depletion layers are induced (electrolyte biased negatively with respect to the  $n$ -type semiconductor). It becomes appreciable, however, under accumulation conditions, the more so the stronger the induced accumulation layer. It is this leakage that prevents the formation of strong accumulation layers by d.c. biases. By employing our pulse techniques [3-5], on the other hand, it is possible to induce extremely strong accumulation layers not only on CdS but also on a number of other semiconductors, such as Ge [3], Si [5] and ZnO [6, 7], without being hampered by charge leakage. Moreover, these techniques enable a straightforward separation of the different components of the induced charge, so as to obtain the variation of the free space-charge density as well as of the leaked charge and of the occupancy of the interface states with the surface potential barrier. More important still, the use of a limited number of short-duration pulses minimizes electrochemical reactions which may otherwise greatly complicate the interpretation of the data. By the same token, surface damage that usually occurs under

prolonged application of large d.c. biases is largely eliminated.

### EXPERIMENTAL

The samples were cut from single crystal (*n*-type) CdS ingots ranging in resistivity between about 0.1 and 10 ohm-cm. The samples' dimensions were typically  $2 \times 3 \times 0.5$  mm<sup>3</sup>, with the large faces perpendicular to the *c* axis. Following mechanical polishing, each sample was first etched in HCl and then in a solution of  $K_2Cr_2O_7$  in dilute  $H_2SO_4$ , at 90°C, for 10 min. This resulted in a smooth surface with a negligible density of surface states and low leakage currents. An ohmic contact was applied to one of the large surfaces. The wire lead, contact area and the entire sample were masked by epoxy cement, except for a small area ( $\sim 1$  mm<sup>2</sup>) to be exposed to the electrolyte. The exposed area was usually the (000T) face (the "sulfur" face). The CdS sample and a large platinum electrode were immersed in a  $Ca(NO_3)_2$  or

KCl electrolyte. These are represented by the equivalent circuits (to be discussed below) between points A and B in Fig. 1(a) which is a schematic diagram of the experimental arrangement. The pulse generator (Hewlett-Packard type 214A) of internal resistance  $r_p$  ( $= 50 \Omega$ ), can provide positive and negative pulses of up to 100 V in amplitude and 0.05 to 200  $\mu$ s in duration. It is connected to the platinum and semiconductor electrodes (points A and B) via a diode D and a large (0.1-1  $\mu$ F) series capacitor C. The diode polarity is such as to permit rapid charging of the system while the pulse is on and to prevent its discharge through the low-impedance pulse generator after the termination of the pulse. An electronic switch S can short-circuit the Pt electrode to ground at any prescribed time following the termination of the pulse. The residual resistance  $r_s$  of the shorted switch is a few ohms. Short-duration (0.1-10  $\mu$ s) pulses are applied singly, one pulse per data point taken, in order to minimize any electrochemical

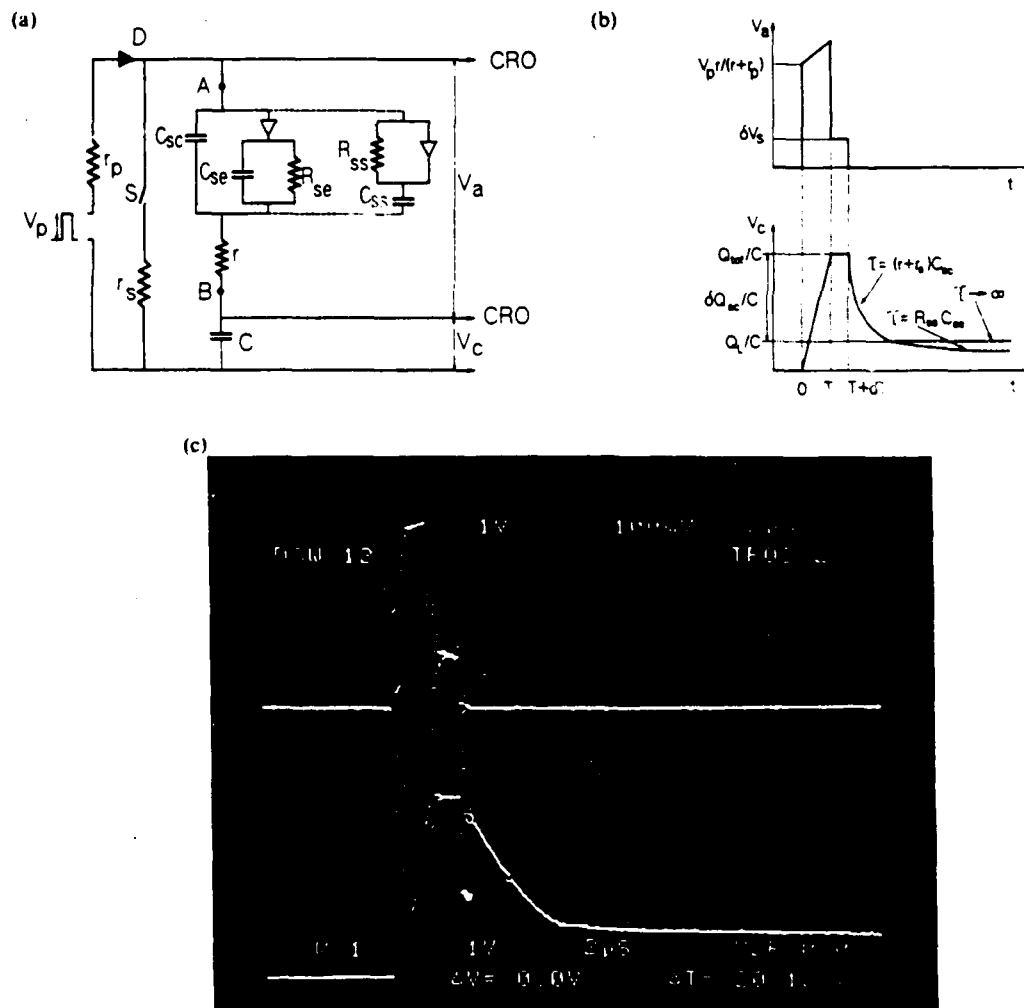


Fig. 1. (a) Circuitry of the experimental arrangement. The sample is simulated (between points A and B) by the space-charge capacitance  $C_{sc}$  and a resistance  $r$  in series, and by the leakage and surface-state equivalent circuits. (b) Schematic representation of expected pulse responses of the voltage drops  $V_a$  and  $V_c$ . (c) Actual pulse response of  $V_a$  (upper trace, 1 V cm<sup>-1</sup>) and  $V_c$  (lower trace, 100 mV cm<sup>-1</sup>) for a CdS/electrolyte interface.

reaction that may take place at the CdS surface. A Tektronix type 7407 CRO is used to monitor the voltage drop  $V_s$  between the Pt electrode (point A) and the ohmic contact of the sample (point B), and the drop  $V_c$  across the series capacitor C. Strictly speaking, the relevant oscillogram is that of the voltage drop  $V'_s$  between a reference electrode and the sample, rather than  $V_s$ . However, the space-charge capacitance at the platinum surface is orders of magnitude larger than that at the semiconductor surface. Hence, only a negligible fraction of the applied bias is expected to drop across the Pt/electrolyte interface, so that the two traces should yield practically identical results. This was indeed checked to be the case by the occasional use [6, 7] of a reference electrode. The magnitude of C is chosen so as to be large compared to the semiconductor surface capacitance, typically by a factor of 10–100. The voltage developed across it ( $V_c$ ) is thus smaller (by the same factor) than the voltage developed across the space-charge layer ( $V_s$ ).

In most cases a space-charge layer already exists at the semiconductor surface, before applying any bias. It is characterized by an equilibrium barrier height  $V_{s0}$  and a space-charge density  $Q_{s0}$ . If surface states are present, there may also be an equilibrium surface-state charge of density  $Q_{s0}$ . The voltage pulse, of amplitude anywhere between 0 and 100 V, charges up the semiconductor surface region. As will be shown in a moment, the voltage drop  $V_s$ , measured just after the termination of the pulse, represents to a very good approximation the change  $\delta V_s = V_s - V_{s0}$  in barrier height induced by the applied pulse. The voltage drop  $V_c$  across the series capacitor C, again measured just after the termination of the pulse, yields the overall charge  $Q'_{tot}$  ( $= CV_c$ ) passing through the system. The charge density  $Q'_{tot}$  (per unit area) is obtained by dividing  $Q'_{tot}$  by the area of the semiconductor surface exposed to the electrolyte.

In general,  $Q'_{tot}$  is made up of three components:

$$Q'_{tot} = \delta Q_s + \delta Q_u + Q_L, \quad (8)$$

where  $\delta Q_s = Q_s - Q_{s0}$  is the change in space-charge density,  $\delta Q_u = Q_u - Q_{u0}$  is the change in surface-state charge density, and  $Q_L$  is the density of the charge leaked across the S/E interface. In terms of electron densities, this can be rewritten as

$$N'_{tot} = \delta N_s + \delta N_u + N_L, \quad (9)$$

where  $N'_{tot}$  is the total electron density passing through the system,  $\delta N_s = N_s - N_{s0}$  is the change in surface electron density,  $\delta N_u = N_u - N_{u0}$  is the density change in surface-state occupation, and  $N_L$  the density of electrons that have leaked across the interface.

We shall now discuss the experimental procedure used in determining the magnitudes of the three components in eqn (8) or (9). This is best done in

terms of the equivalent circuits shown in Fig. 1(a). The ideal case of a perfectly blocking interface and no surface states is simulated simply by a series combination of the space-charge capacitance  $C_s$  and the combined resistance  $r$  of the electrolyte and the underlying semiconductor bulk below the surface. Typically,  $r$  is about  $50 \Omega$ , approximately half of which represents the electrolyte resistance and the other half the sample resistance. Charge leakage across the interface, a prominent process in strong accumulation layers of CdS, is simulated by adding a parallel branch across  $C_s$ , consisting of a diode in series with a parallel combination of a capacitor  $C_u$  and resistor  $R_u$ . As will be shown below, such a circuit is prescribed by the experimental observation that the leakage occurs very fast and remains stored at or near the interface for a long time ( $R_u C_u$ ). Once the charging pulse is terminated, the stored charge does not flow into  $C_s$ , hence the diode. If deep surface states are also present, another equivalent circuit is called for, shown added by the dashed lines in Fig. 1(a). The circuit consists of a resistor  $R_u$  shunted by a diode, both in series with a capacitor  $C_u$ . On the application of a positive pulse, such states charge up very quickly, hence the shunting diode. Their discharge following the termination of the pulse is usually much slower, the more so the deeper they are located energetically and the lower the temperature [8].

It should be noted that the equivalent circuits shown in Fig. 1(a) serve merely as a means of classifying the different processes at the S/E interface on the one hand, and as aids in the understanding of the method of measurement, on the other hand. They do not represent accurately the actual conditions at the interface. In particular, all elements of the equivalent circuits (except  $r$ ) are in reality not passive but voltage dependent.

Figure 1(b) illustrates the time variations of  $V_s$  and  $V_c$  during and following the application of a positive pulse of amplitude  $V_p$ . All the values marked in Fig. 1(b), as well as in the following analysis, correspond to unit surface area. The  $V_s$  scale is expanded by a factor of 100 or so relative to the  $V_c$  scale. The initial rise in  $V_s$  (at  $t = 0+$ ), up to the value  $V_p r / (r + r_s)$ , is very fast (about  $0.01 \mu s$ ) and represents the ohmic voltage drop across  $r$ . Subsequently,  $V_s$  rises much more slowly as  $C_s$ ,  $C_u$  and  $C_u$  charge up. At the termination of the pulse ( $t = T$ ),  $V_s$  drops rapidly to the level  $\delta V_s$ , where  $\delta V_s$  is the voltage developed across  $C_s$ , i.e. the induced change in the potential barrier height. As for  $V_c$ , it rises monotonically up to  $t = T$ , to the level  $Q'_{tot} / C$ , where  $Q'_{tot}$  is the total charge density induced by the pulse, consisting of  $\delta Q_s$ ,  $Q_L$  and  $\delta Q_u$ . The shorting switch S is activated at  $t = T + dT$ , where the interval  $dT$  is very short (usually  $0.1 \mu s$ ), sufficient to permit accurate readings of  $V_s$  and  $V_c$  just after the termination of the pulse. At this point  $V_s$  drops abruptly to practically zero ( $V_c$  being very small compared with  $V_s$ ), and

charge redistribution among  $C_{ss}$ ,  $C_{ss}$ ,  $C_{ss}$  and  $C$  begins to take place. In the first stage, the charge  $\delta Q_{ss}$  stored in  $C_{ss}$  and its equal counterpart in  $C$  discharge relatively fast through  $r + r_s$ . The decay constant associated with this process is approximately  $(r + r_s)C_{ss}$  (since  $C_{ss}$  is small compared with  $C$ ) and is typically several microseconds. In the absence of surface states (as is very nearly the case for CdS),  $V_s$  decays to the value  $Q_L/C$ ,  $Q_L$  being the charge remaining in  $C$  after the fast decay process. This charge will be referred to as a "loss" since, in a sense, it detracts from the induced free space charge. Thereafter,  $V_s$  remains practically constant [solid curve in the bottom diagram of Fig. 1(b)]. Actually, it decays very slowly (0.1–1 s) through the input resistance of the CRO. If, on the other hand, surface states are present and there is no leakage,  $V_s$  decays with the surface-state time constant of approximately  $R_{ss}C_{ss}$  [dashed curve in the bottom diagram of Fig. 1(b)]. In this process, electrons trapped in the surface states by the charging pulse are thermally re-emitted into the conduction band. If both leakage and surface states are present,  $V_s$  first decays rapidly to the value  $(\delta Q_{ss} + Q_L)/C$ . Subsequently it decays with the time constant  $R_{ss}C_{ss}$  to the level of  $Q_L/C$  and thereafter remains practically constant. This behavior enables the separate determination of the three components in eqn (8) that make up the total induced charge density  $Q_{tot}$ . As pointed out above, the surface-state component is essentially absent in CdS.

Typical oscilloscograms illustrating the actual pulse response of the CdS/electrolyte interface for an applied positive pulse (induced accumulation layer) are displayed in Fig. 1(c). The upper and lower traces depict the time variation of  $V_s$  and  $V_c$ , respectively. They are seen to be very similar to the corresponding schematic diagrams in Fig. 1(b), indicating that the models discussed above do indeed provide a realistic description of the S/E interface. As expected, however, the fast decay process of  $V_s$  following the

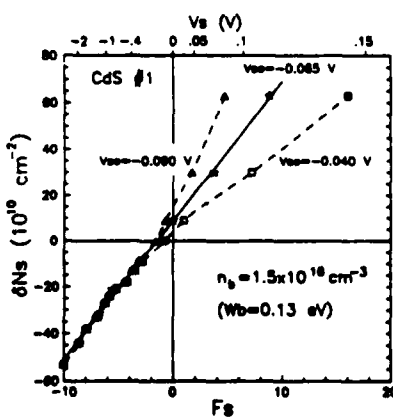


Fig. 2. Change  $\delta N_s$  in surface electron density against  $F_s$  in depletion and moderate accumulation layers. Straight line (solid) corresponds to  $V_s = -0.065$  V, dashed curves to  $V_s = -0.065$  V  $\pm$  0.025 V. Corresponding values of the barrier height are marked off at the upper abscissa.

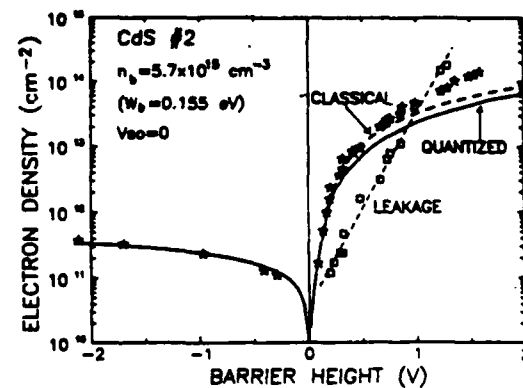


Fig. 3. Electron density vs barrier height. Stars represent the free electron density  $N_s$  for a sample with a relatively low electron bulk concentration  $n_b$ . The classical curve (dashed) is calculated on the assumption of a parabolic conduction band throughout [eqns (4) and (6)]. The solid curve ("quantized") is based on self-consistent calculations carried out for ZnO. (In the depletion range,  $V_s < 0$ ,  $N_s$  is negative and the plot is that of  $-N_s$ .) The squares represent the leakage electron density  $N_L$ .

activation of the shooting switch is not exponential, since  $C_{ss}$  in the actual S/E interface is not a passive element but voltage dependent. This does not interfere at all with the measurement of  $\delta V_s$ ,  $\delta N_s$ ,  $\delta N_{ss}$  and  $N_L$ , and the results to be presented below were obtained precisely as described in connection with Fig. 1(b). It should be noted that the fast decay in  $V_s$  is characterized by a decay time of 2 to 3  $\mu$ s, just the value to be expected from the discharge of the free electrons in the accumulation layer previously induced by the applied pulse [ $(r + r_s)S\delta Q_{ss}/\delta V_s$ ,  $S$  being the area of the CdS surface in contact with the electrolyte]. Accordingly, we identify the amplitude of the fast component as representing the induced change  $\delta Q_{ss}$  in free space-charge density. The subsequent, much slower decay in the  $V_s$  trace (decay time in the millisecond range) has a low amplitude, signifying the low density of surface states (less than  $10^{10}$  cm $^{-2}$ ). This is followed by an essentially non-decaying component representing the leakage charge. The non-decaying component cannot be seen on the scale of Fig. 1(c).

## RESULTS AND DISCUSSION

The results to be reported are based on the analysis of oscilloscope traces of the type shown in Fig. 1(c) above. Under equilibrium conditions, a depletion layer usually exists at the CdS surface in contact with the electrolyte. Since the measurements described above yield directly only the changes  $\delta N_s = N_s - N_{s0}$  in the surface electron density as a function of  $\delta V_s = V_s - V_{s0}$ , the first task is to determine the equilibrium barrier height  $V_{s0}$ . Using eqn (4) one can write

$$\delta N_s = \pm (\kappa \epsilon_0 n_b k_b T / q^2)^{1/2} F_s (V_{s0} + \delta V_s) - N_{s0}. \quad (10)$$

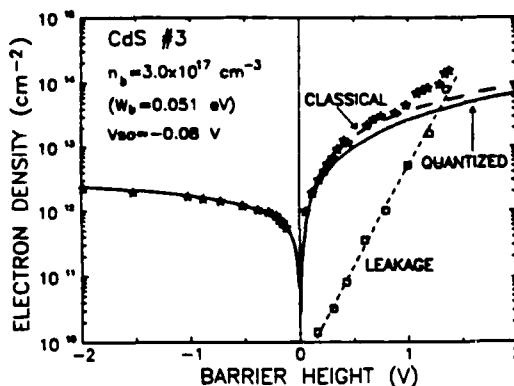


Fig. 4. Electron density vs barrier height. Stars represent the free electron density  $N$ , for a sample with a high electron bulk concentration  $n_b$ . The classical curve (dashed) is calculated on the assumption of a parabolic conduction band throughout [eqns (4) and (6)]. The solid curve ("quantized") is based on self-consistent calculations carried out for ZnO. (In the depletion range,  $V < 0$ ,  $N$ , is negative and the plot is that of  $-N$ .) The squares represent the leakage electron density  $N_L$ .

For depletion and weak (non-degenerate) accumulation layers,  $F_s(V_{s0} + \delta V_s)$  can be evaluated from the simpler expression given by eqn (7). A plot of the  $\delta N_s$  data against the calculated values of  $F_s$  should yield a straight line only if the correct value of  $V_{s0}$  is chosen in the calculation of  $F_s$ . A simple computer program has been set up to so determine  $V_{s0}$ . The results are shown in Fig. 2, where the choice of  $V_{s0} = -0.065$  V is seen to lead to the required linear relation. The accuracy of this method is about  $\pm 0.02$  V, the limits for which deviations from linearity become detectable. This is illustrated by the two dashed lines in Fig. 2 which correspond to  $V_{s0} = -0.065$  V  $\pm 0.025$  V, for which marked deviations from the linear relations are clearly apparent. The slope of the straight line yields the electron bulk concentration  $n_b$  [see eqn (10)]. The value so obtained is marked in Fig. 2 and agrees well with Hall effect measurements.  $N_{s0}$  is derived from the intercept of the straight line with the ordinate ( $F_s = 0$ ).

Once  $V_{s0}$  and  $N_{s0}$  have been determined, the complete  $N_s$  vs  $V_s$  curve (depletion and accumulation ranges) can be evaluated from the measured data through the relations  $V_s = V_{s0} + \delta V_s$ ,  $N_s = N_{s0} + \delta N_s$ . Typical results obtained in this manner are displayed by the full points (stars) in the semi-log plots of Figs 3 and 4, corresponding to the two extremes of the bulk carrier concentration in the available resistivity range of the samples. In the depletion range ( $V_s < 0$ ),  $N_s$  is negative but, because of the logarithmic scale used, the plot is that of its absolute magnitude. The dashed curves in both figures (referred to as "classical") represent eqns (4) and (6), with the appropriate values of  $n_b$  and  $W_b$ . They assume parabolicity of the conduction band throughout. The solid curves ("quantized") take quantization effects into account. As pointed out above, they are based on self-consistent calculations carried out for ZnO [6, 7].

which, to a fair approximation, are adequate also for CdS. As expected, the classical and quantized curves coincide for depletion and moderate accumulation layers. In these ranges, they are seen to account well for the experimental data. Such agreement, obtained with no adjustable parameters, shows, among other things, that there is no significant density of shallow surface states at the CdS surface. After the activation of the shorting switch, such states might release the trapped electrons induced by the pulse back into the conduction band very fast, in a time comparable to that of the discharge of the free electrons in the space-charge layer. The two processes would then be indistinguishable, with the result that the measured value of  $\delta Q_{ss}$  in Fig. 1(c) would be higher than the change in the free space-charge density. The good agreement of the data with the theoretical curves, which represent the free charge only, rules out this possibility.

For strong accumulation layers, on the other hand, the experimental points in Figs 3 and 4 are seen to lie well above both of the theoretical curves. This can only mean that the density of states in the upper reaches of the CdS conduction band is considerably larger than that associated with a parabolic band. This point will be discussed in detail below. The squares in Figs 3 and 4 represent the electron leakage

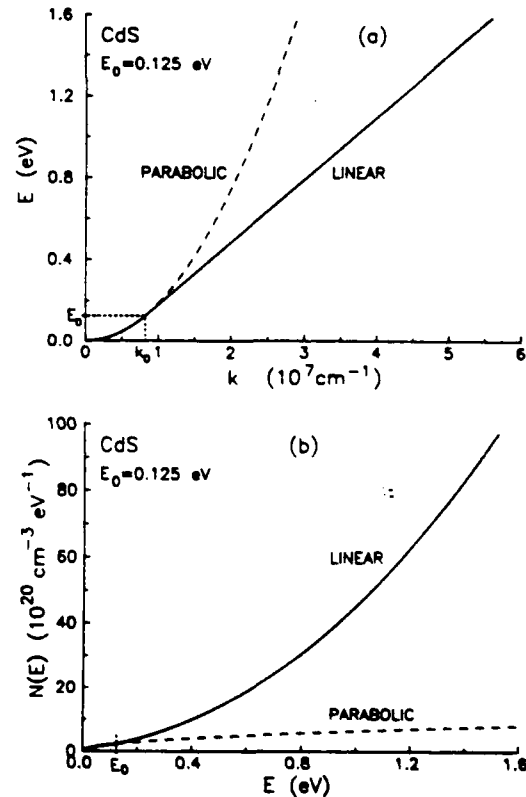


Fig. 5. Model for the structure of the CdS lowest conduction band (solid curves). (a) Energy  $E$  vs wavevector  $k$ . (b) Density of states  $N(E)$  vs energy  $E$ . The dashed curves depict the extensions of the parabolic region for  $E(k)$  and  $N(E)$ .

THIS  
PAGE  
IS  
MISSING  
IN  
ORIGINAL  
DOCUMENT

1073

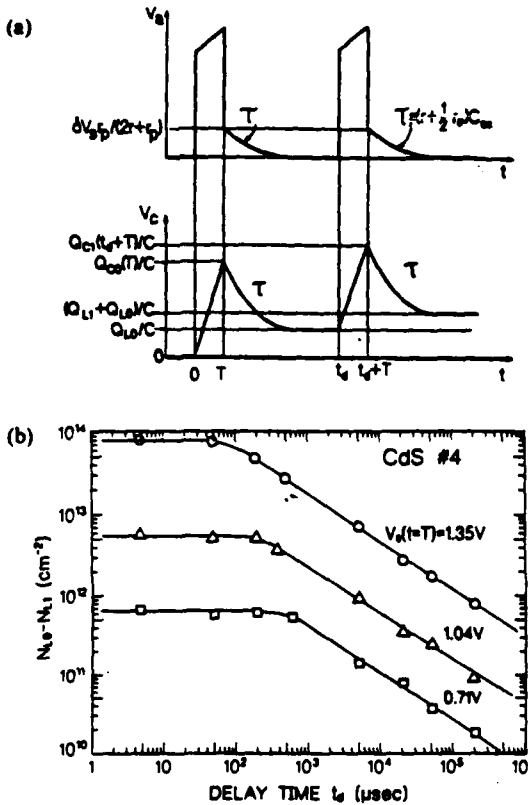


Fig. 8. (a) Schematic representation of the expected response of the voltage drops  $V_s$  and  $V_c$  to a double pulse. (b) Decay characteristics of the leakage charge for different induced barrier heights  $V_s$ .

0.2–10  $\mu\text{s}$ . In other words, the leakage takes place practically instantaneously following the onset of the pulse and is not augmented during the pulse. As will be shown below, it remains stored at or near the interface for a considerable time (hundreds of microseconds). It is gratifying that for both electrolytes and for the different pulse durations, the results of  $N$  vs  $V_s$ , which take into account the electron leakage, are identical. These observations are compatible with the equivalent circuit in Fig. 1(a), and in fact led to its construction. The dashed curve represents, as previously, the classical approximation on the assumption of a parabolic band throughout (constant effective mass). The solid curve is based on the non-parabolic model (Fig. 5), and is again seen to account well for the experimental data.

As pointed out above, electron leakage, the dominant loss mechanism in strong accumulation layers of CdS, is associated with the non-decaying component of  $Q_{L0}$  [Fig. 1(b)]. Hence, apart from the magnitude of the electron leakage, the circuit of Fig. 1(a) is unable to provide any information on the decay characteristics of the leakage charge. To that end, we employed two pulse generators connected in parallel so as to provide two pulses separated by a variable delay time  $t_d$ . Except for the diode D and the shorting switch S, which have been omitted, the rest of the circuit is identical to that in Fig. 1(a). The variations

of  $V_s$  and  $V_c$  with time are schematically displayed in Fig. 8(a). The first pulse charges up the interface capacitance (consisting of the space-charge capacitance  $C_x$  and the leakage capacitance  $C_w$ ). At the termination of the pulse ( $t = T$ ),  $V_s$  does not yield directly the value of  $\delta V_s$ , because in the absence of the diode D,  $\delta Q_{L0}$  now discharges through the internal resistance of the two pulse generators ( $r_p/2$ ). Thus, at  $t = T$ ,  $V_s$  assumes the value of  $[(r_p/2)/(r_p + r_p/2)] \delta V_s$ , from which  $\delta V_s$  can be evaluated. The discharge time  $\tau$  is given approximately (since  $C \gg C_w$ ) by  $(r_p + r_p/2)C_w$ , which is typically of the order of several microseconds. As for  $V_c$ , it rises monotonically during the first pulse, up to the value of  $Q_{L0}(T)/C$ ,  $Q_{L0}(T)$  being the total charge induced by the first pulse. Thereafter it decays with the same time constant of  $\tau$  to the level  $Q_{L0}/C$ ,  $Q_{L0}$  being the leakage charge incurred by the first pulse. After a delay time  $t_d$ , taken to be larger than  $\tau$  such that practically the entire charge in  $C_x$  has decayed ( $V_s \rightarrow 0$ ), the second pulse is applied. Its amplitude is adjusted so as to recharge  $C_x$  to the same value of  $\delta V_s$ . If  $t_d$  is smaller than  $R_w C_w$ , the storage time of the leakage charge, then  $C_w$  would still retain some of its charge at  $t = t_d$ , and the leakage charge  $Q_{L1}$  measured after  $t_d + T + \tau$  would be less than that ( $Q_{L0}$ ) after  $T + \tau$ . By measuring  $Q_{L0} - Q_{L1}$ , the charge retained at the interface up to the application of the second pulse, as a function of the delay time  $t_d$  between the two pulses, one can derive the decay characteristics of the leakage charge. In Fig. 8(b),  $N_{L0} - N_{L1} = -(Q_{L0} - Q_{L1})/q$  is plotted against  $t_d$  on a log-log scale for different values of the induced barrier height  $V_s$ . The decay characteristics are most interesting. For a considerable length of time ( $\sim 500 \mu\text{s}$  for  $V_s = 0.71 \text{ V}$ ,  $\sim 200 \mu\text{s}$  for  $V_s = 1.04 \text{ V}$  and  $\sim 70 \mu\text{s}$  for  $V_s = 1.35 \text{ V}$ ), the leakage charge is almost fully retained at the interface ( $N_{L1} = 0$ ). Subsequently, the charge leaves the interface and its decay with time is nearly linear. The unique features of the leakage charge are: that the leakage occurs in a time shorter than 0.2  $\mu\text{s}$  (see Fig. 7), immediately upon the application of the pulse; that no further leakage takes place through the pulse duration (up to at least 10  $\mu\text{s}$ ); and that the charge remains stored at or near the interface for hundreds of microseconds. From the experimental point of view, these features are most fortunate in that the stored leakage charge can be accurately determined and taken into account in the determination of the  $N$  vs  $V_s$  relation, which is of primary interest in this paper.

## CONCLUSION

The space-charge characteristics of strong accumulation layers of hexagonal CdS show considerable non-parabolicity of the lowest conduction band in this material. A simple model for the structure of the lowest conduction band (Fig. 5) accounts well for the experimental data. It assumes a parabolic band up to

an energy  $E_0$  of 0.125 eV above the band edge and a linear dependence of the energy on the wavevector at higher energies. Such a model is no doubt an oversimplified representation of the actual situation, but it provides a good idea as to the structure of the lowest band; and indeed, the density of states function of the model agrees well with that calculated by Huang and Ching [2] using a minimal basis, orthogonalized LCAO method.

It should be noted that most of the electrons in strong accumulation layers occupy states in the non-parabolic section of the band. As such they are characterized by considerably higher effective masses than at the bottom of the band. Consequently, quantization effects are expected to be insignificant, so that our using the classical calculations [eqn (5)] for the space-charge characteristics in the comparison between theory and experiment is justified.

The measurements presented were made possible by the pulse techniques employed in the study of the S/E interface. These techniques enable both the creation and study of space-charge layers at the semiconductor surface, ranging from large depletion to huge accumulation conditions. What is more important, they permit a straightforward separation of the different components of the induced charge at the S/E interface, so as to obtain the required variation of the free electron density  $N$ , with the barrier height  $V$ . At the same time, the measurements yield the electron leakage across the interface, which becomes prominent in strong accumulation layers. While a determination of such leakage is essential for deriving the experimental  $N$ , vs  $V$ , curve, the leakage process is of considerable interest in itself. The observation that the leakage increases nearly exponentially with barrier height and hence with interface field suggests that electrons tunnel from the accumulation layer into some ionic species (such as  $H^+$ ) in the electrolyte, possibly at sharp points and other imperfections at the interface. The leakage takes place practically instantaneously (in less than  $0.2\ \mu s$ ) following the onset of the pulse and no further leakage occurs

during the pulse (up to at least  $10\ \mu s$  duration—see Fig. 7). This suggests that the density of the ionic species is relatively low: the tunneling electrons appear to saturate completely all the active ionic species within a tunneling distance corresponding to the induced interface field. Another observation is that the leakage remains stored in the electrolyte, for a considerably long time (see Fig. 8). The storage time probably represents the time it takes for diffusion to replenish the exhausted ionic species near the interface. The storage time of several hundreds of microseconds is not unreasonable for such a diffusion process.

**Acknowledgements**—This work was supported in part by a National Science Foundation EPSCoR grant RII 8610677 and in part by U.S. Army Research Office grant No. DAAL03-89-G-0114.

## REFERENCES

1. Bergstresser T. K. and Cohen M. L., *Phys. Rev.* **164**, 1069 (1967).
2. Huang M. Z. and Ching W. Y., *J. Phys. Chem. Solids* **46**, 977 (1985), and references therein.
3. Trokman S., Ph.D. thesis, Hebrew University of Jerusalem, Israel (1978).
4. Trokman S., Many A., Goldstein Y., Heiland G., Kohl D. and Moormann H., *J. Phys. Chem. Solids* **42**, 937 (1981).
5. Wolovelsky M., Levy J., Goldstein Y. and Many A., *Surf. Sci.* **171**, 442 (1986).
6. Eger D., Many A. and Goldstein Y., *Surf. Sci.* **58**, 18 (1976).
7. Eger D. and Goldstein Y., *Phys. Rev. B* **19**, 1089 (1979).
8. Many A., Goldstein Y. and Grover N. B., *Semiconductor Surfaces*, North-Holland, Amsterdam (1965).
9. Stern F., *Phys. Rev. B* **5**, 4891 (1972).
10. Ando T., Fowler A. B. and Stern F., *Rev. mod. Phys.* **54**, 434 (1982).
11. Rose A., *Concepts in Photoconductivity and Allied Problems*, Interscience, New York (1963).
12. Morrison S. R., in *Progress in Surface Science* (Edited by S. G. Davison), Vol. 1, p. 105. Pergamon, Oxford (1971); Morrison S. R., *The Chemical Physics of Surfaces*, Plenum, New York (1977).

## TUNNELING AND PERCOLATION BEHAVIOR IN GRANULAR METALS

I. BALBERG\*, N. WAGNER\*, Y. GOLDSTEIN\* AND S.Z. WEISZ\*\*

\*Racah Institute of Physics, The Hebrew University, Jerusalem 91904, Israel

\*\*Department of Physics, University of Puerto Rico, Rio Piedras 00931, Puerto Rico

### ABSTRACT

The nature of the percolation process in granular metals is examined for the first time by a computer simulation of a system of metallic grains embedded in an insulating matrix. Assuming that the intergrain conduction is due to quantum mechanical tunneling it is found that a percolation-like critical behavior of the conductivity is obtained, but that a percolation *universal* behavior will be found only in a very special case. In contrast, the behavior of the electrical noise does not deviate substantially from the universal one. Comparison of these results with recent experimental observations suggests that in the metallic range, both transport properties are controlled by the continuous metallic network rather than by intergrain tunneling. We propose that the metallic network resembles the previously studied system of "inverted random voids".

### INTRODUCTION

About twenty years ago Abeles and coworkers [1] initiated a comprehensive study of the electronic properties of granular metals, by studying the metal content and temperature dependence of their electrical conductivity,  $\sigma(x,T)$ . As a result of these studies they have attributed the electrical conductance in the materials of low metal content to quantum mechanical tunneling under the constraint of metal grain charging [2], and the conductance of the materials of high metal content, to simple metallic transport in the network formed by the coalescence of the metallic grains [3]. Correspondingly, in the latter case a percolation-like [4] behavior is to be expected [5] where the percolation threshold,  $x_c$ , is associated with the onset of a continuous metallic network. While the more specific nature of the conduction mechanism for  $x < x_c$  was never settled [6], the conduction in the  $x > x_c$  range seemed until recently to be well accounted for by the percolation process mentioned above. The most convincing piece of evidence to support the percolation conduction was the power-law dependence:

$$\sigma \propto (x - x_c)^t \quad (1)$$

found [3] in the  $W-Al_2O_3$  system, with an exponent  $t=1.9$ , which is very close to the universal value of  $t_0 = 2.0$  predicted for three dimensional resistor networks by percolation theory [4,5]. That a percolation geometry is formed by the coalescence of metallic particles is supported by two observations. The first is that in a composite made of macroscopic silver-coated glass spheres which are embedded in Teflon (i.e. where physical contact rather than tunneling between the "metallic" spheres takes place) the same, universal, behavior was found [7]. The second observation is that a transition from thermally activated behavior to a metallic-temperature dependence of the conductivity takes place [1] at metal contents close to  $x_c$ , when  $x_c$  is determined by fitting the experimental data to Eq. (1). Even the problem of "unexpected" high  $x_c$  values obtained experimentally [3], which seemed to cast some question on the percolation description, was removed recently [8]. This removal is based on the argument that such metallic networks are better described by a structure which approximates a randomly closed-packed system of conducting spheres than by a three dimensional (Scher and Zallen-like) system of a mixture of conducting and insulating spheres, or an effective-medium-like [3,9] mixture of the two phases.

Recently there was, however, an attempt by Mantese *et al.* [9,10] to describe the metallic conductivity in  $P_t-Al_2O_3$ , for the range  $x > x_c$ , by an effective medium

theory which, a priori, should yield  $t=1$  for the exponent in Eq. (1). It was also argued [9] on the basis of that theory and the experimentally found [10]  $x$  dependence of the resistivity normalized noise [11],  $S_R$ , in the above material, that even for  $x > x_c$ ,  $S_R$  is dominated by intergrain-tunneling conduction (rather than by metallic transport). In view of the contradiction between the effective medium and the percolation approaches, the first question that arises is whether the experimental power-law behavior reported by Abeles *et al.* [3] is specific to granular  $W-Al_2O_3$  or whether it is a general phenomenon in granular metals. Examining the literature we did not find any other presentation of conductivity data of granular metals that indicate a power-law behavior in general, and a percolation universal behavior, of  $t=t_0$  in particular. Following then the possibility that such a percolation-like behavior was a unique observation we have carried out experimental measurements on another granular system, i.e.  $Co-SiO_2$ . The results of the corresponding measurements are shown in Fig. 1 and are compared to the results [3] on  $W-Al_2O_3$ . Our results clearly confirm the universal behavior for  $x > x_c$  and thus the suggestions of Abeles *et al.* [3] of a percolation-like rather than an effective-medium-like behavior. More details of the  $Co-SiO_2$  granular system and the temperature dependence of its conductivity were presented previously [12].

Since the above experimental evidence provides quite a convincing proof for a percolation-like conduction, the question arises whether the effective medium picture with the intergrain tunneling transport is indeed necessary to account for the resistivity normalized noise, as suggested in Ref. 9. The present computer simulation is trying to answer this question by studying the transport properties of a system of metallic spheres between which a simple quantum tunneling conduction takes place. The corresponding model, which is interesting in its own right, is studied here for the first time. The results appear to show that for  $x > x_c$ , both the conductance and the resistance noise are dominated by the metallic network transport. Moreover, we propose that, at metallic contents just above  $x_c$ , the coalescence of the grains forms an "inverted random void" like network [13,14], i.e. a system of intersecting permeable spheres.

## THE MODEL

Our model consists of hard spheres of diameter  $b$  which are randomly dispersed in a cube of a unit volume. Hence, for  $N$  spheres the fractional occupied volume is  $x = (\pi/6)b^3N$ . In the simulations the  $N$  spheres are placed randomly one after the other. A new sphere is accepted to the system only if it does not overlap a previous sphere. For the precision used in the simulations for the coordinates of the spheres' centers there is no geometrical contact between any pair of spheres. Thus, up to a concentration which corresponds to the randomly close packed structure [8] ( $x=0.64$ ) the system has no connectivity. If we assume that the above system simulates metallic particles embedded in an insulating matrix, all the spherical particles can be considered electrically connected due to quantum

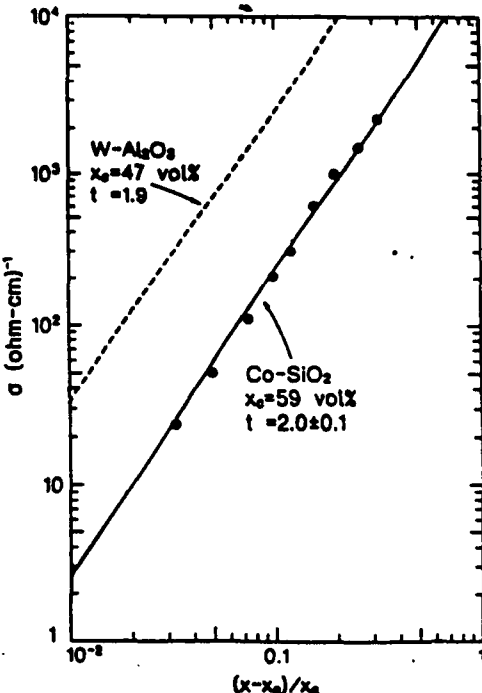


FIGURE 1. The specific conductivity of granular  $Co-SiO_2$  (as obtained both at 78 K and 300 K) as a function of  $(x - x_c)/x_c$ , where  $x$  is the volume fraction of metal and  $x_c$  was obtained from a best fit of the data to Eq. (1). The dashed line represents the data of Abeles *et al.*, ref. 3.

mechanical tunneling. For simplicity we consider simple tunneling or a constant tunneling activation energy [1,2] (i.e. we neglect the interaction energy between the spheres or we assume a high enough temperature [9]) which is a reasonable approximation for a system where all the spheres are of the same diameter [1]. We assume then that the conductance between two metallic grains can be written as:

$$g = g_0 \exp(-s/r_0) , \quad (2)$$

where  $g_0$  is a constant (taken as unity),  $s$  is the separation (at the nearest gap) between two spherical particles and  $r_0$  is the characteristic tunneling distance (the decay distance of the electrons' wave-function [6]). By assigning a conductance  $g$  to each pair of metal spheres we have constructed a network of  $N(N-1)/2$  resistors. This model is expected to be a simple simulation of a granular metal when  $x < x_c$  and, for the ensemble of particles which do not belong to the percolation cluster when  $x > x_c$ . Computationally, however, if reasonable statistics are desired, the computer memory requirements become difficult and expensive. The difficulty is reduced [15] if one assumes a cutoff distance  $s_c$  such that for  $s > s_c$  one takes  $g=0$ . The physical justification for the cutoff is the fact that the average distance between the nearest-neighbor spheres' centers in the system is [16]  $d = (6/\pi N)^{1/3} = b/x^{1/3}$  and one expects then that resistors for which  $s > s_c > d$  will provide a negligible contribution to the conductance of the system. We set  $s_c$  equal to  $6b$ . For typical granular metals [1],  $r_0 \leq b/5$  and  $d \geq b$ , and thus setting  $s_c = 6b$  amounts to neglecting conductances which are smaller than the typical largest conductance in the system by a factor of  $\exp[-5(7-d/b)]$ .

Following the construction of the system we have computed the currents through all the different conductors, using our conjugate-gradient algorithm [14,15], and computed the resultant conductance,  $G$ , and the resistivity normalized noise  $S_R$ . For simplicity we considered the case where the resistance fluctuations are proportional to the value of the resistors. Correspondingly the resistance noise is taken here as [11,13]

$$S_R = A(\sum i_n^4/g_n^2)/(\sum i_n^2/g_n)^2 , \quad (3)$$

where  $A$  is a constant and the summation is over all the resistors in the system. This form has the essentials of the problem, since it contains the diverging nature of the resistor distribution. In view of the exponential dependence of  $g$  [Eq. (2)] it is not expected that intergrain volume effects [13,14] will alter significantly any of the conclusions of the present work.

## RESULTS

The typical behavior of the computed sample conductance  $G$ , as a function of the metallic fractional volume  $x$ , is shown in Fig. 2 for two values of  $r_0/b$ . It is seen that the conductance increases monotonically with  $x$ , and that this increase is faster the smaller the value of  $r_0$ . As is to be expected from the model, there is no critical  $x_c$  below which  $G=0$  (as in well defined percolation systems). On the other hand, the qualitative features of the data in Fig. 2 are similar to those found experimentally in the various granular metals [3,9,12]. Considering the results of Fig. 1 it is apparent that a log-log presentation of the data given in Fig. 2, for  $x$

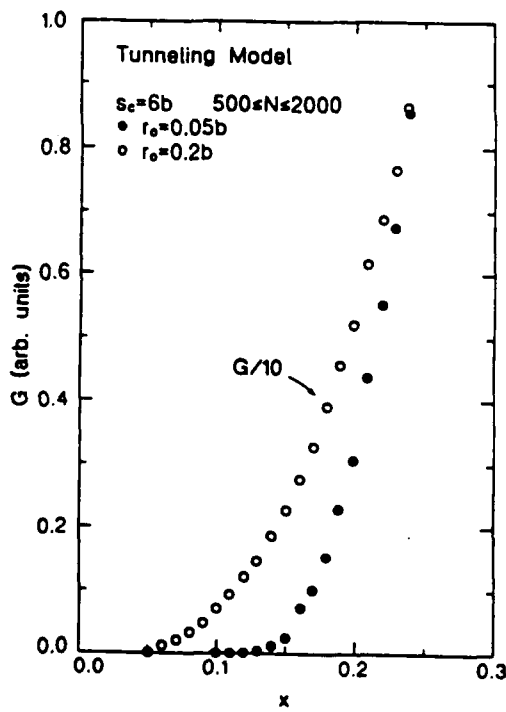


FIGURE 2. The computed dependence of the conductance  $G$  of a system of metallic spheres in a unit volume, on the volume fraction of metal, for two extreme values of  $r_0$ , the characteristic tunneling distance.

larger than some  $x_c$ , may indicate whether our simple tunneling model resembles a percolation-like behavior [Eq. (1)]. Indeed the best fit of these data, for the higher  $x$  values, to a power-law behavior yields a "threshold" value of  $x_c=0.1$  and a corresponding exponent. For the illustration of the nature of this fit we show in Fig. 3 a log-log presentation of the data of Fig. 2. The results show that for the higher  $x$  values the data can be well fitted by a power-law and cannot be distinguished from typical percolation simulation data. Even the deviation from a power-law behavior at low  $x-x_c$  resembles the typical behavior due to finite size scaling [4,14] and thus, for the finite samples used here, this deviation does not reveal a non-percolative conduction. The  $t$  values found are, however, strongly  $r_0$  dependent. Qualitatively this is to be expected for the small values of  $r_0/b$  since for these values only nearest neighbors contribute to the electrical conduction of the system and thus it resembles conduction in a percolating system. The increase of  $t$  with decreasing  $r_0$  indicates then a transition from a conductance due to the many parallel chains of a few resistors of high values, to a conductance due to very few (percolation-like) long chains of many resistors of smaller values. Indeed, for an experimental system where nearest neighbor (percolation-like) tunneling transport takes place between "metallic" spheres which do not coalesce (Mogul-L in PVC), we have found [16] previously that a power law behavior with a nonuniversal exponent ( $t>t_0$ ) is obtained. We may conclude then, that in systems where the tunneling is of short range, the conductance behaves according to the continuum theory of percolation [5,13,16]. In fact, it appears that we may define a phenomenological critical value for  $r_0$ , which marks the transition between a non-percolative ( $t< t_0$ ) behavior to a (nonuniversal) percolative behavior ( $t> t_0$ ). This value, in the present simulations is found to be  $r_{0c}=0.1b$ . To further stress the relationship between the present problem and continuum percolation [5,13] we show in Fig. 4 the conductance distributions,  $P(g)$ , which were found here for various values of  $r_0$ . It is clearly seen that these distributions exhibit a diverging behavior reminiscent of the conductance distribution functions [5]  $P(g)=(1-\alpha)g^{-\alpha}$  which yields the nonuniversal critical behavior for other continuum systems [13,14]. This behavior is known [5] to be manifested by the relation  $t=t_0+\alpha/(1-\alpha)$ . Hence, when the system approaches a percolation-like network

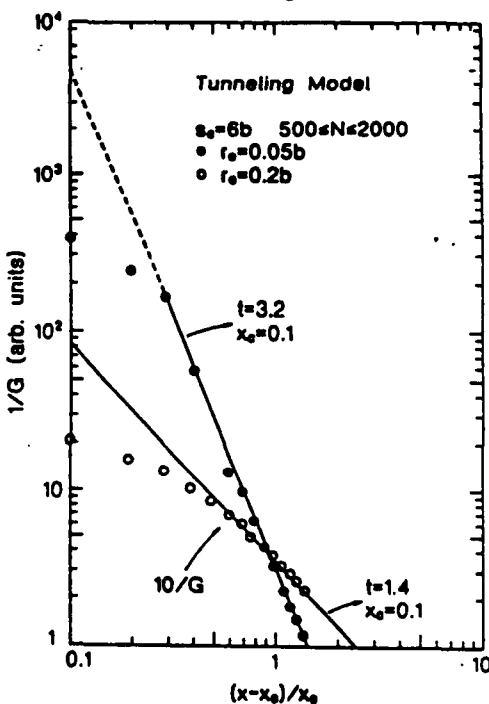


FIGURE 3. The data of Fig. 2 presented on a  $\log(1/G)$  vs.  $\log[(x-x_c)/x_c]$  scale. The apparent critical metallic volume fraction is  $x_c=0.1$ .

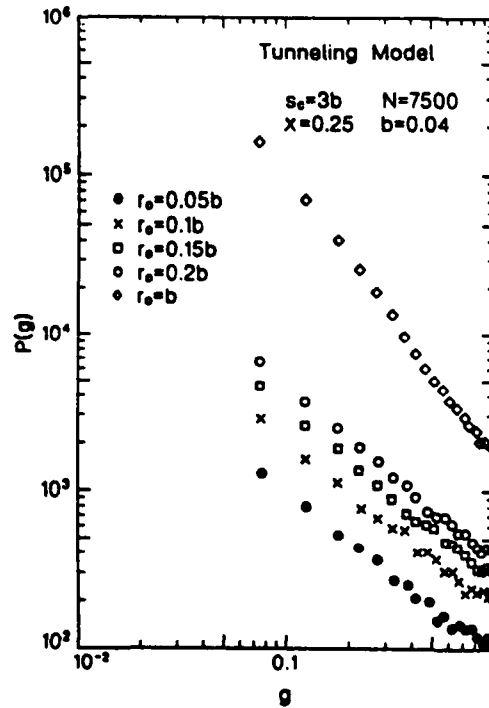


FIGURE 4. The conductance distributions  $P(g)$  of the present simulation for a few tunneling cutoff distances, as marked in the figure.

( $r_0=0$ ) the nonuniversality is due to the singly-connected (nearest-neighbor) largest resistors, as in "conventional" continuum percolation [5,13,16]. In summary, the data presented in Figs. 2-4 show that, in principle, data derived from a system of grains between which simple tunneling takes place, can always be presented in a form which suggests a continuum percolation-like behavior. This presentation is both conceptually [5] (see above) and experimentally [16] justified in the  $r_0/b=0$  limit. We also carried out computations for various values of the cut-off distance  $s_c$  in the range  $b \leq s_c \leq 6b$  and no variations of significance in the present context were observed [15]. Hence we do not discuss these variations here.

Turning to the resistivity normalized noise data, we found again (for  $x > x_c$ ), a power-law behavior of the form:

$$S_R \propto (x - x_c)^{-\kappa} \quad (4)$$

This is shown in Fig. 5. As expected from the conductance data, the values of  $\kappa$  increase with decreasing  $r_0$  but they are found to be confined to a relatively narrow range around 1.6 ( $\kappa = 1.6 \pm 0.5$ ). Noting that the universal  $\kappa$  value is  $\kappa_0 = 1.56$ , the surprising fact is that the deviation  $\kappa - \kappa_0$  (for  $\kappa > \kappa_0$ ) is much smaller than  $t - t_0$  for the same continuum system. This is just the opposite to the situation in typical continuum systems [5,13]. Following the interpretation of the conductivity data, this implies that since the currents through the many "parallel" high resistance channels are small, the noise power is dominated by the singly connected bonds through which the entire current is passing as in a genuine percolation backbone. Hence, while the value  $r_{oc}$  describes the transition to the percolation-like behavior of the electrical resistance, the corresponding value for the resistance noise is probably smaller. The reason for this may be that as  $r_0$  decreases below  $r_{oc}$  the second moment of the current (i.e. the resistance [5]) through a channel made of nearest neighbors dominates the multiplicity of the non-nearest neighbors current paths in the system, but for the fourth moment (i.e. the electrical noise [5,13]) this may not yet be the case.

## DISCUSSION

The first conclusion from our simulation results is that the critical behavior of a system of grains, between which tunneling transport takes place, i.e. the value of  $t$ , depends on  $r_0/b$ . Relating our results to granular metals we note that the values of  $b$  vary significantly from one granular material to another [1]. We should expect then that since the universal-like behavior ( $t=t_0$ ) will appear only for the specific value of  $r_{oc}/b$ , different materials should exhibit different  $t$  values. The fact that in granular metals one seems to get a universal behavior (Fig. 1 and Ref. 3) indicates that a different mechanism is responsible for this behavior, namely percolation. We thus reconfirm the original suggestion of Ref. 3 that in the  $x > x_c$  range, metallic network percolation appears to be a better description of the system than intergrain tunneling, which can not account for the observed universal behavior.

Let us now compare our results with those of Mantese et al. [9,10]. They concluded that even for  $x > > x_c$  the resistance-noise is associated with the

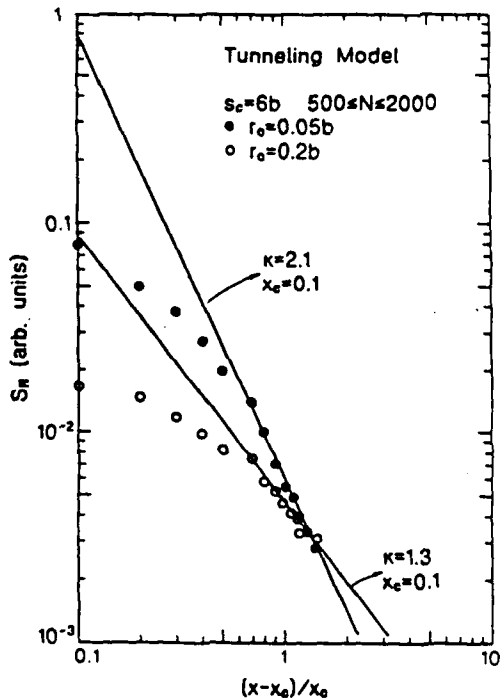


FIGURE 5. The computed dependence of the resistivity normalized noise  $S_R$  as a function of  $(x - x_c)/x_c$  for  $x > 0.1$ . The values of  $\kappa$  (and  $x_c$ ) are marked in the figure.

intergrain tunneling rather than with the continuous metallic network. This conclusion is based on the assumptions that the relative resistance noise associated with intergrain tunneling is independent of  $x$  and is much larger than the corresponding noise associated with the metallic network. In contrast, our results show that the intergrain relative noise is strongly  $x$  dependent. In addition, while the metallic grains contribute maybe only a low relative noise, the metallic network may yield a high relative noise, due to the metallic necks between the grains. This noise, in principle, may be even larger than that associated with intergrain tunneling. Another discrepancy is the value of the resistivity-normalized-noise exponent  $\kappa$ . The results of our model show (see Fig. 5) that intergrain tunneling is reasonably well approximated by the known [13,14] universal percolation behavior  $\kappa/t \leq 1$ . In contrast, the experimental findings of Mantese et al. [9,10] show a very strong nonuniversal behavior manifested by  $\kappa/t = 2.39$  for Pt-Al<sub>2</sub>O<sub>3</sub> and  $\kappa/t = 4.22$  for Mo-Al<sub>2</sub>O<sub>3</sub>. Thus we must conclude that these experimental results may be better explained by conduction in a metallic network than by intergrain conduction. Further support for this argument can be found in their experimental observation of the change in the temperature dependence of the relative resistance noise at the same  $x_c$  as the transition in the temperature dependence of the electrical resistivity to metallic-like.

The question now arises what kind of a metallic network can cause the observed universal value [3] for  $t$  and nonuniversal value [10] for  $\kappa$ . So far the only system known to obey these two conditions simultaneously is the inverted random void model [13,14] (where overlap of permeable conducting spheres takes place) for which in three dimensions [14]  $t = t_0$  and  $\kappa = \kappa_0 + 3$  i.e.  $\kappa/t = 2.30$ . Noting in particular the agreement with one of the experimental values [10] it appears that upon the coalescence of the metallic particles, for  $x$  just above  $x_c$ , the "necks" which are formed resemble overlaps of two permeable spheres. Hence we believe that for  $x > x_c$  both the conductance and the corresponding noise are associated with the inverted-void-like metallic network. It is only for  $x < x_c$  that the electrical behavior of granular metals is determined by intergrain tunneling.

#### ACKNOWLEDGMENT

This work was supported in part by a National Science Foundation EPSCoR grant RII 8610677 and in part by U. S. Army Research Office grant No. DAAL03-89-G-0114.

#### REFERENCES

1. B. Abeles, *Appl. Solid State Science* **6**, 1 (1976). Review.
2. P. Sheng, B. Abeles and Y. Arie, *Phys. Rev. Lett.* **31**, 44 (1973).
3. B. Abeles, H.L. Pinch and J. I. Gittleman, *Phys. Rev. Lett.* **35**, 247 (1975).
4. D. Stauffer, *Introduction to Percolation Theory* (Taylor and Francis, London, 1985).
5. I. Balberg, *Phil. Mag. B* **56**, 991 (1987).
6. C.J. Adkins, *J. Phys. C* **20**, 235 (1987), and references therein.
7. S.-I. Lee, Y. Song, T.W. Noh, X.D. Chen and J.R. Gaines, *Phys. Rev. B* **34**, 6719 (1986).
8. I. Balberg and N. Binenbaum, *Phys. Rev. B* **35**, 8749 (1987).
9. J.V. Mantese, W.A. Curtin and W.W. Webb, *Phys. Rev. B* **33**, 7897 (1986).
10. J.V. Mantese and W.W. Webb, *Phys. Rev. Lett.* **55**, 2212 (1985).
11. R. Rammal, C. Tannous and A.-M.S. Tremblay, *Phys. Rev. A* **31**, 2662 (1985).
12. S. Barzilai, Y. Goldstein, I. Balberg and J. Helman, *Phys. Rev. B* **23**, 1809 (1981).
13. A.-M.S. Tremblay, S. Feng and P. Breton, *Phys. Rev. B* **33**, 2077 (1987).
14. I. Balberg, N. Wagner, D.W. Hearn and J.A. Ventura, *Phys. Rev. Lett.* **60**, 1887 (1988).
15. I. Balberg and N. Wagner (unpublished).
16. I. Balberg, *Phys. Rev. Lett.* **59**, 1305 (1987).

# Accurate determination of the two carriers steady-state mobility-lifetime products in hydrogenated amorphous silicon

I. Balberg

The Racah Institute of Physics, The Hebrew University, Jerusalem 91904, Israel

S. Z. Weisz

Department of Physics, University of Puerto Rico, Rio Piedras 00931, Puerto Rico

(Received 24 October 1990; accepted for publication 6 May 1991)

The photocarrier grating (PCG) technique is used for the first time in the high electric field regime. The results are shown to confirm previously unproven theoretical predictions for this regime. It is demonstrated that, by application of the PCG technique in the high-field regime, accurate values for the ratio of the two carriers mobility-lifetime products can be deduced. This is in contrast with the fact that their sum cannot be derived accurately from the measurement of photoconductivity because one cannot determine accurately the carrier generation rate. Combining the ratio, determined by the high field PCG, with the low-field data yields accurate values for the mobility-lifetime products of both carriers.

## I. INTRODUCTION

The two most informative parameters which characterize the photoelectronic properties of a semiconductor are the mobility-lifetime,  $\mu\tau$ , product of the two charge carriers.<sup>1,2</sup> These parameters contain the information regarding the transport mechanism ( $\mu$ ) and the recombination kinetic mechanism ( $\tau$ ). Traditionally  $\mu\tau$  products have been determined under transient conditions<sup>3</sup> or under steady-state conditions.<sup>4</sup> It is well known that the two types of measurements yield different results,<sup>5,6</sup> but in devices it is usually the steady-state  $\mu\tau$  value which determines their performance.<sup>1,2</sup> For both basic physics<sup>7</sup> and device physics<sup>8</sup> it is important in many cases to determine these values accurately. This paper proposes and demonstrates a new technique for accurate determination of the  $\mu\tau$ 's of both carriers.

While by now it is quite established that in low mobility materials the photocarrier grating technique (PCG) yields accurate values for the minority carrier (the carrier with the lower drift mobility<sup>10</sup>) steady-state  $\mu\tau$  product,<sup>9</sup> there is no accurate technique to derive the same product for the majority carriers. Thus, the latter quantity has been derived thus far from the measurement of the photoconductivity  $\sigma$ . Assuming that the electron is the majority carrier, the relation between the above quantities is expressed by the equation<sup>10</sup>

$$\sigma = q(\mu_e\tau_n^R + \mu_h\tau_p^R)G \quad (1)$$

and the inequality  $\mu_e\tau_n^R > \mu_h\tau_p^R$ . Here  $q$  is the (positive) electronic charge,  $G$  is the carriers generation rate,  $\mu_e(\mu_p)$  is the band mobility of the electron (hole), and  $\tau_n^R(\tau_p^R)$  is the recombination time for the electron (hole). The experimental difficulty with the application of Eq. (1) is that  $\sigma$  and in particular  $G$  cannot be determined accurately. The difficulties are associated with inaccurate determination of the sample geometry, the quantum efficiency of the carrier generation, the absorbed light fraction (even after correcting for reflectivity and scattering), and the inhomogeneity of the impinging light beam. Usually, when

one derives a  $\mu\tau$  value from photoconductivity [by using Eq. (1) or similar expressions<sup>1,5</sup>], one can only say that this value is within a factor of two of the "correct" value. This problem may become severe if one wants to determine  $\mu_e\tau_n^R$  when  $\mu_e\tau_n^R \approx \mu_h\tau_p^R$ . In this case, one determines  $\mu_h\tau_p^R$  from another measurement (e.g., the low field PCG<sup>11</sup>) and with the inaccurate sum [Eq. (1)] one may obtain a "negative" value for  $\mu_e\tau_n^R$ . Another example for the need to overcome the inaccuracies is in the problem of the ratio between the steady state  $\mu\tau$  value and the transient  $\mu\tau$  value.<sup>10</sup> It may be that this ratio is twice as large or twice as small as that reported in the literature.<sup>5,6</sup>

Following these considerations it appears that there is a need for a technique in which the uncertainties in the measurement will be removed. One of the major advantages of the photocarrier grating (PCG) technique<sup>11-13</sup> is that, one measures photoconductivity ratios, rather than absolute values of the photoconductivity, under the same  $G$ . This technique has been used, however, thus far in the zero-field limit,<sup>9,11</sup> where it yields essentially the minority carriers  $\mu\tau$ , and in the low-field (or "relaxation") regime, where it yields an ill-defined  $\mu\tau$  product.<sup>14,15</sup> It can be shown<sup>16</sup> that the latter is a result of the fact that in the low-field regime the measured quantity ( $\beta$ , see below) is a complicated combination of the two carriers  $\mu\tau$  products and other parameters and thus it cannot provide unique, single carrier,  $\mu\tau$  values. In this paper we examine the previously unstudied high-field regime and show that in this regime one can derive a unique value for  $\mu_h\tau_p^R/(\mu_e\tau_n^R)$ . A combination of this result with the  $\mu_h\tau_p^R$  result derived from the zero field PCG measurement then yields an accurate value for  $\mu_e\tau_n^R$ .

## II. THEORETICAL BACKGROUND

Turning to the utilization of the PCG method for the present problem, we follow the concepts of the zero-field PCG theory<sup>12</sup> while introducing the specific variations and definitions associated with the high-field regime. A more detailed account of the analysis and the physical picture of

the photocarrier grating under these conditions will be given elsewhere.<sup>16</sup> In the PCG configuration, two light beams which can interfere generate carriers in a photoconductor.<sup>11</sup> When they are made to interfere, a sinusoidal carrier generation along the direction between two coplanar electrodes (hereafter the  $x$  direction) takes place. When they are made not to interfere, a uniform illumination results. The ratio between the additional photoconductivities which result due to the application of one of the beams (the low-intensity beam), in the above two situations is the quantity which is being determined<sup>11</sup> experimentally,  $\beta$ . The photocarrier generation function is given then by  $G = G_0 + \Delta G(x)$ , where:  $\Delta G(x) = A_g \cos(kx)$ . The generated electron concentration distribution which results is  $n(x) = n_0 + \Delta n(x)$ , where  $\Delta n(x) = A_e \cos(kx + \nu)$ , and the corresponding hole concentration distribution is  $p(x) = p_0 + \Delta p(x)$ , where  $\Delta p(x) = A_h \cos(kx + \phi)$ . Here  $G_0(n_0, p_0)$  is the carrier generation (electron concentration, hole concentration) when no grating is formed,  $k = 2\pi/\Lambda$  where  $\Lambda$  is the grating period, and  $\nu$  ( $\phi$ ) is the phase shift of the electron (hole) concentration grating<sup>17</sup> with respect to the carrier generation grating ( $\phi = \nu = 0$  with no field).  $A_g$  is the amplitude of the generation grating and  $A_e$  ( $A_h$ ) is the excess electron (hole) concentration amplitude in the presence of the grating. The theory developed thus far<sup>12,16,17</sup> is applicable only if the linearization of the continuity equation applies, i.e., if  $A_g \ll G_0$ , and if the material is assumed "intrinsic" in the sense that  $n_0$  and  $p_0$  are much larger than the carrier concentrations in the dark. The task of the theory is then to present  $A_e$ ,  $A_h$ ,  $\phi$ , and  $\nu$  in terms of the  $\mu\tau$  products while the task of the experimental procedure is to correlate the former parameters with the quantity measured by the PCG technique,  $\beta$ . For the presentation of the experimental results one uses the normalized grating amplitude<sup>13,17</sup>  $\gamma_{\text{eff}}$  which can be expressed as<sup>16</sup>

$$\gamma_{\text{eff}}^2 = [(\mu_e A_e \cos \nu + \mu_h A_h \cos \phi)^2 + (\mu_e A_e \sin \nu + \mu_h A_h \sin \phi)^2] / [A_g \sigma / G_0] \quad (2)$$

and is related to  $\beta$  by<sup>11,16,17</sup>

$$\gamma_{\text{eff}}^2 = (1 - \beta) / (2\gamma_0^2), \quad (3)$$

where  $\gamma_0$  is an experimental quality factor (of the order of unity<sup>11</sup>) and  $\gamma$  is the light intensity exponent of the photoconductivity.<sup>18</sup>

Under the small signal grating conditions the linearization of the transport-continuity equations is possible and for the electrons the corresponding equation takes the form<sup>12,17</sup>

$$-(\mu_e q n_0 / \epsilon) (\Delta p / \theta_p - \Delta n / \theta_n) - D_e \left( \frac{\partial^2 \Delta n}{\partial x^2} \right) - \mu_e E_0 \left( \frac{\partial \Delta n}{\partial x} \right) + (\Delta n / \tau_n + \Delta p / \tau_p) = A_g \cos(kx). \quad (4)$$

The equation for the holes takes a similar form. The first term in Eq. (4) is the space charge term,  $\epsilon$  is the dielectric constant, and the  $\theta$ 's are the free to total electron

(or hole) ratios.<sup>18</sup> The second term is the diffusion term and we assume throughout that  $D_e = (k_B T / q) \mu_e$ , where  $k_B T$  is the thermal energy. The third term is the drift term where  $E_0$  is the applied dc field, and the last term on the left-hand side of Eq. (4) is the small signal recombination term<sup>17</sup> (characterized by the small signal recombination times  $\tau_n$  and  $\tau_p$ ). For all practical purposes<sup>16</sup>  $\tau_n = \tau_n^R$  and  $\tau_p = \tau_p^R$ . Equation (4) and its coupled hole equation can be solved analytically by substituting the above suggested solutions in these equations,<sup>16</sup> but the expressions for  $A_e$ ,  $A_h$ ,  $\phi$ , and  $\nu$  are so cumbersome that they are of no practical use for deriving unique  $\mu\tau$ 's from the experimental  $\beta$ . The alternative approach<sup>16</sup> is to perform the experiments under conditions which correspond to a simplified mathematical version of Eq. (4) and its hole counterpart, such that a desirable *unique* and simple relation between the above mentioned quantities will result. Such a simplification occurs if the space-charge term is made negligible compared with the diffusion term and the diffusion term is made small but non-negligible compared to the drift term.<sup>16</sup> If we assume that Eq. (4) has the sinusoidal solutions suggested above, the condition mentioned can be written [see Eq. (4)] as

$$(qn_0 / \epsilon \theta_n) [(\mu_e \theta_n / \mu_h \theta_p) - 1] \ll k^2 k_B T / q < kE_0. \quad (5)$$

Under condition (5), the algebraic equation obtained by using the suggested solutions of Eq. (4) (and its hole counterpart) can be easily shown to yield reasonably simple relation between  $\gamma_{\text{eff}}$  and the  $\mu\tau$  products.<sup>16</sup> In particular, assuming that:  $\mu_e \tau_n = \mu_h \tau_p > kE_0 \mu_e \mu_h \theta_n \theta_p$  (i.e., fields higher than  $k k_B T / q = 1600$  V/cm but not too high, see below) the solution for  $\gamma_{\text{eff}}$  [see Eq. (2)] becomes<sup>16</sup>

$$\gamma_{\text{eff}} = (2k k_B T / q E_0) \{ \mu_e \mu_h \theta_n \theta_p / [(\mu_e \tau_n)^2 - (\mu_h \tau_p)^2] \}. \quad (6)$$

If we further assume that  $\mu_e \tau_n > 3\mu_h \tau_p$ , this equation can be further reduced to

$$\gamma_{\text{eff}} = (2k k_B T / q) [\mu_h \tau_p^R / (\mu_e \tau_n^R)] (1/E_0). \quad (7)$$

Since, in the experiment,  $2k k_B T / q$  is known, a presentation of the measurable quantity  $\gamma_{\text{eff}}$  [see Eq. (3)] as a function of  $1/E_0$  is expected to yield the steady-state carriers  $\mu\tau$ 's ratio. On the other hand, the known result (in the  $E_0 \rightarrow 0$  limit) for the ambipolar diffusion length  $L$  is that<sup>11,12</sup>

$$\gamma_{\text{eff}} = (1 + k^2 L^2)^{-1}, \quad (8)$$

where

$$L^2 = (2k_B T / q) \mu_h \tau_p^R. \quad (9)$$

As pointed out above, the principle of the method is to substitute the experimental results for  $\gamma_{\text{eff}}$  in Eqs. (7)–(9) in order to derive the two  $\mu\tau$  products without resorting to the inaccurate estimates of  $\sigma$  and  $G$ .

Before turning the experimental results let us consider the consequences of condition (5). For the typical grating of  $\Lambda = 10^{-4}$  cm this condition implies that  $E_0 > 1600$  V/cm, and for  $a\text{-Si:H}$  if  $(\mu_e \theta_n) / (\mu_h \theta_p) \approx 10$ , one must not exceed<sup>16</sup> a light intensity of  $1.5 \text{ mW/cm}^2$  (for higher drift mobility ratios lower intensities should be used). For the demonstration of the proposed method under convenient

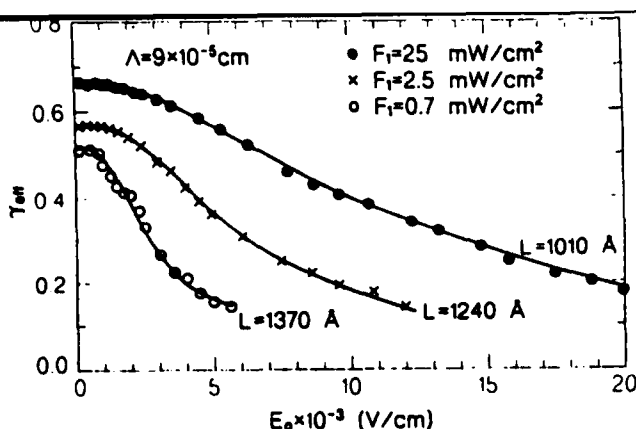


FIG. 1. The measured dependence of the excess carriers normalized grating-amplitude vs the applied electric field, under three different background He-Ne illuminations. The ambipolar diffusion lengths are determined from the zero field limit.

experimental conditions, this constraint led us to choose an *a*-Si:H material for which  $(\mu_e \theta_n) / (\mu_h \theta_p) < 10$  as well as the lowest light intensity which enabled a convenient measurement (0.7 mW/cm<sup>2</sup>). A rough preliminary estimate of this ratio was determined from the corresponding photoconductivity and the diffusion length measurements by applying the method of Ritter *et al.*<sup>13</sup> We note in passing that the material used in the following experiment had a photoconductivity of  $1.7 \times 10^{-5}$  ( $\Omega \text{ cm}$ )<sup>-1</sup> at 100 mW/cm<sup>2</sup> and that for this light intensity  $\mu_e \theta_n / \mu_h \theta_p$  is larger than the corresponding value for the weak light intensity which we have used for the verification of the linear dependence of  $\gamma_{\text{eff}}$  on  $1/E_0$ . This is, of course, a result of the "faster" displacement of the quasi-Fermi level for electrons, in comparison with that of the holes, with increasing illumination intensity in *a*-Si:H.<sup>10,16</sup> We emphasize that in contrast to the common  $E_0 \rightarrow 0$  case,<sup>13,14</sup> we are interested here in *nonambipolar* conditions for the excess carriers.

### III. EXPERIMENTAL RESULTS

The experimental details of the present work were much the same as those described in detail previously.<sup>11,19</sup> The measured dependence of  $\gamma_{\text{eff}}$  on the applied electric field  $E_0$  is shown in Fig. 1. The conspicuous qualitative feature of the data is the inflection point in the  $\gamma_{\text{eff}}$  vs  $E_0$  dependence, and in particular its shift towards the lower values of  $E_0$  with decreasing illumination intensity. This result is consistent with the predictions from computer<sup>17</sup> and analytic<sup>16</sup> solutions of the continuity equations [see Eq. (4)], and with the expected transition from ambipolar to nonambipolar transport in the grating [Eq. (5)] with decreasing dielectric response time and increasing field. The transition (which is signaled by the inflection point) is necessary for the applicability of Eq. (6). As discussed above, and as can be gathered from the data, this condition is well fulfilled for illumination levels below 2.5 mW. Also given in the figure are the ambipolar diffusion lengths derived by using the  $\gamma_{\text{eff}}$  values at  $E_0 \rightarrow 0$  and relation (8) (with  $\Lambda = 9 \times 10^{-5}$  cm). These values have been con-

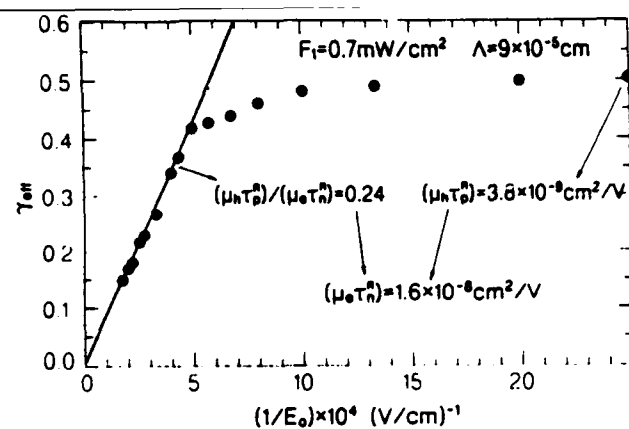


FIG. 2. The results of Fig. 1 for the He-Ne illumination of 0.7 mW/cm<sup>2</sup>, plotted as a function of the inverse applied electric field. The slope of the plot and the zero field result yield the  $\mu\tau$  products for the two carriers.

firmed independently by a more detailed PCG measurement.<sup>19</sup> We should point out that the measurement for  $\gamma_{\text{eff}} < 0.15$  requires an extremely high sensitivity of the technique which is beyond our capability at present.

Following the observation of nonambipolar transport at 2500 V/cm (the inflection point, for  $F_1 = 0.7$  mW/cm, see Fig. 1) we expect, for higher fields, the linear  $\gamma_{\text{eff}}$  vs  $1/E_0$  dependence predicted by our "diffusion/drift perturbation" approach<sup>16</sup> [Eq. (7)]. Indeed, this expectation is fulfilled by the  $\gamma_{\text{eff}}$  vs  $1/E_0$  plot, shown in Fig. 2. Comparing the slope in the linear regime with Eq. (7) we get a value of 0.24 for the minority to majority  $\mu\tau$  ratio. Combining this with the  $\mu_h \tau_p^R$  result [derived as explained above from Eqs. (8) and (9)], we find that the sum of the two  $\mu\tau$ 's is  $2 \times 10^{-8}$  cm<sup>2</sup>/V.

### IV. DISCUSSION

In order to check the qualitative validity of the above novel theoretical and experimental approaches, we have compared the above sum of the  $\mu\tau$ 's with the one derived from photoconductivity, although, as is apparent from the above discussion, these may differ by a factor as large as 2. Our best experimental estimate of  $\sigma$  under the 0.7-mW/cm<sup>2</sup> illumination (electrode separation 0.4 mm, beam diameter 3 mm, and sample thickness 1  $\mu\text{m}$ ) was  $1.3 \times 10^{-7}$  ( $\Omega \text{ cm}$ )<sup>-1</sup>. The corresponding He-Ne laser photon flux was  $2.1 \times 10^{15}$  photons/cm<sup>2</sup> s. Assuming the commonly accepted<sup>20</sup> 30% reflection, and an absorption coefficient of  $2 \times 10^3$  cm<sup>-1</sup> we estimated a carrier bulk generation rate of  $2.8 \times 10^{19}$  carrier-pairs/cm<sup>3</sup> s. Using these values in Eq. (1), we find that  $\mu_e \tau_n^R + \mu_h \tau_p^R = 2.9 \times 10^{-8}$  cm<sup>2</sup>/V. Considering the more reliable procedures for the determination of this sum from the measured photocurrent,<sup>1,3,21</sup> we found somewhat different estimates. All the estimates can be summarized, however, by  $(3 \pm 1) \times 10^{-8}$  cm<sup>2</sup>/V, (which agrees with the uncertainty range suggested in the above given discussion). The important point, of course, is the good agreement of this value with the value derived from the data of Fig. 2. This agreement proves the validity

of our suggested new method for the derivation of the  $\mu\tau$ 's. For the reasons given above, the difference between the two results is attributed to the uncertainties associated with the extraction of the  $\mu\tau$  from photoconductivity, rather than to possible shortcomings of the present method.

In conclusion, we have presented the first study of the PCG in the high electric field regime and have shown quantitative agreement between experimental results and the simplest analytical predictions for this regime. The agreement with the corresponding photoconductivity data shows that the suggested technique can be useful for the determination of accurate values for the two carriers  $\mu\tau$  products.

#### ACKNOWLEDGMENTS

This work was supported in part by the U.S.-Israel Binational Science Foundation and in part by the U.S. Army Research Office, Grant No. DAAL 03-89-G-0114. The authors are indebted to A. E. Delahoy for providing the samples used in the present work, and to H. Branz for critical reading of the manuscript.

- <sup>1</sup>R. A. Smith, *Semiconductors* (Cambridge University Press, London, 1978).
- <sup>2</sup>S. M. Sze, *Physics of Semiconductor Devices* (Wiley, New York, 1981).
- <sup>3</sup>A. Many and G. Rakavy, *Phys. Rev.* **126**, 1380 (1962).
- <sup>4</sup>H. S. Sommers, Jr., in *Methods in Experimental Physics*, edited by K. Lark Horovitz and V. A. Johnson (Academic, New York, 1959), Vol.

- <sup>6</sup>Pt. B., p. 357.
- <sup>5</sup>K. D. Mackenzie and W. Paul, *MRS Conf. Proc.* **95** (North-Holland, Amsterdam, 1987), p. 281.
- <sup>6</sup>M. A. Parker and E. A. Schiff, *Phys. Rev. B* **37**, 10426 (1988); R. S. Crandall and I. Balberg, *Appl. Phys. Lett.* **58**, 508 (1991).
- <sup>7</sup>See, e.g., J. Kocka, E. Sipek, O. Stika, H. Curtiss, and F. Juska, *J. Non-Cryst. Solids* **114**, 336 (1989).
- <sup>8</sup>See, e.g., R. S. Crandall, *J. Appl. Phys.* **54**, 7176 (1983).
- <sup>9</sup>L. Yang, A. Catalano, R. R. Arya, and I. Balberg, *Appl. Phys. Lett.* **57**, 908 (1990).
- <sup>10</sup>R. S. Crandall, in *Semiconductors and Semimetals*, edited by J. I. Pankove (Academic, New York, 1984), Vol. 21, Part B, Chap. 8; R. S. Crandall and I. Balberg, *Appl. Phys. Lett.* **58**, 508 (1991).
- <sup>11</sup>D. Ritter, E. Zeldov and K. Weiser, *Appl. Phys. Lett.* **49**, 291 (1986).
- <sup>12</sup>I. Balberg, *J. Appl. Phys.* **67**, 6329 (1990).
- <sup>13</sup>D. Ritter, E. Zeldov, and K. Weiser, *J. Non-Cryst. Solids* **97-98**, 619 (1987).
- <sup>14</sup>D. Ritter and K. Weiser, *Phys. Rev. B* **34**, 9031 (1986).
- <sup>15</sup>J. Z. Liu, A. Maruyama, S. Wagner, and A. Delahoy, *J. Non-Cryst. Solids* **114**, 363 (1989).
- <sup>16</sup>I. Balberg, *Phys. Rev. B* **15** (in press).
- <sup>17</sup>D. Ritter, E. Zeldov, and K. Weiser, *Phys. Rev. B* **38**, 8296 (1988). In this paper the high-field regime has been considered but only numerical solutions were given. Hence, a unique derivation of  $\mu\tau$  products by comparison of experimental results with that work is impossible.
- <sup>18</sup>A. Rose, *Concepts in Photoconductivity and Allied Problems* (Wiley, New York, 1963).
- <sup>19</sup>I. Balberg, A. E. Delahoy, and H. A. Weakliem, *Appl. Phys. Lett.* **53**, 992 (1988).
- <sup>20</sup>G. D. Cody, in *Semiconductors and Semimetals*, edited by J. I. Pankove (Academic, New York, 1986), Vol. 21, Pt. B, p. 11, and references therein.
- <sup>21</sup>W. B. Jackson, R. J. Nemanich, and N. M. Amer, *Phys. Rev. B* **27**, 4871 (1983).

# Identification of nonambipolar transport in the application of a photocarrier grating to hydrogenated amorphous silicon

I. Balberg

The Racah Institute of Physics, The Hebrew University, Jerusalem 91904, Israel

S. Z. Weisz

Department of Physics, University of Puerto Rico, Rio Piedras 90931, Puerto Rico

(Received 20 May 1991; accepted for publication 5 July 1991)

Thus far the many reports concerning the utilization of the photocarrier grating (PCG) method have assumed that ambipolar transport takes place in such a PCG when it is imposed on hydrogenated amorphous silicon ( $a$ -Si:H). This assumption, which is decisive in the interpretation of the experimental results in terms of the ambipolar diffusion length, has not been tested thus far. In this letter a corresponding testing criterion is proposed, and it is demonstrated that whenever ambipolarity is lost, the PCG-derived diffusion lengths may be wrong. The finding that ambipolarity is maintained in device quality  $a$ -Si:H is shown to confirm the theoretical suggestion that, whenever observed, the ambipolarity in  $a$ -Si:H is due to shallow trapping effects.

By now the photocarrier grating (PCG) technique for the estimation of the minority-carrier mobility lifetime ( $\mu\tau$ ) product in amorphous semiconductors has become the most accepted and widely used method for this purpose.<sup>1-7</sup> The very fundamental assumption associated with the interpretation of the corresponding experimental results is that ambipolarity (or local charge neutrality) is maintained in the PCG. Under these conditions the physical quantity derived is the important photoelectronic parameter which is known as the ambipolar diffusion length  $L$ . This crucial assumption has not been confirmed thus far. In fact, it is quite surprising that in spite of the many reports<sup>1-7</sup> in which the results were interpreted in terms of  $L$  no one has reported nonambipolar transport. In view of the importance of the knowledge of the minority-carrier  $\mu\tau$  ( $\propto L^2$ ) product for the physics<sup>3</sup> and application<sup>8</sup> of hydrogenated amorphous silicon ( $a$ -Si:H) and in view of the present abundance of the PCG method, a critical examination of this assumption appears necessary.

The PCG technique is based on a comparison of the ac (due to light chopping) photocurrent through a photoconductor under two conditions: when it is subjected to spatially modulated illumination and when under the same illumination intensity there is no such modulation. The relation between the corresponding ratio of the two ac photocurrents,  $\beta$ , and the microscopic transport and kinetic parameters of the material, which are summarized (see below) by the parameter  $\gamma_{\text{eff}}$ , is given by<sup>1,9</sup>

$$\gamma_{\text{eff}} = [(1 - \beta)/(2\gamma\gamma_0^2)]^{1/2}. \quad (1)$$

Here  $\gamma_0$  is an experimental quality factor which is of the order of unity<sup>1,3</sup> and  $\gamma$  is the well-known light-intensity exponent of the samples' dc photoconductivity  $\sigma_0$  (i.e.,  $\sigma_0 \propto G_0^\gamma$ , where  $G_0$  is the carrier's generation rate under the relatively large uniform dc background illumination).

The purpose of this letter is to suggest a test by which one can qualitatively identify the existence or nonexistence of ambipolar transport in the PCG and to demonstrate experimentally that one can find ambipolar as well as nonambi-

polar transport in  $a$ -Si:H materials. This test is possible now due to the development of an analytic theory of the PCG.<sup>9</sup>

Since the concept of ambipolarity is somewhat different in the present context than in the classical theory of semiconductors<sup>10</sup> we redefine it here as the set of conditions under which local charge neutrality prevails (see below). Under these conditions the PCG measurement can be readily shown<sup>1,9</sup> to yield the relation

$$\gamma_{\text{eff}} = (1 + k^2 L^2)^{-1}, \quad (2)$$

where  $k = 2\pi/\Lambda$ ,  $\Lambda$  is the grating period, and  $L$  is defined by<sup>9,11</sup>

$$L^2 = (2k_B T/q)[\mu_e \theta_n \mu_h \theta_p]/(\mu_e \theta_n + \mu_h \theta_p) \cdot t_\theta \equiv 2D_\theta t_\theta \quad (3)$$

Here  $k_B T$  is the thermal energy,  $q$  is the (positive) electronic charge,  $\mu_e$  ( $\mu_h$ ) is the electrons' (holes') band mobility,  $\theta_n$  ( $\theta_p$ ) is the ratio between the free-electron (hole) concentration  $n_0(p_0)$ , and the total (free and trapped) concentration of electrons (holes),  $N + n_0(P + p_0)$ , and  $t_\theta$  is the "common" two-carrier recombination time.<sup>9,12,13</sup> Under the PCG configuration, in the zero applied field limit, the excess free-electron (hole) concentration that forms under the generation grating is described by  $\Delta n = A_e \cos(kx)$  [ $\Delta p = A_h \cos(kx)$ ], where  $A_e$  ( $A_h$ ) is the excess electron (hole) concentration amplitude. Hence it is obvious that local charge neutrality will be maintained if  $\Delta p/\theta_p = \Delta n/\theta_n$ . Physically this condition means that all (free and trapped) generated electrons are not spatially separated from all generated holes. Since the carriers diffuse from regions of excess illumination and the dielectric response time  $\tau_d$  ( $= \epsilon/\sigma_0$ , where  $\epsilon$  is the dielectric constant) is finite, some separation will always exist. In the PCG configuration, where the only imposed length scale is the grating period  $\Lambda$ , one can say that "local" charge neutrality prevails if the two-carrier separation in the PCG is much smaller than  $\Lambda$ . This happens when  $\Lambda$  is much larger than the dielectric diffusion lengths of the two carriers. The latter lengths are the distances traveled by the two carriers due to diffusion within the time  $\tau_d$ . This distance for all the

(free and trapped) electrons is  $(D_e \theta_n \tau_d)^{1/2}$ , and for all the holes it is  $(D_h \theta_p \tau_d)^{1/2}$ . Here  $D_e$  ( $D_h$ ) is the diffusion coefficient of free electrons (holes). Hence the requirements for ambipolarity in the PCG are  $\Lambda > (D_e \theta_n \tau_d)^{1/2} = L_{ed}$  and  $\Lambda > (D_h \theta_p \tau_d)^{1/2} = L_{hd}$ .

This conclusion, from the above simple physical picture, has also been derived rigorously.<sup>9</sup> The exact solutions found (which are given explicitly in Ref. 9) yield the dependencies of  $A_e$  and  $A_h$  on  $k^2$  and  $f$  where

$$f = A_e/A_h = [\sigma_0/(\epsilon \theta_p) + k^2 D_h]/[\sigma_0/(\epsilon \theta_n) + k^2 D_e], \quad (4)$$

and where  $\sigma_0 = q(\mu_e n_0 + \mu_h p_0)$ . Considering the definition (4) it is apparent that  $f$  is a quantity that measures the degree of ambipolarity. Indeed, when the above ambipolarity requirements for  $L_{ed}$  and  $L_{hd}$  are fulfilled,  $f$  is reduced to  $\theta_n/\theta_p$ , and the ambipolarity condition  $A_e = (\theta_n/\theta_p)A_h$  is fulfilled. Correspondingly  $A_e$  is given by<sup>9</sup>

$$A_e = G_1 \theta_p / [1/\theta_p + 2k^2 D_e]. \quad (5)$$

With application of Eqs. (3) and (5) and the definition<sup>14</sup> of  $\gamma_{\text{eff}}$  as the ratio of the excess photoconductivities in the presence and absence of the grating, i.e., as<sup>9,14</sup>

$$\gamma_{\text{eff}} = q(\mu_e A_e + \mu_h A_h) / [G_1 \sigma_0 / G_0],$$

one can immediately see that under the ambipolar conditions  $\gamma_{\text{eff}}$  is reduced to the well-known<sup>13</sup> relation given by Eq. (2).

If the conditions for  $L_{ed}$  and  $L_{hd}$  are not fulfilled simultaneously we have to introduce  $f$  from Eq. (4) into the expressions for  $A_e$  and  $A_h$  and then use the definition of  $\gamma_{\text{eff}}$ . For example, in the extreme nonambipolar limit, i.e., when  $f = D_h/D_e$ ,  $\gamma_{\text{eff}}$  has the form

$$\gamma_{\text{eff}} = (1 + Bk^2) / (Ck^4 + Dk^2 + E), \quad (6)$$

where  $B, C, D, E$  are quantities determined (through cumbersome expressions) by the various material parameters that characterize<sup>9</sup>  $A_e$  and  $A_h$ . In the intermediate case, i.e., when the condition for  $L_{ed}$  is reversed but the condition for  $L_{hd}$  is fulfilled [so that  $f \approx (k^2 D_h \theta_p \tau_d)^{-1}$ ]  $\gamma_{\text{eff}}$  takes the form

$$\gamma_{\text{eff}} = k^2 / (ak^4 + bk^2 + c) + 1/(a'k^2 + b'), \quad (7)$$

where again  $a, b, c, a', b'$  are determined by the various material parameters. The latter case describes, for example, an  $n$ -type material for which  $L_{ed} > \Lambda > L_{hd}$ . The condition  $L_{ed} > L_{hd}$  definitely holds in undoped and phosphorous-doped  $a$ -Si:H where (assuming the Einstein relation<sup>10</sup>) one would expect that  $D_e \theta_n > D_h \theta_p$  (since<sup>15</sup>  $\mu_e \theta_n > 10 \mu_h \theta_p$ ). Hence in discussing  $n$ -type  $a$ -Si:H we do not have to use the most general expression for the parameter  $f$  [Eq. (4)] and we may consider the three simpler cases that yield the  $\gamma_{\text{eff}}$  results given by Eqs. (2), (6), and (7). The important point to realize is that unlike the ambipolar case given by Eq. (2), the cases described by Eqs. (6) and (7) yield a maximum in the  $\gamma_{\text{eff}}$  vs  $k^2$  dependence. Hence a presence of such a maximum in the experimental data is a clear signature of nonambipolar transport. A more detailed discussion of the various coefficients in Eqs. (6) and (7) will be given elsewhere.

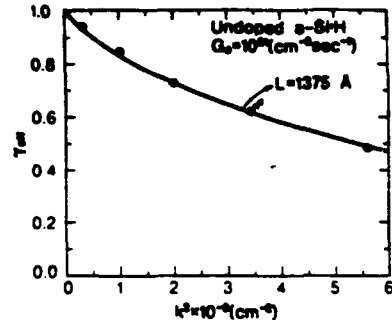


FIG. 1. The measured dependence of the normalized grating amplitude  $\beta$  on the squared wave-vector of the photocarrier grating, as obtained on undoped device quality  $a$ -Si:H.

Let us estimate now the magnitude of the parameter  $f$  [Eq. (4)] and the corresponding expected  $\gamma_{\text{eff}}$  vs  $k^2$  dependence. In trying to quantify  $f$  one notes that we do not know the values of  $D_e$  and  $D_h$  in  $a$ -Si:H and even for  $\mu_e$  and  $\mu_h$  we have only rough estimates. However the order of magnitude of these quantities is quite well established<sup>16</sup> as  $\mu_e \approx 10 \text{ cm}^2/\text{V s}$  and  $\mu_h \approx 1 \text{ cm}^2/\text{V s}$ . Assuming the Einstein relations one can then estimate that  $D_e = (k_B T/q) \mu_e \approx 0.25 \text{ cm}^2/\text{s}$  and that  $D_h = 0.025 \text{ cm}^2/\text{s}$ . Consideration of Fermi-Dirac statistics<sup>14</sup> and our knowledge of the band-tail widths<sup>16</sup> are not expected to increase these values by more than a factor of 3. The photoconductivity is well known for device quality<sup>5</sup>  $a$ -Si:H; for a generation rate of  $10^{21} \text{ cm}^{-3} \text{ s}^{-1}$  (1-sun intensities) it is of the order of  $\sigma_0 = 10^{-4} (\Omega \text{ cm})^{-1}$ . Since for  $a$ -Si:H,  $\epsilon = 10^{-10} \text{ F m}^{-1}$  and since in the typical grating geometry  $\Lambda \approx 1 \mu\text{m}$ , we find that under the above conditions  $f$  of Eq. (4) is of the order of

$$f \approx (10^8/\theta_p + 10^8) / (10^8/\theta_n + 10^9). \quad (8)$$

For obtaining the ambipolar limit, i.e., in order that the  $\gamma_{\text{eff}}$  ( $k^2$ ) dependence given by Eq. (2) will be maintaining, we must have  $\theta_p < 1$  and  $\theta_n < 10^{-1}$ . These two conditions are definitely fulfilled considering the above values of  $\mu_e$  and  $\mu_h$  and the corresponding values of the drift mobilities.<sup>15</sup>

Turning to the experimental results derived from the measurements on the PCG we note that these results are usually presented by  $\beta(\Lambda)$  plots.<sup>13</sup> Here, however, in order to make a comparison with the predictions (2), (6), and (7), we use the dependence of  $\gamma_{\text{eff}}$  [the values of which are determined from the measured  $\beta$  and relation (1)] on  $k^2$ . In Fig. 1 we show the predicted [Eq. (2)] and the experimentally observed  $\gamma_{\text{eff}}$  vs  $k^2$  dependence for device quality, undoped  $a$ -Si:H. In the present case we found<sup>3</sup> that  $\gamma_0 \gamma^{1/2} = 0.91$  which is consistent with the independent determination of  $\gamma$  ( $= 0.85$ ). The excellent agreement between these results and the predicted behavior of Eq. (2), as well as the above-mentioned expectation from Eq. (8), seem to confirm our suggestion<sup>9</sup> that the small values of  $\theta_n$  and  $\theta_p$  are the reason for the ambipolar behavior in the PCG imposed on undoped  $a$ -Si:H. This proof is, however, incomplete since it could be that the experimentally observed Eq. (2)-like behavior is "universal" and has nothing to do with our  $f$  parameter. In particular, this possi-

bility cannot be ignored since no other experimental  $\gamma_{\text{eff}}$  vs  $k^2$  dependence has been reported in the literature<sup>1-7</sup> thus far. In order to provide a decisive proof for the applicability of the theory,<sup>9</sup> and the meaning of  $f$  as outlined above, one has to show that being guided by our expression for  $f$  [Eq. (4)] it is possible to obtain experimentally nonambipolar behaviors such as those given by Eqs. (6) and (7). In other words, one has to show that by upsetting the fulfillment of the conditions for  $L_{\text{ad}}$  or for  $L_{\text{hd}}$  one can obtain a deviation from the ambipolar behavior given by Eq. (2).

We have chosen to demonstrate a nonambipolar behavior by using a doped material. Our approach is based on the finding<sup>15</sup> that with a few ppm of phosphorous doping the drift mobility of the electrons increases while the drift mobility of the holes does not, i.e.,  $\theta_n$  increases while  $\theta_p$  does not. On the other hand, it is known that such doping causes an increase in the photoconductivity. In order to offset this increase we have used thinner films (4200 Å instead of 2  $\mu\text{m}$ ) than those used for the undoped  $a\text{-Si:H}$  films.<sup>17</sup> Hence, for the doped films, the first term in the numerator and the second term in the denominator of Eqs. (4) and (8) become dominant. Correspondingly we expect a nonambipolar  $\gamma_{\text{eff}}$  vs  $k^2$  dependence [as given by Eq. (7)], i.e., an apparent peak in the corresponding plot. The results shown in Fig. 2 confirm this expectation. In turn, this observation proves the results of our general theory,<sup>9</sup> the meaning of the "ambipolarity" coefficient  $f$ , and our conjecture regarding the importance of  $\theta_n$  and  $\theta_p$ .

Another extreme nonambipolar case may be expected in very thin films of  $a\text{-Si:H}$  where the high defect density<sup>18</sup> (or the strong effect of the surface recombination velocity) is expected<sup>19</sup> to yield low values for  $\sigma_0$  and  $L$ . Correspondingly we have chosen an undoped 250-Å film in which  $\mu\tau$  is three orders of magnitude smaller than in our 2- $\mu\text{m}$  undoped film. For this case one would expect, on the basis of the above large difference in the majority-carrier  $\mu\tau$ 's, the behavior characterized by Eq. (6). Carrying out the  $\gamma_{\text{eff}}$  vs  $k^2$  measurement on these films has confirmed the expectation for a nonambipolar transport. This can be seen by the predicted presence of a corresponding peak in Fig.

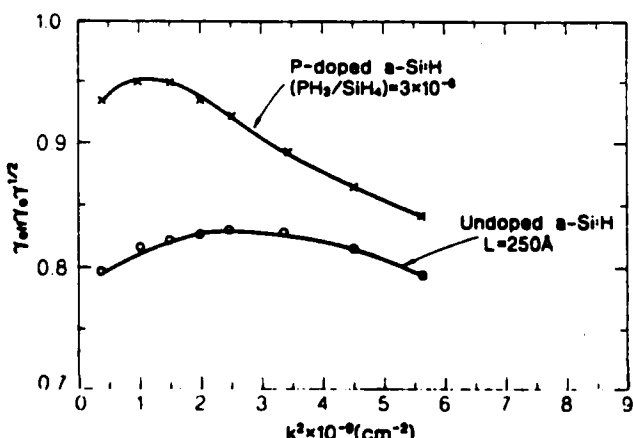


FIG. 2. The measured dependence of the normalized grating amplitude on the squared-wave vector of the photocarrier grating as obtained for a doped sample ( $\text{PH}_3/\text{SiH}_4 = 3 \times 10^{-6}$ ) and a very thin undoped sample of  $a\text{-Si:H}$ . Note that  $\gamma_0$  is a constant (of order 1) and thus the qualitative contrast between the results shown in this figure and those shown in Fig. 1 is apparent.

2. Hence the guidance provided by our ambipolarity coefficient<sup>9</sup>  $f$  is shown again to have a predictive power for the ambipolarity test.

In conclusion, we have shown theoretically and experimentally that a nonmonotonic decrease of the normalized grating amplitude with the squared grating-wave vector is a signature of a nonambipolar transport in the PCG. Our procedure provides, then, an immediate qualitative test for the interpretation of the results in terms of the ambipolar diffusion length. A quantitative application of the ambipolarity factor  $f$  further confirms that the claim made in the many reports, in which the value of  $L$  was derived from PCG measurements on undoped  $a\text{-Si:H}$ , is justified, and that the reason for this is the high trapping rate in this material.

This work was supported in part by the U.S.-Israel Binational Science Foundation and in part by the U.S. Army Research Office, Grant No. DAAL-03-89-6-0114. The authors are indebted to A. Catalano, K. Epstein, and B. Nelson for samples used in this study.

- D. Ritter, E. Zeldov, and K. Weiser, *Appl. Phys. Lett.* **49**, 791 (1986).
- G. H. Bauer, C. E. Nebel, and H. D. Mohring, *Mater. Res. Symp. Proc.* **118**, 679 (1988).
- I. Balberg, A. E. Delahoy, and H. A. Weakliem, *Appl. Phys. Lett.* **53**, 992 (1988).
- Z. Liu, A. Maruyama, S. Wagner, and A. Delahoy, *J. Non-Cryst. Solids* **114**, 363 (1989).
- L. Yang, A. Catalano, R. R. Arya, and I. Balberg, *Appl. Phys. Lett.* **57**, 908 (1990).
- G. Mao, H. Fritzsche, K. Chen, and D. Feng, *Bull. Am. Phys. Soc.* **35**, 348 (1990).
- E. Sauvain, A. Shah, and J. Hubin, in *Proceedings of the XI IEEE Photovoltaic Specialists Conference* (IEEE, New York, 1990), p. 1560. Note that in that work deviation from ambipolarity has to do with the application of a relatively high electric field (see also Ref. 4) but the high-electric-field measurements are not suitable for the derivation of the value of  $L$  [see I. Balberg, *Phys. Rev. B* **44**, 1628 (1991)]. In the present paper we consider the case where the drift field used in the measurements is much smaller than the "diffusion field" of 1600 V/cm. For the "diffusion case" discussed here, Sauvain and co-workers state explicitly that they did not see deviations from ambipolarity.
- M. Hack and M. Shur, *J. Appl. Phys.* **58**, 997 (1985).
- I. Balberg, *J. Appl. Phys.* **67**, 6324 (1990).
- R. A. Smith, *Semiconductors* (Cambridge University Press, London, 1961), Chap. 8.
- A. R. Moore, in *Semiconductors and Semimetals*, edited by J. I. Pankove (Academic, New York, 1984), Vol. 21, Pt. C, Chap. 7.
- Actually this expression is very general as was shown by R. S. Crandall, in *Semiconductors and Semimetals*, edited by J. I. Pankove (Academic, New York, 1984), Vol. 21, Pt. B, Chap. 8.
- Note that the band mobility of the carrier (e.g.,  $\mu_e$ ) describes the mobility of the free carrier while the drift mobility of the carrier (e.g.,  $\mu_e\theta_n$ ) describes the mobility of all (free and trapped) carriers. This is seen immediately from the fact that  $\mu_e\theta_n = \mu_e\theta_n(N + n_0)$ . See also, R. S. Crandall and I. Balberg, *Appl. Phys. Lett.* **58**, 508 (1991).
- D. Ritter, E. Zeldov, and K. Weiser, *J. Non-Cryst. Solids* **97-98**, 619 (1987); *Phys. Rev. B* **38**, 8296 (1988).
- R. A. Street, *Appl. Phys. Lett.* **41**, 1060 (1982); R. A. Street, J. Zesch, and M. J. Thompson, *ibid.* **43**, 672 (1983).
- See, for example, J. Abelson, *J. Non-Cryst. Solids* **114**, 450 (1989).
- For these two thicknesses the photoconductivity is smaller in the thinner samples by about an order of magnitude. See, for example, H. Curtins, M. Favre, Y. Ziegler, N. Wyrach, and A. V. Shah, *Mater. Res. Symp. Proc.* **118**, 159 (1988).
- H. Curtins and M. Favre, in *Amorphous Silicon and Related Materials*, edited by H. Fritzsche (World Scientific, Singapore, 1988), p. 329.
- L. Yang, I. Balberg, A. Catalano, and M. Bennett, *Mater. Res. Symp. Proc.* **192**, 243 (1990).

# High-energy LMM Auger Transitions

S. Z. Weiss, M. Gomez and O. Resto

Department of Physics, University of Puerto Rico, Rio Piedras, PR 00931, USA

A. Many and Y. Goldstein\*

Racah Institute of Physics, The Hebrew University, Jerusalem, Israel

We have recently shown that with the commonly available resolution in Auger electron spectroscopy measurements, significant errors can be incurred in the measured Auger line intensities. To overcome this difficulty, a universal relation has been derived theoretically whereby the experimentally measured line intensities can easily be corrected so as to yield good estimates for the true intensities, i.e. those that would have been measured were the resolution infinitely good. The validity of our correction procedure was recently demonstrated for the high-energy KLL and low-energy LMM lines of Si, Al and Mg as well as for the high-energy LMM and low-energy MNN lines of Cu. In this paper we extend these studies to the high-energy LMM lines of Zn, Ge, Fe, Co and Ni. We present here the intrinsic lineshapes of these lines as well as the Auger sensitivities relative to silver, measured with different resolutions. The correction procedure applied to the data yields the true sensitivities to a good approximation and is therefore important for quantification and for theoretical calculations of Auger yields.

## INTRODUCTION

When the resolution width used in measurements of Auger electron spectroscopy (AES) becomes comparable to or larger than the intrinsic Auger linewidth, the signal intensity is no longer a linear function of resolution.<sup>1,2</sup> As a result, atomic concentrations derived from line intensity measurements usually depend on the resolution used, a situation that is detrimental for quantification. Since the resolution width is usually proportional to the Auger energy, this effect is more pronounced in measurements of high-energy Auger lines. Contrary to the common belief (see e.g. Ref. 3) that the width of the Auger lines is of the order of 3–4 eV, the widths of the high-energy lines of many elements are below 1 eV,<sup>4</sup> a fact that enhances the dependence of the measured concentrations on the resolution used.

In order to overcome these difficulties, we have derived<sup>1,2</sup> a universal relation whereby the experimentally measured peak-to-peak amplitudes of the differentiated Auger signal, referred to as the 'derivative amplitude', can easily be corrected so as to represent quite accurately in most cases the true value of the derivative amplitude. All that is required is to multiply the as-measured amplitude for the line of each element 'EI' by  $1 + [W_i(EI)/W_i(EI)]^2$ . Here  $W_i(EI)$  is the intrinsic width of the line and  $W_i(EI)$  is the resolution width at the line's energy<sup>1,2</sup> (see below). Thus the *corrected* sensitivity  $S_{corr}$  relative to a standard line 'Si' (such as silver) is related to the corresponding as-measured sensitivity  $S_{meas}$  by

$$S_{corr} = FS_{meas} \quad (1)$$

where the correction factor  $F$  is given by

$$F = \frac{1 + [W_i(EI)/W_i(EI)]^2}{1 + [W_i(Si)/W_i(Si)]^2} \quad (2)$$

Strictly speaking, our analysis is valid for Gaussian lineshapes, but it is usually quite adequate, with somewhat reduced accuracy, for more complex lineshapes as well.

In this paper we display the intrinsic lineshapes of the high-energy LMM lines of Zn, Ge, Fe, Co and Ni as obtained from extremely high-resolution measurements. In addition, we present the atomic sensitivities at different resolutions. The combined data lead to the corrected, true sensitivities of these elements.

## EXPERIMENTAL

The samples studied, together with the silver standard, were mounted simultaneously in the vacuum chamber of a Physical Electronics model 560 Auger microprobe. Their surfaces were cleaned by argon ion bombardment. Two modes of operation were used in the AES measurements, the 'ESCA (electron spectroscopy for chemical analysis) mode' and the 'Auger mode'. In both modes an electron beam was used to excite the Auger transitions. In the ESCA mode a retarding field is applied to the Auger electrons so that they enter the analyser at a low (constant) energy. The resolution attained in this mode was extremely high, amply sufficient to measure accurately the natural shapes and intrinsic widths of all lines. The intrinsic width  $W_i$  of each line is given at this high resolution by the energy separation between the positive and negative peaks of the Auger derivative.

Unfortunately, our ESCA mode is unsuitable for quantitative intensity measurements because of losses in beam intensity introduced by the retarding field. Such losses have a complicated dependence on energy, so that a quantitative comparison of derivative amplitudes for different Auger lines is unfeasible. The derivative amplitudes were therefore measured in the usual Auger mode, i.e. without the application of the retarding field. In addition, this is the mode commonly used in quantitative analyses and is hence of more interest. The

MARKED *LET 2*  
PLEASE RETURN

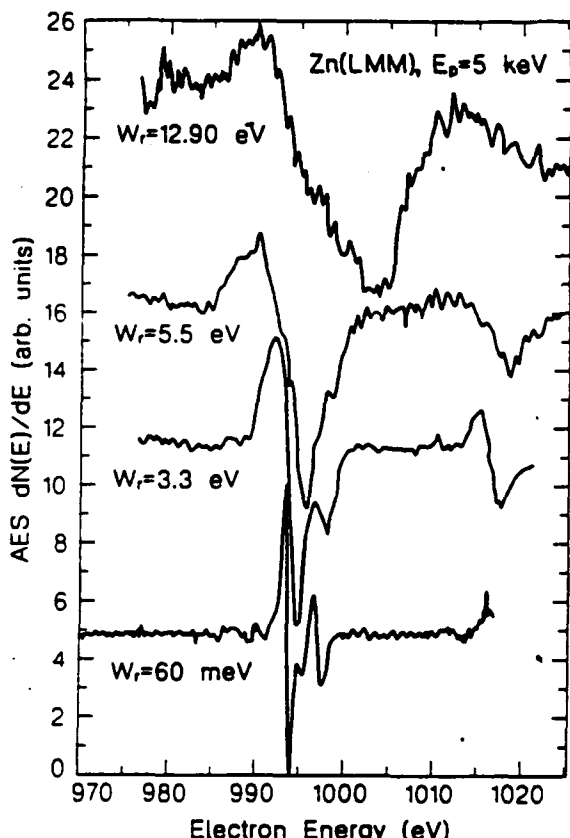


Figure 1. Derivative spectra of the Zn LMM line in the ESCA mode (bottom curve) and in the Auger mode at three different resolutions (three upper curves).

resolution was varied by adjusting the analyser apertures. In this manner three resolutions were obtained, around 0.3%, 0.6% and 1.3% of the Auger energy  $E$ . Care was taken at each setting to perform the measurements on the different samples under identical experimental conditions. The measurements were carried out

with a primary beam energy of 5 keV. The derivative spectra were obtained by nine-point computer differentiation of the measured  $N(E)$ -spectra.<sup>3</sup> The measurement steps were sufficiently fine (either 0.05 or 0.1 eV) that the 'differentiation potential'<sup>4</sup> was always less than 0.7 of the measured widths of all the Auger lines studied. Hence this procedure yielded accurate values for the derivative spectra<sup>4</sup> in as far as the differentiation procedure is concerned.

The resolution width  $W_r$  was determined<sup>2</sup> by differentiating the signal originating from the elastically scattered electrons at a sufficiently high primary beam energy ( $\sim 2$  keV) and measuring the separation between the positive and negative peaks. In some measurements  $W_r$  was determined by measuring the actual width of an Auger line of narrow and known intrinsic width. The measured width  $W_m$  is related to  $W_r$  and  $W_i$  by

$$W_m^2 = W_r^2 + W_i^2 \quad (3)$$

Obviously  $W_m = W_r$  in the limit of infinitely good resolution ( $W_r \ll W_i$ ), while for an infinitesimally narrow line ( $W_i \ll W_r$ )  $W_m = W_r$ . Since  $W_r$  is proportional to energy, its value at any Auger line can readily be evaluated.

## RESULTS

The silver line, used as the standard, and all the high-energy LMM lines studied were measured both in the ESCA mode (resolution width  $W_r$  either 60 or 120 meV) and in the Auger mode at three different resolutions (0.33%, 0.55% and 1.3% of the line energy). The detailed lineshape of the silver line has been reported previously.<sup>4</sup> Figure 1 displays the evolution of the Zn LMM lineshape as the resolution is degraded from that in the ESCA mode (bottom curve,  $W_r = 60$  meV) to those of the Auger mode (three upper curves). The curves in the figure were shifted along the y-axis and the line intensities were normalized to 10. As seen in the

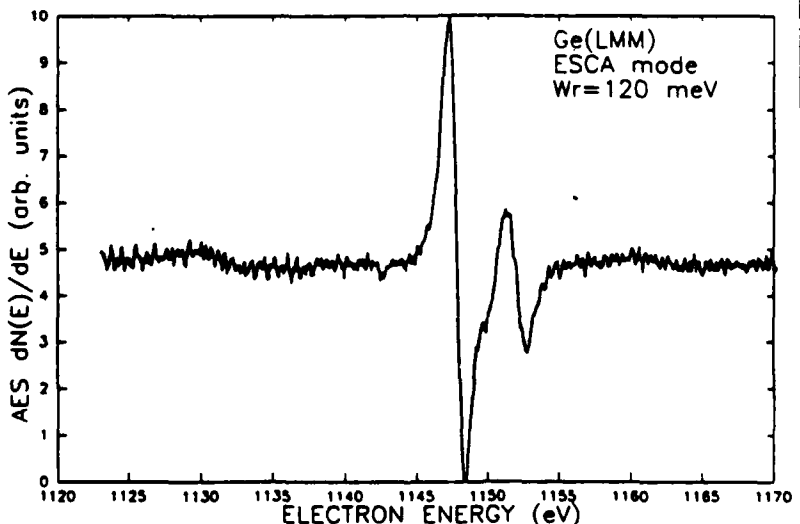


Figure 2. The Ge LMM line measured in the ESCA mode.

HIGH-ENERGY LMM AUGER TRANSITIONS

MARKED SET  
PLEASE RETURN  
178 300

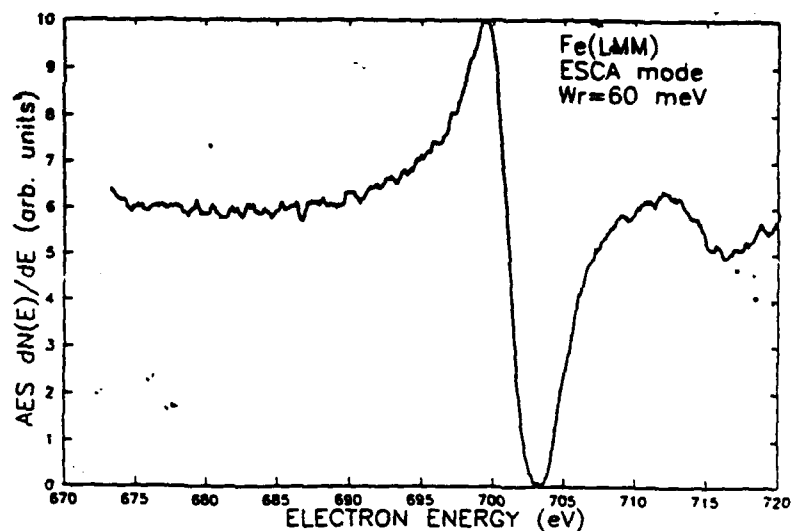


Figure 3. The Fe LMM line measured in the ESCA mode.

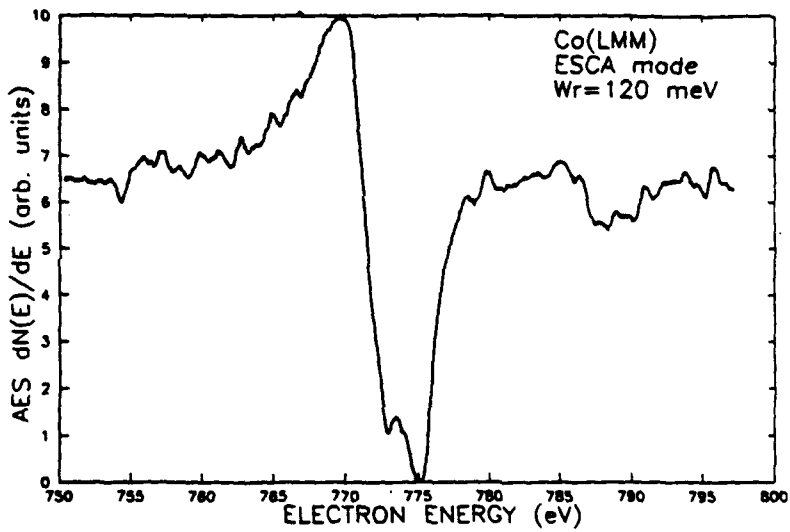


Figure 4. The Co LMM line measured in the ESCA mode.

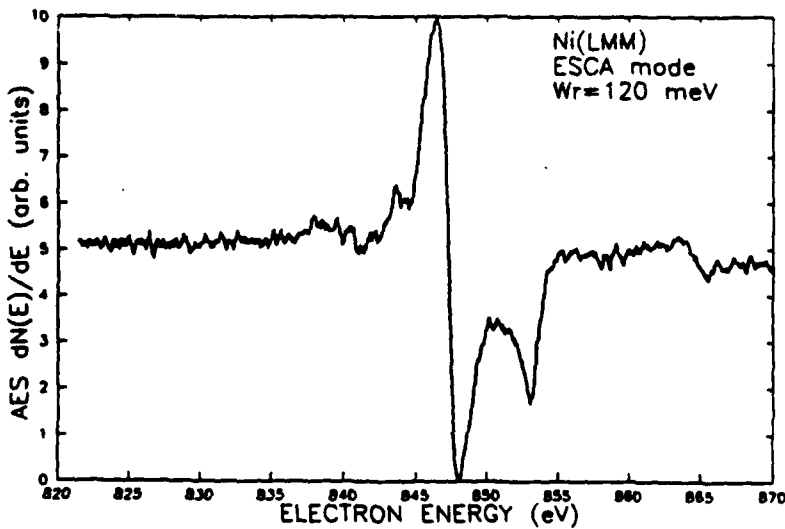


Figure 5. The Ni LMM line measured in the ESCA mode.

MARKED - 3  
PLEASE RETURN

bottom curve of Fig. 1, the zinc line is intrinsically very narrow (0.65 eV) and has a satellite about 3 eV above the main line. The satellite is still resolved (with lower amplitude) in the first upper curve ( $W_i = 3.3$  eV), our best resolution in the Auger mode, but is completely washed out in the much poorer resolutions of the two uppermost curves.

Figures 2-5 display the intrinsic lineshapes of the high-energy LMM transitions of the rest of the elements studied, as measured in the high-resolution ESCA mode. The line intensities in these figures were normalized to full scale. We note that the Ge LMM line (Fig. 2), just like the Zn LMM line (Fig. 1), is intrinsically very narrow (1 eV). Such linewidths are characteristic also of the KLL lines reported previously.<sup>4</sup> In contrast, the LMM lines of the three transition metals are appreciably wider, as can be seen in Figs 3-5.

Measurements in the Auger mode, such as those displayed in Fig. 1, together with those of the silver line (not shown here) were used to determine the derivative amplitudes of the different lines and, through their ratios, the atomic sensitivities. The as-measured sensitivities  $S_{\text{meas}}$  of the Zn and Ge lines relative to Ag at three resolutions are depicted by the open symbols in the semilogarithmic plots of Fig. 6. As expected, the as-measured sensitivities decrease as the resolution is degraded. The full symbols represent the corrected sensitivities  $S_{\text{corr}}$ , obtained by the use of Eqns (1) and (2) with  $W_i(\text{Ag}) = 1.3$  eV.<sup>4</sup> These are seen to be constant to within 10%-20%, independently of resolution. The horizontal lines depict the averages of the corrected sensitivities for the two elements. The curves below represent the calculated dependences of  $S_{\text{corr}}$  on resolution, as evaluated from Eqns (1) and (2), and are seen to fit well the measured points. These curves immediately indicate what values of  $S_{\text{corr}}$  are to be expected at any resolution. For the case at hand one would need a resolution of 0.01% or so in order to measure the true sensitivities. Obviously such resolutions are unattainable by far in AES measurements. Hence one has no recourse but to use the correction method described here if one wishes to arrive at reasonable estimates for the true sensitivities.

Similar plots are displayed in Fig. 7 for the Ni and Fe lines. The correction factors for Ni are smaller than

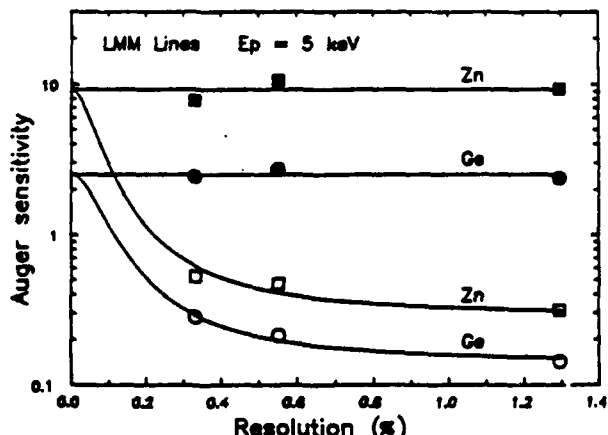


Figure 6. As-measured and corrected sensitivities of the LMM lines of Zn and Ge relative to the MNN line of Ag as functions of instrumental resolution.

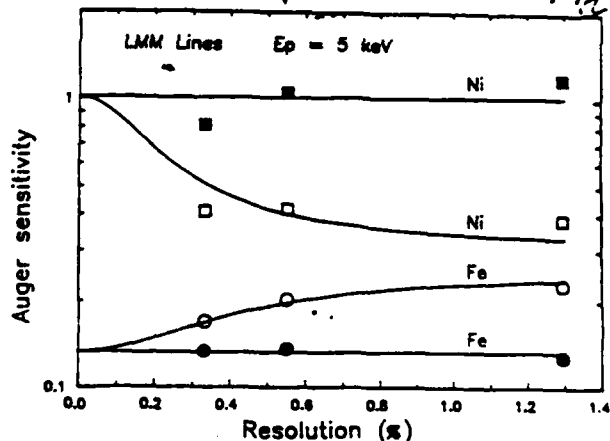


Figure 7. As-measured and corrected sensitivities of the LMM lines of Fe and Ni relative to the MNN line of Ag as functions of instrumental resolution.

those for Zn and Ge owing to the larger width of the Ni line (1.75 eV). The agreement with theory in this case is not very good. This is not surprising since the Ni line is far from Gaussian (see Fig. 5). Hence the correction procedure yields only a rough estimate of the true sensitivity, yet the divergence in the corrected sensitivities does not exceed 20%-30%. The Co line is also non-Gaussian (see Fig. 4) and the agreement of the sensitivity values with theory is similarly poor. As for the Fe line, the agreement with theory is quite good, as expected in view of its Gaussian lineshape (see Fig. 3). It should be noted that here the corrected sensitivities are lower than the as-measured sensitivities. This is because the width of the Fe line (3.6 eV) is much larger than the width of the Ag line (1.3 eV), so that the correction of the silver intensity is larger than that of the Fe line intensity (see Eqns (1) and (2)).

The main results for Zn, Ge, Fe, Co and Ni are summarized in Table 1. The table lists the intrinsic widths  $W_i$  of the lines, as obtained from Figs 1-5, the as-measured sensitivities relative to Ag at three resolutions and the average corrected sensitivities  $\langle S_{\text{corr}} \rangle$ .

Table 1. As-measured sensitivities  $S_{\text{meas}}$  at three resolutions and average corrected sensitivities  $\langle S_{\text{corr}} \rangle$  of the LMM lines of Zn, Ge, Fe, Co and Ni relative to the MNN line of Ag. The data were taken with a primary beam energy  $E_p$  of 5 keV. Also included are the line energies  $E$  and the intrinsic linewidths  $W_i$ .

Element	$E$ (eV)	$W_i$ (eV)	0.33%	0.56%	1.3%	$\langle S_{\text{corr}} \rangle$
Zn	994	0.65	0.53	0.48	0.31	9.3
Ge	1147	1.0	0.29	0.22	0.14	2.5
Fe	703	3.6	0.17	0.20	0.23	0.13
Co	775	4.4 <sup>a</sup>	0.28	0.46	0.46	0.2 <sup>b</sup>
Ni	848	1.75	0.41	0.42	0.39	1 <sup>b</sup>

<sup>a</sup>This value represents the energy separation between the positive peak and the mean of the two negative peaks of the differentiated Auger signal (see Fig. 4).

<sup>b</sup>These values are rough estimates (see text).

## DISCUSSION

The use of the high-resolution ESCA mode with fine steps in the data accumulation provides a detailed picture of the natural lineshapes of all the Auger lines studied. All the lines, except the Fe line, exhibit double peaks or prominent satellites in their close vicinity. Such fine structure should be useful in studying the different initial and final states involved in the Auger transitions (see e.g. Ref. 7).

The narrow widths of the high-energy LMM lines of Zn and Ge (1 eV or less), just like those of the high-energy KLL lines reported previously,<sup>4</sup> are not surprising, since these lines originate from deep level transitions. As a result of the narrow widths, the errors in the as-measured sensitivities are quite large, requiring correspondingly large correction factors. The considerably larger widths of the high-energy lines of Fe, Co and Ni are probably due to the unfilled d-shells in these elements.

The observation that the as-measured sensitivities at different resolutions can vary whereas the corrected sensitivities are the same to within 10%-20% demonstrates once again the validity of our simple correction procedure—this much in spite of the fact that the Auger lines studied were not strictly Gaussian, some deviating quite significantly from a Gaussian lineshape.

The corrected sensitivities provide good estimates for the true sensitivities. They can differ by one to two orders of magnitude from the as-measured values. It is these true sensitivities that the results of any theoretical calculations<sup>8,9</sup> of Auger yields should be compared with. This is particularly important for Auger lines originating from different transitions.<sup>4</sup>

## Acknowledgements

This work was supported in part by National Science Foundation EPSCoR grant RII 8610677 and in part by US Army Research Office grant DAAL03-89-G-0114.

## REFERENCES

1. A. Many, Y. Goldstein, S. Z. Weiss and O. Resto, *Appl. Phys. Lett.* **53**, 192 (1988).
2. Y. Goldstein, A. Many, O. Millo, S. Z. Weiss and O. Resto, *J. Vac. Sci. Technol. A* **8**, 3130 (1988).
3. J. C. Riviere, in *Practical Surface Analysis by Auger and X-ray Photoelectron Spectroscopy*, ed. by D. Briggs and M. P. Seah, p. 72, Wiley, Chichester (1983).
4. S. Z. Weiss, O. Resto, Y. Goldstein and A. Many, *J. Vac. Sci. Technol. A* **8**, 3198 (1990), A. Many, Y. Goldstein, S. Z. Weiss and O. Resto, *Vacuum* **41**, 1805 (1990).
5. A. Savitsky and M. J. E. Golay, *Anal. Chem.* **36**, 1627 (1964).
6. M. P. Seah, M. T. Anthony and W. A. Dench, *J. Phys. E: Sci. Instrum.* **16**, 848 (1983).
7. M. Salmeron, A. M. Baro and J. M. Rojo, *Surf. Sci.* **53**, 689 (1975), and references cited therein.
8. S. Mroczkowski and D. Lichtman, *J. Vac. Sci. Technol. A* **3**, 1860 (1985), and references cited therein.
9. C. J. Powell, *Rev. Mod. Phys.* **48**, 33 (1976).

# THEORETICAL AND EXPERIMENTAL DEVELOPMENTS IN THE DETERMINATION OF THE MINORITY CARRIER PROPERTIES IN LOW MOBILITY SEMICONDUCTORS

L. Balberg

The Racah Institute of Physics, The Hebrew University, Jerusalem, Israel

S.Z. Weisz

Physics Department, University of Puerto Rico, Rio Piedras, Puerto Rico

Until the recent development of the photocarrier grating (PCG) method it was impossible to follow the phototransport properties associated with minority carriers in materials in which the diffusion length of these carriers is in the submicron range. The two systems in which significant knowledge of the minority carrier properties have already been extracted by the application of the PCG are amorphous silicon and polycrystalline Cu-ternary-chalcopyrites. While the basic physics of the method is well understood the interpretation of its experimental results, in terms of the microscopic transport and recombination mechanisms, is not settled. In this presentation we give a short review of the present understanding of the PCG method and its application to the above materials.

## I. INTRODUCTION

The special feature which singles out semiconductors from other materials is that the electrical conduction in those materials is carried out by two types of carriers. The carrier which dominates this conduction is known as the majority carrier. On the other hand the other, minority, carrier is the carrier which controls the electrical behavior of inhomogeneous semiconductors in general, and in semiconductor devices in particular. Hence, in addition to the interest in the basic physics of the electronic structure and the transport mechanism associated with the minority carrier, there is a strong motivation to study the properties of this carrier from the device physics point of view. Correspondingly an intensive effort was made in order to characterize the minority carrier properties in semiconductors. Of these properties the minority carrier's diffusion length,  $L_m$ , was studied more than any other parameter.  $L_m$  yields information on both, the transport and the kinetics of the minority carrier, and is the dominant parameter in determining the performance of the well understood and widely used bipolar devices.

It turns out that the many methods which were applied to crystalline semiconductors have used in one way or another the fact that  $L_m \gtrsim 10 \mu\text{m}$ . The development of new, in particular thin film, semiconductors where  $L_m < 1 \mu\text{m}$  has challenged the researchers of those materials to develop suitable methods for the measurement of their  $L_m$ . The first attempts, which were based on methods used for crystalline semiconductors, failed mainly because in the corresponding inhomogeneous configurations the short  $L_m$  could not be separated from the drift length contribution due to the presence of internal electric fields<sup>2</sup>.

A breakthrough in the possibility of the measurement of  $L_m$  came when Ritter, Zeldov and Weiser<sup>3</sup> suggested the use of a photocarrier sinusoidal grating which is based on the possibility of comparing  $L_m$  with a variable carrier-concentration grating period  $\Lambda$ . It is obvious then that for  $L_m \gg \Lambda$  the existence of the grating does not effect the measured photoconductivity,  $\sigma_g$ , while otherwise  $\sigma_g$  is effected by the presence of the grating. The relation between  $\sigma_g$  and  $\Lambda$  yields<sup>3</sup> then the value of  $L_m$ . It took however three years, after the work of Ritter et al<sup>3</sup>, to prove experimentally that indeed the length parameter determined from the measurement,  $L$ , is associated with the minority carriers<sup>4</sup>. The exact relation between  $L$  and  $L_m$  is still however a matter of intensive discussion. On the other hand the latter experimental proof enabled the utilization of the PCG technique to resolve many material-physics and device-physics issues in hydrogenated amorphous silicon<sup>4</sup> (a-Si:H) and Cu-ternary chalcopyrites<sup>5</sup> (CuInSe<sub>2</sub> and CuGaSe<sub>2</sub>).

## II. THEORETICAL DEVELOPMENTS

The basic physical picture of the photocarrier grating formed by a small sinusoidal carrier generation grating, which is superimposed on a much larger uniform generation background, is now well understood<sup>6</sup>. Quantitatively, it is generally agreed that the length  $L$  derived from the PCG measurement can be written as<sup>6</sup>:

$$L = \sqrt{2Dt} \quad (1)$$

where  $D$  is some "effective" diffusion coefficient and  $t$  is some "effective" small signal recombination time that can be written (for high enough  $\sigma_g$  values) as<sup>3,6</sup>:

$$1/t = (\partial U / \partial n)_p + (\partial U / \partial p)_n, \quad (2)$$

where  $U$  is the common, two carrier, recombination rate in the uniform background of the electron ( $n$ ) and hole ( $p$ ) concentrations. Until recently even Eq. (1) was in doubt since it is not obvious that a small superimposed sinusoidal carrier generation will yield a small superimposed sinusoidal carrier concentration<sup>6</sup>. The questions of present debate<sup>7,8</sup> are the meanings of an "effective"  $D$  and an "effective"  $t$ . These concepts depend of course on the set of assumptions made in the theoretical calculations, and their justification, when applied to a given material and under given conditions. We list here the set of assumptions made in order to get the simplest expression for  $L$  in terms of the microscopic parameters of the material, and we refer to objections<sup>6-8</sup> made regarding this set.

In the value of  $D$  the question is whether one should consider only shallow trapping or whether deep trapping should also be included<sup>7</sup>. The other question<sup>8</sup> is whether the quasi Fermi level (or the carrier generation rate) effects the value of  $D$  and whether one can assume the fulfillment of the Einstein relation in systems studied thus far by the PCG<sup>3</sup>. The expression for  $t$  is even more problematic since one has to assume a priori a recombination mechanism and thus an explicit expression for  $U$ . Also, as with the quantity  $D$ , the question of which trapping should be considered is

still open<sup>6-8</sup>. Correspondingly the interpretation of the value of  $L$  and its light intensity and temperature dependences, in terms of electronic structure and transport mechanism, is determined by the assumptions made regarding the material under study. The simplest assumptions are the fulfillment of the Einstein relation, constant carrier mobilities, only shallow (or no) trapping, and a Shockley Read recombination mechanism<sup>3,6</sup> (single level,  $n$ ,  $p \ll P_r, N_r$  where  $P_r$  and  $N_r$  are the corresponding concentrations of available recombination centers). These assumptions yield the expression:

$$L^2 = (2kT/q)[\mu_e \mu_h \tau_n \tau_p] / [\mu_e \tau_n + \mu_h \tau_p], \quad (3)$$

where,  $kT$  is the thermal energy,  $q$  is the electronic charge,  $\mu_e(\mu_h)$  is the electron (hole) mobility and  $\tau_n(\tau_p)$  is the electron (hole) recombination time in the uniform background of the two carriers. One notes of course that if the minority carriers are the holes ( $\mu_h \tau_p \ll \mu_e \tau_n$ ) this expression is reduced to  $L^2 = (2kT/q)\mu_h \tau_p$  and thus the assumption:

$$L = L_m \quad (4)$$

is fulfilled. As stated out above there is currently sufficient experimental data<sup>4,9</sup> to assume that Eq. (4) is a fairly good approximation for the materials studied thus far. However the accuracy of this relation is definitely an open question and so is the physical information that can be extracted regarding the recombination process<sup>4,7,8</sup>.

### III. EXPERIMENTAL DEVELOPMENTS

At present there are some twenty PCG experimental systems in the world, which except for some minor details are similar to the system used initially<sup>9</sup>. The photocarrier generation grating is created by the interference of two coherent laser beams, which are of very different light intensities. Hence the generation of a large uniform carrier background and a small superimposed, sinusoidal, carrier grating which has a submicron period<sup>3,4</sup>. The initial experimental results obtained by the PCG method yielded observations which appear to be contrary to expectations<sup>1</sup>. The variation of  $L$  with the variation of materials was found to be over a narrower range than the corresponding change in the majority carrier  $\mu\tau$  product, the ratio  $\mu_h \tau_p / \mu_e \tau_n$  was found to be much larger than the one observed in time-of-flight measurements, and the light intensity exponents were found to be different for  $L^2$  and  $\mu_e \tau_n$  in contrast with the expectations<sup>6</sup> from the simple Shockley Read model. It turns out<sup>4</sup> that the first observation is simply a result of the  $\Lambda$  range available at present in PCG experimental systems, while the second observation relates only to the oldest sets of data, which were taken in measurements carried out on nearly compensated materials. The third observation is obviously a result of the application of the above Shockley Read approach. One can show that if charge neutrality is considered a one level Shockley Read-like model of recombination can still explain most of the data reported. This is since under this consideration Eq. (2) takes the two term form:

$$1/t = K_1 n + K_2 (N_r + P_r) \quad (5)$$

where  $K_1$  and  $K_2$  are constants. Hence the range of possibilities covered by Eq. (5) is enough to account for the data. In fact for materials where this is not the case it is enough to introduce just one additional (e.g. correlated) recombination center in order to explain the data<sup>4</sup>. At present the proper approach seems to be the one in which the minimum assumptions, necessary to explain the deviations from the behavior given by Eq. (3), are made.

Among the achievements of the applications of the PCG technique to a-Si:H materials we should mention<sup>4</sup>: optimization of materials by finding deposition conditions under which  $L_m$  is maximized, determination of the majority carrier to minority carrier transition (as a function of boron doping), evidence for the existence of safe hole traps, the determination of the dependence of the minority carrier quasi Fermi level on temperature, the surface recombination velocity, the relation between  $\mu_e \tau_n$  and the corresponding quantity in time-of-flight measurements, and the experimental proof that it is the minority carrier which is the limiting carrier in the p-i-n solar cells. In the Cu-ternary-chalcopyrites the PCG yielded the value of  $L_m$  and its relation to the variable crystallite size in the material. Here again conditions were found for maximizing  $L_m$  as a function of composition and deposition parameters<sup>5</sup>.

In conclusion, the PCG is presently the only available method for the experimental study of the phototransport properties of the minority carriers in materials where the corresponding diffusion length is in the submicron regime. The present understanding of the method and its results is definitely sufficient for the understanding of the device physics of the corresponding materials. From the progress made thus far it appears also that additional data and proper theories will enable to make this method an effective tool for the derivation of more detailed information regarding the basic physics of these materials.

**Acknowledgements:** This work was supported in part by the U.S.-Israel Binational Science Foundation, in part by NSF EPSCoR Grant No. EHR-9108775, and in part by U.S. ARO Grant No. DAAL03-89-G-0114.

## REFERENCES

1. J.W. Orton and P. Blood, The Electrical Characterization of Semiconductors: Measurement of Minority Carrier Properties (Academic, London, 1990)
2. P.J. McElheny, J.K. Arch, H.-S. Lin and S.J. Fonash, *J. Appl. Phys.* **64** 1254 (1988).
3. D. Ritter, E. Zeldov and K. Weiser, *Appl. Phys. Lett.* **49** 791 (1986), *Phys. Rev. B* **38** 8296 (1988).
4. I. Balberg, *Mat. Res. Soc. Symp. Proc.* **258** (1992), in press.
5. I. Balberg, D. Albin and R. Noufi, *Appl. Phys. Lett.* **58**, 140 (1991).
6. I. Balberg, *J. Appl. Phys.* **67**, 6329 (1990), *Phys. Rev. B* **44**, 1628 (1991).
7. A. Shah, J. Hubin, and E. Sauvain, *Tech. Digest of the 5th PSEC*, Kyoto (1990), p. 821.
8. K. Hattori, H. Okamoto and Y. Hamakawa, *Rev. B* **45** 1126 (1992).
9. L. Yang, A. Catalano, R.R. Arya and I. Balberg, *Appl. Phys. Lett.* **57** 508 (1990).

## Lineshapes and yields of high-energy Auger lines

S Z Weisz†, M Gomez†, O Resto†, M H Fariast‡, Y Goldstein‡ and A Many‡

† Department of Physics, University of Puerto Rico, Rio Piedras, PR 00931, USA

‡ Racah Institute of Physics, The Hebrew University, Jerusalem 91904, Israel

**Abstract.** We present high-resolution measurements of the Auger  $M_5N_{67}N_{67}$  transitions of Au, Pt and W. All the lines studied are narrower than 2 eV. We also measured the atomic sensitivities for the above Auger transitions with a resolution of 0.4% of the Auger energy (somewhat better than commonly available). With this resolution it is impossible to resolve fine structure and gross errors are incurred in the measurements of Auger signals. We corrected the measured sensitivities with the method developed previously; the correction factors for the sensitivities are around ten. These large factors represent also the errors incurred in the as-measured sensitivities if no correction is applied.

With the commonly available analyser resolution in Auger electron spectroscopy (AES), of about 0.5% of the Auger energy, the lineshapes can be greatly distorted and most of the fine structure obliterated. Large errors can also be incurred in the measured signal intensities [1]. This effect leads to gross errors in the measured atomic sensitivities and hence in the evaluation of cross sections for Auger excitation. In order to overcome these difficulties, we have derived [1] theoretically a universal relation whereby the experimentally measured peak-to-peak amplitudes of the differentiated Auger signal can be corrected so as to represent quite accurately the true atomic sensitivities.

The samples studied were mounted together in the vacuum chamber of a Physical Electronics model 560 Auger microprobe. Two modes of operation were used in the AES measurements [1], the 'ESCA mode' and the 'Auger mode'. In both modes an electron beam was used to excite the Auger transitions. In the ESCA mode, a retarding field is applied to the Auger electrons so that they enter the analyser at a low (constant) energy. The resolution attained in this mode, 200 meV, was very good. Such a resolution, combined with a fine mesh (0.05 eV), was amply sufficient to measure accurately the natural shapes and intrinsic widths of all lines. Unfortunately, our ESCA mode is unsuitable for quantitative intensity measurements [1]. The Auger signals were therefore also measured in the usual Auger mode, with a resolution of 0.4% of the Auger energy. We present results on the highest-intensity MNN lines of Au, Pt and W, corresponding to the  $M_5N_{67}N_{67}$  transitions. In the ESCA mode the lines are well resolved and, in addition to the main peaks, several satellites were observed. The widths of the main peaks and the satellites are less than 2 eV (see table 1). In order to obtain the atomic sensitivities (with respect to Ag), we measured the Auger signals of Au, Pt, W and Ag in the Auger mode. The lines appeared now as single peaks with no discernible fine structure. Their as-measured atomic sensitivities (relative to Ag),  $S_{\text{meas}}$ , are listed in table 1.

The high-energy MNN lines of Au, Pt and W are quite narrow, less than 2 eV. Because of their high energies ( $\sim 1700$ –2000 eV), the commonly available analyser resolution (about 0.5%) in their vicinity would be  $\sim 8$ –10 eV. Obviously, it is impossible to resolve such

**Table 1.** The intrinsic linewidths of the  $M_5N_{67}N_{67}$  transitions of Au, Pt, and W, and their as-measured and corrected atomic sensitivities relative to Ag. The primary electron beam energy was 5 keV and the analyser resolution 0.4%. The effective width of the Ag line used in the calculations of  $S_{\text{corr}}$  was 1.3 eV [1]. Also included are the theoretical values of Mrockowski and Lichtman [2] and those listed in [3].

Element	$E_i$ (eV)	$W_i$ (eV)	$S_{\text{meas}}$	$S_{\text{corr}}$	Theory [2]	Handbook [3]
Au	2015	1.95	0.033	0.27	0.077	0.036
Pt	1960	1.90	0.036	0.30	0.092	0.042
W	1729	1.45	0.076	0.83	0.130	0.080

narrow lines with that kind of resolution. Thus, the only way to obtain the intrinsic lineshape of the lines is by operating the analyser in a very-high-resolution mode, such as the ESCA mode used here. The narrowness of the high-energy lines and the poor analyser resolution in the Auger mode pose another problem, that of how to obtain the true atomic sensitivities associated with the transitions. Our analysis makes it possible to overcome this difficulty even when the resolution is much poorer. All that is needed for a good approximation of the true sensitivity is to multiply the as-measured line intensities by the correction factor [1]  $[1 + (W_r/W_i)^2]$ , where  $W_r$  is the analyser resolution width at the Auger-line energy and  $W_i$  is the natural Auger linewidth. This procedure has to be applied for the transition in question as well as for the standard transition (Ag in this case). The atomic sensitivities are then given by the *corrected* line intensities relative to that of Ag. The fifth column in table 1,  $S_{\text{corr}}$ , lists the values of the corrected sensitivities. We note that they are about an order of magnitude higher than the as-measured sensitivities ( $S_{\text{meas}}$ ). They are also higher than the corresponding theoretical values derived from Mrockowski and Lichtman's [2] calculations and listed in the sixth column of the table (theory). For comparison purposes, we include in the last column the sensitivities taken from [3]. They are fairly close to our as-measured sensitivities obtained with comparable resolution. We wish to stress that the corrected values represent true sensitivities. It is these values that should be compared with theoretical calculations on the one hand, and be used for more accurate quantification of Auger measurements on the other.

### Acknowledgments

This work was supported in part by a National Science Foundation EPSCoR grant EHR-9108775 and in part by US Army Research Office grant DAAL03-89-G-0114. One of us (MHF) acknowledges support by CONACYT.

### References

- [1] Many A, Goldstein Y, Weisz S Z and Resto O 1988 *Appl. Phys. Lett.* **53** 192  
Goldstein Y, Many A, Millio O, Weisz S Z and Resto O 1988 *J. Vac. Sci. Technol. A* **6** 3130  
Weisz S Z, Resto O, Goldstein Y and Many A 1990 *J. Vac. Sci. Technol. A* **8** 3198
- [2] Mrockowski S and Lichtman D 1985 *J. Vac. Sci. Technol. A* **3** 1863
- [3] Davis L E, MacDonald N C, Palmberg P W, Riach G E and Weber R E 1976 *Handbook of Auger Electron Spectroscopy* 2nd edn (Eden Prairie, MN: Physical Electronics)

## STUDY OF a-Si:H USING THE SOLID/ELECTROLYTE SYSTEM

Y. GOLDSTEIN\*, A. MANY\*, S.Z. WEISZ\*\*, J. PENALBERT\*\*,  
W. MUÑOZ\*\* and M. GOMEZ\*\*

\*Racah Institute of Physics, The Hebrew University, Jerusalem 91904, Israel.

\*\*Department of Physics, University of Puerto Rico, Rio Piedras, PR 00931.

### ABSTRACT

Pulsed measurements on the solid-electrolyte system, which proved very useful in the study of crystalline semiconductors, have been found to be equally effective when applied to hydrogenated amorphous Si films. Here, as well, the aSi:H/electrolyte interface is essentially blocking to current flow and, as a result, surface space-charge layers, ranging from large depletion to very strong accumulation conditions, can be induced and studied. In particular, valuable information can be gained on the density of the localized bulk states. Measurements in the depletion range under illumination yield directly the total density of *occupied* states in the entire energy gap. This is very useful in obtaining a quick and reliable assessment of the quality of the amorphous films. In high-grade films we find that the total density of occupied states is around  $10^{18} \text{ cm}^{-3}$ . The data in the accumulation range, on the other hand, provide useful information on *unoccupied* states near the conduction band edge. The blocking nature of the amorphous Si/electrolyte interface is utilized also to apply a sweep-out technique for an accurate determination of  $\mu\tau$ , the product of the electron mobility and lifetime, even when this value is very low. In a rather poor-quality film, for example, we find  $\mu\tau$  to be  $5 \times 10^{-8} \text{ cm}^2/\text{V}$ .

### INTRODUCTION

Considerable effort, both theoretical and experimental, has been devoted to derive the density of states spectra in a-Si:H films [1]. In this paper use is made for this purpose of pulse measurements on the semiconductor/electrolyte (S/E) system. Such measurements, which proved to be very useful in the study of crystalline semiconductors [2-4], have been found to be equally effective when applied to a-Si:H films. The essentially blocking nature of the S/E interface allows one to induce by an applied bias space-charge layers at the a-Si:H surface, ranging from large depletion to very strong accumulation conditions. In this manner, the entire energy gap in the space charge region, together with its localized states, can be swung below and above the Fermi level. At the same time, one can measure the surface space-charge density  $Q_{sc}$  as a function of the barrier height  $V_s$ . In a-Si:H,  $Q_{sc}$  resides predominantly in the localized states (except in strong accumulation conditions), so that the measurements yield, at least in principle, the energy distribution of the density of states.

High-grade, device-quality films are usually close to intrinsic (resistivity  $\sim 10^{10} \text{ ohm}\cdot\text{cm}$ ). Such high-resistivity films cannot be handled by our measurement technique because the surface space-charge capacitance  $C_{sc}$  cannot be charged within the short-duration applied pulse biases. Accordingly, most of the results to be reported here have been obtained under illumination, for which the photo resistivity is typically  $10^5 \text{ ohm}\cdot\text{cm}$  or less. Our measurements in the depletion range are in remarkably good agreement with the theoretical curve that takes into account the presence of localized states [5]. The data thus yield directly the total density of occupied states in the entire energy gap. This is very useful in obtaining a quick and reliable assessment of the quality of the

amorphous films. In high-grade materials we find that the total density of occupied states is around  $10^{18} \text{ cm}^{-3}$ . The results in the accumulation range, on the other hand, provide useful information on the unoccupied states near the conduction-band edge. Analysis of the data in this case, however, is more difficult because surface states are apparently also involved.

The blocking nature of the a-Si:H/electrolyte interface is utilized also to apply a sweep-out technique for an accurate determination of  $\mu\tau$ , the product of the electron mobility and lifetime. The technique is effective over a very wide range of  $\mu\tau$ . In a rather poor-quality film, for example, we have measured a  $\mu\tau$  value as low as  $5 \times 10^{-8} \text{ cm}^2/\text{V}$ .

## EXPERIMENTAL

Device quality a-Si:H films were prepared by rf glow-discharge decomposition of silane. First, a thin n+ layer was deposited on a conducting glass substrate, followed by a 1  $\mu\text{m}$  thick intrinsic film. The n+ layer provides an ohmic contact between the conducting glass and the intrinsic film. The conducting glass was cut into squares of about  $0.5 \text{ cm}^2$  in area and a contact attached to the conducting glass. The wire lead, contact area and the entire sample were masked by epoxy cement, except for a small area ( $\sim 2 \text{ mm}^2$ ) of the film's surface to be exposed to the electrolyte. The sample and a platinum electrode were immersed in an indifferent electrolyte such as  $\text{Ca}(\text{NO}_3)_2$  or  $(\text{NH}_4)_2\text{SO}_4$ . The sample was illuminated through the (transparent) electrolyte by a  $\sim 2 \text{ mW}$  He-Ne laser. The measurement technique has been described elsewhere [3], and will be reviewed only briefly here. A short (0.1–40  $\mu\text{scc}$ ) voltage pulse applied between the Pt and the sample is used to charge up the semiconductor space-charge capacitance. The voltage drop across these electrodes, measured just after the termination of the pulse, represents to a very good approximation the change  $\delta V_s$  in barrier height across the film's space-charge layer induced by the applied pulse. The change  $\delta Q_{sc}$  in space-charge density is obtained from the voltage developed across a series capacitor, again at the termination of the pulse. In general, the induced charge may include also charge leaked across the S/E interface arising from imperfect blocking. Methods have been developed to determine directly the leakage charge and subtract it, if necessary, from the measured charge so as to yield  $\delta Q_{sc}$  [3,4]. In the case of a-Si:H, however, the interface is essentially perfectly blocking over the entire range of barrier heights studied. Pulses of varying amplitude are applied singly, one per data point taken. In this manner electrochemical reactions that may take place at the a-Si:H interface are practically eliminated and, what is more important, damage to the amorphous film is minimized. We found that applying a large number of pulses degrades the material, drastically reducing its resistivity and introducing large trap densities.

In order to derive the  $Q_{sc}$  vs.  $V_s$  curve from the measured  $\delta Q_{sc}$  vs.  $\delta V_s$  data, one has to determine  $V_{so}$  and  $Q_{sco}$ , the quiescent barrier height and space charge density, respectively.  $V_{so}$  is determined quite accurately (to within  $\pm 20 \text{ meV}$ ) from measurements in the depletion range. The entire  $Q_{sc}$  vs.  $V_s$  curve can then be constructed, using the relations  $V_s = V_{so} + \delta V_s$ ,  $Q_{sc} = Q_{sco} + \delta Q_{sc}$ . In what follows the surface electron density  $N_s = Q_{sc}/q$ , where  $q$  is the electronic charge, rather than  $Q_{sc}$ , is plotted against  $V_s$ .

The dark and photo resistance of each sample (between the a-Si:H/electrolyte interface and the n+ contact) was derived from current-voltage characteristics measured at the *onset* of the applied pulse, before the surface space-charge capacitance can be charged through the sample's resistance (see

below). In this manner, the blocking interface is effectively shorted.

## RESULTS AND DISCUSSION

Typical results of the surface electron density  $N_s$  vs. the barrier height  $V_s$ , obtained for an illuminated a-Si:H sample from measurements with a pulse of 3- $\mu$ sec (squares) and 30- $\mu$ sec (circles) duration, are displayed in the semilog plot of Fig. 1. In the depletion range ( $V_s < 0$ ), the  $N_s$  values are negative and, because of the logarithmic scale used, the plots are those of their absolute magnitudes. The free electron concentration under illumination  $n_{bi}$  in the amorphous film has been derived from the measured photoconductivity on the assumption that the electron mobility  $\mu$  is  $10 \text{ cm}^2/\text{Vsec}$  [6,7]. The corresponding theoretical dependence of the surface electron density  $N_s$  on barrier height  $V_s$ , as obtained from a solution of Poisson's equation [5] in the absence of localized states, is shown by the dashed curve. The experimental points are seen to lie well above this curve indicating, as expected for amorphous films, that the space-charge layer in both the depletion and accumulation ranges is dominated by localized states.

When a depletion layer is formed (by an applied negative pulse), free and trapped electrons are expelled from the surface region, leaving behind the positively-charged localized states that make up the immobile space-charge in the depletion layer. Consider first the case of a non-illuminated sample. The first process that occurs following the application of the negative pulse is the expulsion of free electrons from the surface region. As a result, there is a net thermal emission of trapped electrons from localized states into the conduction

band, and the emitted electrons are, in turn, swept away from the space-charge region. Only shallow states, down to 0.3-0.4 eV below the conduction band edge, are able to do so within the measurement time (the pulse duration) [5]. Under illumination, on the other hand, the situation is quite different. Hole-electron pairs are continuously generated by the light. The electrons are expelled from the surface region, while the holes are attracted to the surface where they can recombine with the trapped electrons. In this manner electrons in occupied states throughout the energy gap can be discharged and expelled from the space-charge layer, irrespective of the depth of the states. The only factors that determine which and how many states can release their trapped electrons within the measurement time are the hole capture cross sections of the states and the hole trapping kinetics. Referring to Fig. 1, we see that for a measurement time of 3  $\mu$ sec (squares) only a fraction of the trapped electrons are expelled, but when the pulse duration is extended to 30  $\mu$ sec (circles),

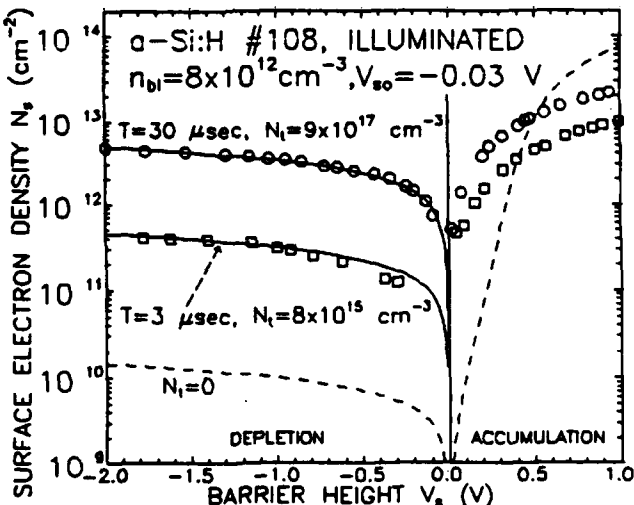


Figure 1. Surface electron density  $N_s$  vs. barrier height  $V_s$  in an illuminated sample of a-Si:H.

practically all occupied states in the depletion layer are discharged and expelled (see below). The solid curves, passing in each case through the points, were calculated from Poisson's equation for the case in which localized states of densities  $N_t$  (as marked) are present [5]. The agreement between theory and experiment is seen to be remarkably good, adding considerable confidence to our analysis. The total density of occupied states in the entire energy gap, as derived from the data for the 30  $\mu$ sec measurement time is about  $10^{16} \text{ cm}^{-3}$ , which is the expected value for the films studied.

When accumulation layers are formed, unoccupied states are filled up. Here again, the experimental points are seen to be initially well above the dashed curve calculated for the case of no localized states present, indicating that localized states dominate the space charge layer in this range as well. Surface states are probably also involved. At stronger accumulation conditions, however, the calculated curve crosses the experimental points and climbs above them. This is not understood at present, and more work is in progress to account for such a behavior. Further studies are needed also to distinguish between surface and bulk states.

It should be noted that the quiescent barrier height is nearly zero. This is to be expected since illumination tends to flatten the bands at the surface [5].

The expelled trap density under depletion conditions, as derived from measurements such as those shown in Fig. 1, is plotted in Fig. 2 against pulse duration (measurement time). The lower two curves were obtained for high-grade a-Si:H films, while the upper curve was obtained after a film has been degraded by the application of many

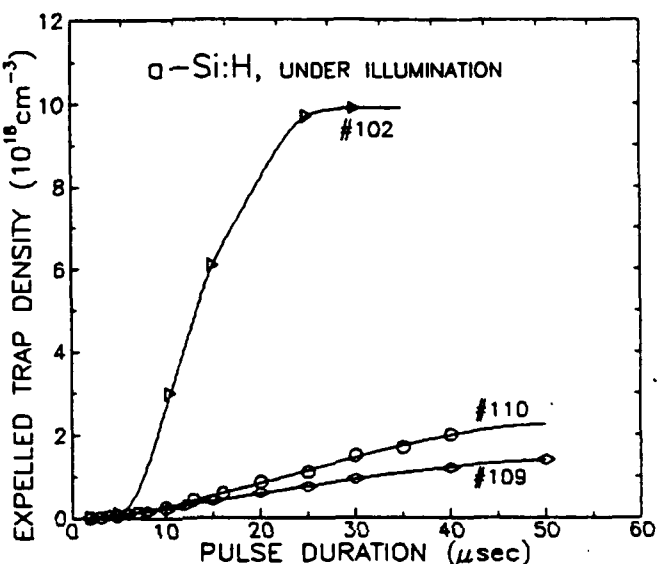


Figure 2. Expelled trap density vs. pulse duration (measurement time) for three a-Si:H samples under illumination.

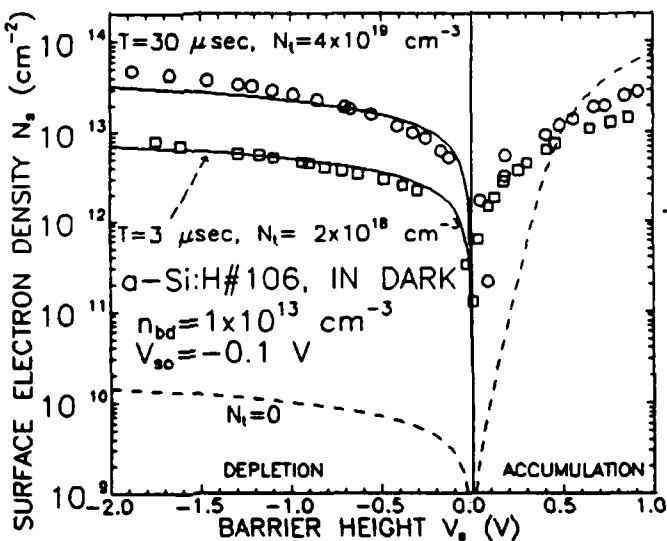


Figure 3. Surface electron density  $N_s$  vs. barrier height  $V_s$  in an unilluminated, degraded sample of a-Si:H.

voltage pulses. In all cases, the expelled trap density increases with pulse duration, but tends to saturate at a pulse duration of 30-40  $\mu$ sec. We interpret the saturation level as representing the total density of occupied states in the energy gap. We are in the process of developing a model involving the hole trapping kinetics in order to account for the shape of the experimental curve. Such a model might yield an estimate of the average cross section for hole capture by the occupied states.

The results depicted in Fig. 3 are similar to those in Fig. 1, except that they were obtained for a non-illuminated sample. The low dark resistivity necessary for the application of our pulse technique has been achieved in this case by degrading the film (see above). Here we find a rather high density of occupied states, as expected for poor-quality material. Since the sample is in the dark, the trapped electrons must now be discharged through thermal emission into the conduction band. As such these states must be not deeper than 0.3-0.4 eV below the conduction-band edge [5].

The dark and photoconductivity of a degraded a-Si:H sample vs. applied pulse voltage is displayed in Fig. 4 on a semilog plot. The measurements were taken at the onset of the pulse, before the space-charge capacitance at the a-Si:H interface can charge up. For positive pulses (electrolyte positive with respect to the n+ contact), the conductivity in both the dark and under illumination is seen to increase with applied voltage. This is due to electron injection from the n+ layer. In the negative polarity, the dark conductivity is independent of voltage, as it should.

The photoconductivity, on the other hand, is seen to decrease with pulse amplitude, approaching the dark conductivity at large negative voltages. We attribute this behavior to electron sweep-out by the applied fields, as shown by the following considerations. The continuity equation [5] for the case of a blocking contact can be written as:

$$dN/dt = L - N/\tau - \mu EN/d, \quad (1)$$

where N is the total density of photo electrons in the sample per  $\text{cm}^2$ , L is the number of hole-electron pairs generated by the light per  $\text{cm}^2\text{sec}$ , E is the applied field and d is the film's thickness. Strictly speaking, the last term in eq. (1) should be  $\mu En_{bl}(d)$ , where  $n_{bl}(d)$  is the electron concentration at the n+ contact. For simplicity, we have replaced  $n_{bl}(d)$  by the average electron concentration  $N/d$ , which is a fairly good approximation. Space-charge effects

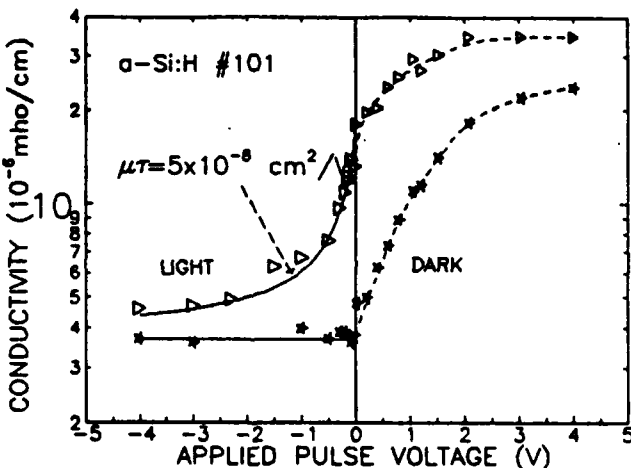


Figure 4. Dark and photo conductivity of a degraded a-Si:H sample vs. applied voltage pulse. Solid curve in the negative pulse range represents eq. (3) for  $\mu\tau = 5 \times 10^{-8} \text{ cm}^2/\text{V}$ .

are negligible in this polarity, even if all photo electrons are swept away from the sample (leaving behind the photogenerated holes). Hence the field is very nearly uniform at the value  $V/d$ . Solution of eq. (1), with the boundary condition that  $N$  assumes the zero-field density  $N_0 = L\tau$  at the onset of the pulse ( $t = 0$ ), yields

$$N = N_0/(1 + \mu\tau E/d) + N_0 \exp[-(1/\tau + \mu E/d)t]/(1 + d/\mu\tau E). \quad (2)$$

Now  $d/\mu E$  is the electron transit time through the film and is typically  $10^{-8}$  sec for an applied voltage of 1 V. The measurement is taken about 1  $\mu$ sec following the pulse onset, so that the second term in eq. (2) can be neglected to a very good approximation. Re-writing eq. (2) in terms of the photoconductivity  $\sigma = q\mu N/d$  we then have

$$\sigma = \sigma_0/(1 + \mu\tau V/d^2) \quad (3)$$

The solid curve fitted to the photoconductivity data at negative voltages in Fig. 4 is a plot of eq. (3) for  $\mu\tau = 5 \times 10^{-8}$  cm<sup>2</sup>/V. The fit with the experimental points is seen to be very good. The rather low value of  $\mu\tau$  is reasonable for the degraded sample used in the measurement. The method can be applied effectively even if  $\mu\tau$  is an order of magnitude lower. It should be noted that  $\mu$  in this context is the trap-controlled mobility [7,8].

#### ACKNOWLEDGMENTS.

The authors are indebted to Dr. A. Catalano for providing the a-Si:H samples. Special thanks are due to Prof. I. Balberg for many helpful discussions. This work was supported in part by the National Science Foundation EPSCoR grant EHR-9108775 and in part by the U.S. Army Research Office grant No. DAAL03-89-G-0114.

#### REFERENCES

1. See, for example, A. Madan and M.P. Shaw, *The Physics and Applications of Amorphous Semiconductors* (Academic, Boston, 1988) and *Amorphous Silicon Technology-1992*, Edited by M.J. Thompson, Y. Hamakawa, P.G. LeComber, A. Madan and E. Schiff, Mat. Res. Soc. Symp. Proc. 258 (1992).
2. S. Trokman, A. Many, Y. Goldstein, G. Heiland, D. Kohl and H. Moermann, J. Phys. Chem. Solids 42, 937 (1981).
3. M. Wolovelsky, J. Levy, Y. Goldstein, A. Many, S.Z. Weisz and O. Resto, Surf. Sci. 171, 442 (1986).
4. S.Z. Weisz, J. Penalbert, A. Many, S. Trokman and Y. Goldstein, J. Phys. Chem. Solids, 51, 1067 (1990).
5. A. Many, Y. Goldstein and N.B. Grover, *Semiconductor Surfaces* (North Holland, Amsterdam, 1970).
6. D. Goldie, P.G. LeComber and W.E. Spears, Mat. Res. Soc. Symp. Proc. 119, 489 (1988).
7. E.A. Schiff and M. Silver in *Amorphous Silicon and Related Materials*, H. Fritzsche, Ed. (World Scientific, Singapore, 1988), p. 825.
8. T. Tiedje and A. Rose, Solid State Commun. 37, 48 (1981).

## INHOMOGENEITY IN THE NETWORK ORDER OF DEVICE QUALITY a-Si:H

G. MORELL<sup>1</sup>, R.S. KATIYAR<sup>1</sup>, S.Z. WEISZ<sup>2</sup>, M. GOMEZ<sup>2</sup>, AND I. BALBERG<sup>2</sup>

<sup>1</sup>Physics Department, University of Puerto Rico, Rio Piedras, PR 00931

<sup>2</sup>Racah Institute of Physics, The Hebrew University, Jerusalem 91904, Israel

### ABSTRACT

In this paper we show that the degree of order of the Si network in a-Si:H is increasing with two length scales from the surface into the bulk. The major manifestation of the disorder is the variation in the Si-Si bond-stretching rather than the variation in the width of the dihedral angle distribution. The results are interpreted in terms of the decrease of the hydrogen concentration from the free surface into the bulk.

### INTRODUCTION

A considerable understanding of the lattice dynamics of covalent amorphous semiconductors in general, and of hydrogenated amorphous silicon in particular, has been gained<sup>1-3</sup> between the mid 70's and the mid 80's. This understanding is based on the identification of the phonon spectra in these materials as associated with a coupling parameter-weighted phonon density of states of the crystalline one phonon modes<sup>4-6</sup>. Following this development the Raman spectra of a-Si:H became a tool in evaluating the "order" of the amorphous silicon network. Both the tool and the "order" are simply defined by the similarity to the spectrum<sup>3</sup> of crystalline silicon, c-Si, while the amorphicity of the structure (i.e., the corresponding lack of a long range order or the presence of the corresponding amorphous radial distribution function<sup>7</sup>) is maintained. The most conspicuous feature of these Raman spectra is the phonon density band which originates from the transverse optical (TO) Si-Si stretching mode in the tetrahedral structure of c-Si. The closer the peak position of the corresponding band in the spectrum,  $\omega_{TO}$ , to that of the c-Si line at  $520 \text{ cm}^{-1}$ , and the narrower the peak width,  $\Delta_{TO}$ , the more "ordered" the material. The microscopic meanings of these features are that the Si-Si bond length is closer to that of c-Si, and that the width of the bond's dihedral angle distribution function,  $\Delta\theta$ , is narrower. In particular, models were presented<sup>5,8</sup> and predictions were given for an almost linear relationship between  $\Delta_{TO}$  and  $\Delta\theta$ . Once this model became well established, attempts were made to relate the degree of order to other physical properties<sup>9-12</sup>, and to evaluate the effects of various film deposition parameters on the degree of disorder. The purpose of the present study is to follow the type and degree of network order from the free surface of a deposited a-Si:H film toward its bulk.

Our approach in the present work is to study both, the effect of the laser excitation frequency and the effect of the film thickness on the Raman spectra. The need for such a simultaneous application of both approaches is that application of the first approach only, does not enable the association of the observations with other physical parameters (such as the optical band gap<sup>6</sup>) that were studied in conjunction with the Raman spectra. On the other hand, the results of the second approach do not necessarily represent inhomogeneity within the films. For example, it is known that for thick films there is hardly any thickness dependence of the Raman spectra<sup>13-15</sup>, does this mean that these films are uniform? Hence, mutually consistent results of the above two approaches may reveal whether the previously reported film thickness dependencies of the Raman spectra have to do with inhomogeneity in the network structure along the axis of growth, and indicate the reason for these dependencies. We also note in passing that while film thickness dependencies of the Raman spectra have been studied previously, we do not know of a simultaneous report of the thickness dependencies of the TA-TO peak intensities ratio,  $I_{TA}/I_{TO}$ , the peak width  $\Delta_{TO}$ , and the peak position  $\omega_{TO}$  of the TO mode. Consequently, no comprehensive picture regarding the film thickness dependence of the disorder has been derived thus far.

Following the above considerations it appears that only a comprehensive study of the various features, and the simultaneous approach adopted in the present study may provide maps for the inhomogeneity of the various degrees of network order in a-Si:H films. Following the derivation of the maps we will discuss the possible mechanisms that determine the spatial distribution of the disorder.

## EXPERIMENTAL DETAILS

The samples used in the present study were device quality a-Si:H films that were deposited by rf glow discharge decomposition of silane under standard conditions<sup>12,17,18</sup> (e.g., decomposition temperature  $T_s = 270^\circ\text{C}$  and growth rate of  $4\text{\AA/s}$ ). These conditions were kept the same for all the samples used, except the deposition time which was varied in order to yield films of different thicknesses. The substrates used were Corning 7059 glass slides. The most relevant characterization of the samples is their optical band gap. Consequently we show in Figure 1 the Tauc-band gap of the films (the first set was used for our Raman spectra study). These data were derived from the measured optical transmission and reflection of the films.

The Raman spectra were recorded using a Raman microprobe<sup>19</sup> (from Instruments S.A.) and the applied laser excitation sources were 514.5 nm radiation from a 6W model Innova 906 Ar<sup>+</sup> laser, and 620nm radiation from model CR-590 dye laser, both from Coherent, Inc. The measurements were carried out in back scattering geometry, using a 100X microscope objective. In order to avoid any heating (or degradation) of the sample, the laser power at the sample was kept below 6 mW and the incident beam has been slightly defocussed on the samples. The samples' condition was displayed on a video monitor interfaced to the microscope. The detector system was a water cooled 1024 channel diode array from Princeton Instruments. The raw data was smoothed using a fast Fourier filtering program (Peakfit V3.0) developed by AISN Software Inc.

## EXPERIMENTAL RESULTS

In Figure 2 we show typical Raman spectra taken by the application of the above described two laser excitations. It is seen that for this  $10\text{ }\mu\text{m}$  thick film there are significant differences between the two corresponding spectra that we attribute to the fact that in device quality a-Si:H the red light photons have an absorption depth of 500 nm while the green light photons have an absorption depth of 70 nm. In the set of samples studied here the band gap varies, as seen in Figure 1, but both excitations correspond to above-optical band gap-absorption, and the ratio between these two absorption depths does not vary significantly within this set. In Figure 2 the feature around  $150\text{ cm}^{-1}$ , which is known to be associated with the TA bond bending mode, splits, in contrast to many and in agreement with many previous reports. The most interesting observation is that the relative intensity of the two subpeaks is different for the two excitations. Since this mode is believed to involve Si triades<sup>6</sup> and Si-rings<sup>3</sup> this finding, which has not been reported

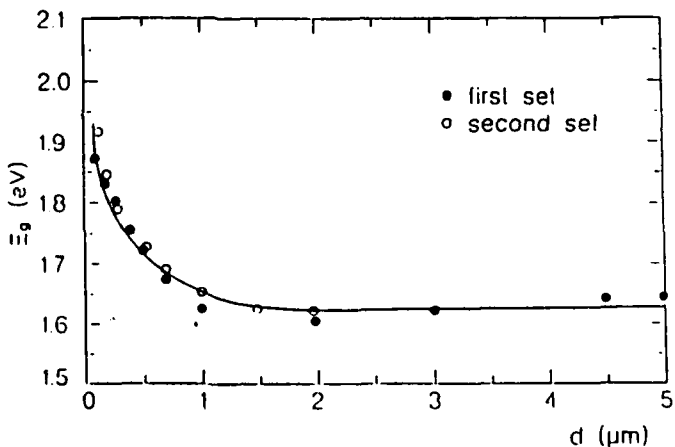


Figure 1. The Tauc-optical gap as a function of sample thickness used in the present Raman study (first set).

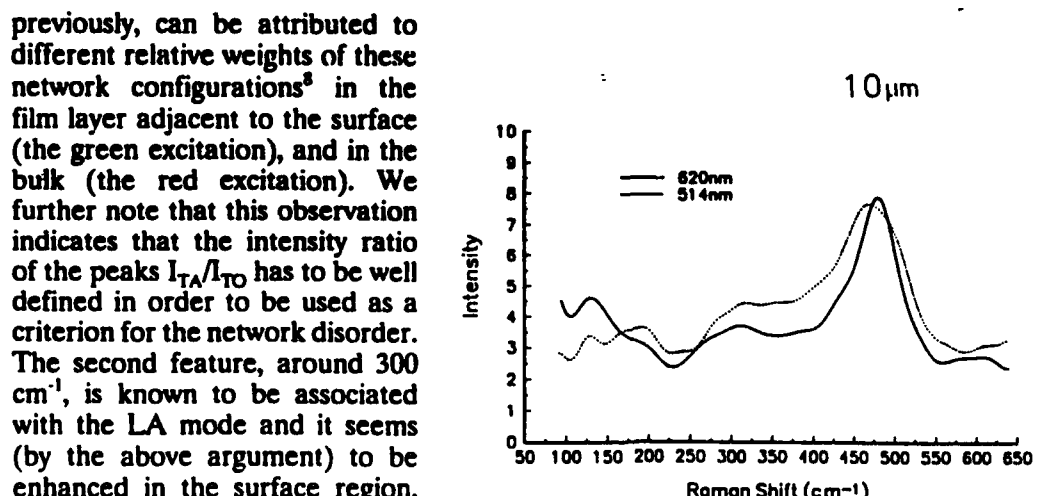


Figure 2. Typical Raman spectra of a-Si:H films under the excitation of two different laser frequencies.

The second feature, around  $300\text{ cm}^{-1}$ , is known to be associated with the LA mode and it seems (by the above argument) to be enhanced in the surface region. The third feature, around  $410\text{ cm}^{-1}$ , which is known to be associated with the LO mode, is responsible for the asymmetric broadening of the most conspicuous feature in the spectrum, the peak of the TO stretching mode, which is located around  $470\text{ cm}^{-1}$ . The strength of the LO mode in the film's layer adjacent to the surface (a larger amplitude for the green excitation) may be interpreted as due to a higher concentration of Si rings structures<sup>1,13</sup> on the surface and its vicinity. Such higher concentration of rings can be the result of the bond bridging that takes place on the surface.

Examining the TO peak position in both spectra shows a consistent behavior of both  $\omega_{\text{TO}}$  and  $\Delta_{\text{TO}}$ . The decrease of  $\omega_{\text{TO}}$  and the increase of  $\Delta_{\text{TO}}$  with respect to those of c-Si are larger for the green excitation. Considering the above-mentioned criteria for the short and intermediate range order of the Si network<sup>5-8</sup> we may conclude that the top 70 nm layer (the depth of the green light absorption) is less ordered than the bulk material. Note that this is also true for a  $10\text{ }\mu\text{m}$  sample for which a film thickness dependence study can be wrongly interpreted as indicating a homogeneous network order throughout the film.

The above conclusions are following the premise that the different behavior of the red and green excitations in Figure 2 cannot be attributed to a resonance Raman scattering. The basic argument for this premise is that the two excitations used here, are well removed from the resonance that occurs<sup>3</sup>, in a-Si:H, for photon energies larger than 3 eV. If there is any contribution of the "tail" of the resonance that affects our results it is clearly being offset by the penetration effect argued above. The evidence for that is the fact that our observation that  $\omega_{\text{TO}}$  decreases, the  $\Delta_{\text{TO}}$  increases, and the  $I_{\text{TA}}/I_{\text{TO}}$  increases with increasing laser frequency, while in the pure resonant case the reverse is true. Furthermore, while the switching in the TA subpeaks amplitudes can be easily attributed to the difference between a bulk and a surface response (see above) it cannot be attributed to a resonant effect. As we show below, the interpretation of the above data in terms of the film inhomogeneity is also consistent with the following findings regarding the thickness dependence of the features mentioned above.

Let us turn then to the thickness dependence of  $\omega_{\text{TO}}$ . As it is clearly shown in Figure 3,  $\omega_{\text{TO}}$  increases within the first couple of microns of film thickness, and then saturates for both excitations. This increase is relatively faster for the green excitation in comparison with that of the red excitation. We interpret these results as indicating that an "equilibrium" degree of network disorder for the corresponding property is established, both at the "free surface" vicinity and in the bulk, only for depths larger than a couple of microns. If we assume that a thin sample is similar in its properties to the top layer of a thick sample this finding is consistent with the findings of Figure 2. The range of variation of the network order is also consistent with the homogeneity scale associated with other

physical properties of these films, such as the optical band gap (Figure 1) and the phototransport properties<sup>18</sup>. For the derivation of the  $\Delta_{TO}$  value, so that the result is not affected by the contribution of the LO mode, we have considered in this study the value of twice the right hand side width of the TO peak as done in previous studies<sup>6,13,15</sup>. We find that  $\Delta_{TO}$  is quite insensitive to the sample thickness but, as clearly seen in Figure 4, it is larger for the green excitation than for the red excitation. We note in passing that the independence of  $\Delta_{TO}$  on  $d$  is reminiscent of the independence found<sup>15</sup> on  $T_s$  or on the band gap<sup>6</sup>, in a-Si:H films made by glow discharge decomposition of silane when the hydrogen content,  $C_H$ , is less than 20 at % (see below).

The main conclusion from the results shown here is then, that in device quality materials,  $\Delta\theta$  is a constant. Considering the theoretical predictions and the experimental values<sup>4,6</sup> we can conclude that the bulk  $\Delta\theta$  is as narrow as it can be (i.e., 9°), while at the vicinity of the surface  $\Delta\theta$  has not relaxed to the bulk optimized value. On the other hand the fact that the surface  $\Delta\theta$  is also independent of the history of the sample growth, indicates that there is a "surface optimized"  $\Delta\theta$  which is achieved in device quality a-Si:H.

Turning to the  $I_{TA}/I_{TO}$  ratio, which we denote here by  $A_{TA}/A_{TO}$  to indicate that the corresponding data is obtained by taking the ratio of the areas under the corresponding peaks, we get the results shown in Figure 5. Other evaluations of  $I_{TA}/I_{TO}$  ratios and their meaning will be discussed elsewhere. The overall decrease of the  $A_{TO}/A_{TA}$  ratio with thickness and the larger ratios for the green excitations are consistent with previous results, obtained on glass

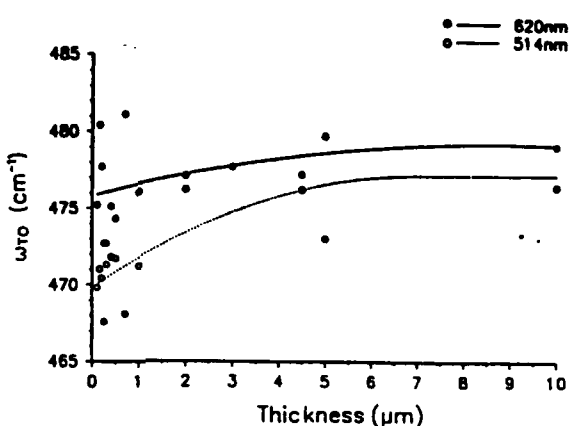


Figure 3. The thickness dependence of the TO peak position for the two applied laser excitations.

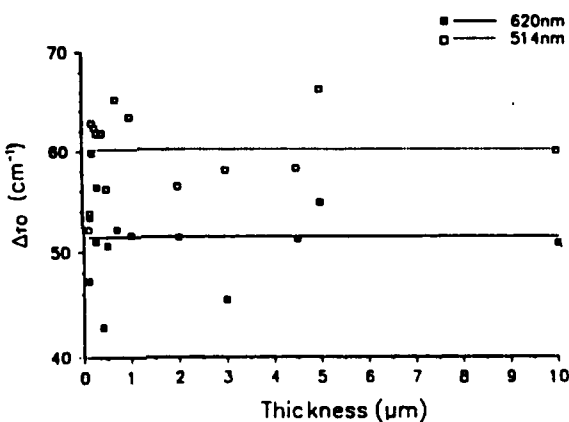


Figure 4. The thickness dependence of the TO peak width under the two applied laser excitations.

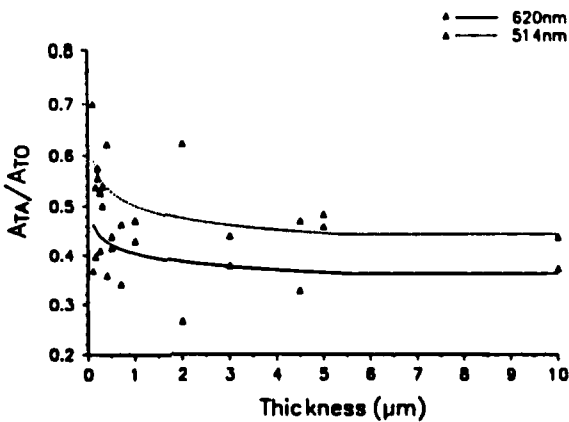


Figure 5. The ratio of the areas under the TA and the TO peaks, under the two applied laser excitations.

substrates<sup>16</sup>, and with the general decrease of network disorder from the surface into the bulk.

## DISCUSSION AND CONCLUSIONS

The data presented seems to indicate quite clearly that device quality a-Si:H is an inhomogeneous system in the order of the Si network along the film's growth axis. The inhomogeneity has two depth scales, one that is less than 70 nm and the other that has a tail of a couple of microns from the free surface into the bulk. These two length scales should be considered when analysis of a-Si:H devices is carried out. The most important conclusion of the present work is that the Raman spectra reported in the literature, which are normally taken using 514 nm wavelength excitation, reflect the degree of network order within the first length scale. Deeper in the bulk the amorphous network has a considerably larger degree of order.

Turning to the various features of disorder and their meaning let us start with the  $\Delta_{TO}$  thickness independence shown in Figure 4. The fact that  $\Delta_{TO}$  has been found to be independent of  $T_S$  for other films prepared by glow discharge<sup>15</sup>, such that the variation of  $E_g$  is the same<sup>4,6</sup> as in our films (see Figure 1), yields the conclusion that the dihedral angle distribution disorder is optimized under the preparation conditions of device quality a-Si:H. The fact that this is in sharp contrast with the dependence found in sputtered films<sup>4,6,10</sup> and the fact that  $\Delta_{TO}$  is of the order expected for the minimum possible  $\Delta\theta$  is indicating that no more improvement can be made in narrowing  $\Delta\theta$  by variation of deposition conditions. On the other hand the constant difference between  $\Delta_{TO}$  values for the two excitation frequencies used can be interpreted as due to the sharp difference between the close vicinity of the free surface (70 nm) and the bulk of a-Si:H. While not mentioned previously in the literature, this finding is not to surprising since the bond reconstruction near the surface, due to the termination of the tetrahedral network, is quite different from that of the bulk. The present results show then that the  $\Delta\theta$  width at the surface vicinity is also optimized, but, as to be expected the surface optimized value is larger than the bulk optimized value.

The results for the  $A_{TA}/A_{TO}$  thickness dependence, which are similar to those obtained by other researchers (for glass substrates<sup>14</sup>), reveal the variation of this ratio on a scale of a couple of microns, just as the  $E_g(d)$  variation shown in Figure 1. We find again a clear difference between the close vicinity of the surface and the bulk. Since the TA mode is associated with the presence of Si triads<sup>3</sup> this conclusion is consistent with the variation of the photoelectronic properties which depend on the concentration of dangling bonds. One can indeed show that there are two length scales involved in the latter concentration. The first is associated with the surface recombination velocity<sup>18</sup> and the other with a broader decrease of this concentration toward the interior of the bulk<sup>20</sup>. The agreement of the above observations with those found in the study of the Raman spectra as a function of  $T_S$  for materials of the same optical band gap<sup>16</sup> is an indication that it is the  $E_g$  dependence that should be used for comparisons of features in the Raman spectra. In particular, since the dihedral angle order is shown here to be optimized, it appears<sup>6</sup> that the prime reason for the variation of  $E_g(d)$  is due to the variation of  $C_{11}$ . It is also well known that  $C_{11}$  decreases from the surface into the bulk<sup>21</sup>. Correspondingly, there is the decrease of the  $A_{TA}/A_{TO}$  ratio with  $d$ , and, as discussed above, the corresponding decrease of the dangling bond concentration. This conclusion is also consistent with the  $\omega_{TO}$  dependence on  $d$  as given in Figure 3, since again, the results are consistent with the  $\omega_{TO}$  dependence on  $T_S$ . The explanation for the latter results was given by the model of the quasi interstitial hydrogen. This model, as proposed by Hishikawa et al<sup>16</sup>, suggests that the main role of the hydrogen atom is to act as an interstitial impurity in the silicon network, yielding repulsive forces between itself and the neighboring silicon atoms. Therefore the much larger hydrogen concentration at the surface and its gradual decrease into the bulk account well for the observation. A model based on network relaxation, on the other hand, cannot explain simultaneously the independence of  $\Delta_{TO}$  and the dependence of  $\omega_{TO}$  on  $d$ .

## ACKNOWLEDGEMENTS

The authors are indebted to A. Catalano and B.P. Nelson for the samples used in this study. This work was supported in part by EPSCoR-NSF grant EHR-9108775, in part by U.S. Army Research Office grant No. DAALO3-89-G-0114, and in part by the U.S.-Israel Binational Science Foundation.

## REFERENCES

1. M.H. Brodsky in Light Scattering in Solids, Vol. I, edited by M. Cardona (Springer Verlag, Berlin, 1975), p.205.
2. D. Beeman and R. Alben, *Adv. in Physics*, **26** 339 (1977).
3. D. Bermejo, M. Cardona and M.H. Brodsky, Proc. of the VII Intl. Conf on Amorphous and Liquid Semiconductors, edited by W. Spear (University of Edinburgh, Edinburgh, 1977), p. 343, D. Bermejo and M. Cardona, *J. Non Cryst. Solids* **32** 405 (1979).
4. D. Beeman, R. Tsu and M.F. Thorpe, *Phys. Rev. B* **32** 874 (1985).
5. R. Tsu, J.G. Hernandez and F.H. Pollak, *J. Non. Cryst. Solids* **66** 109 (1984).
6. N. Maley and J.S. Lannin, *Phys. Rev. B*, **36** 1146 (1987).
7. J.S. Lannin, *J. Non Cryst. Solids* **97 & 98**, 39, 203 (1987).
8. N. Maley, D. Beeman and J.S. Lannin, *Phys. Rev. B* **38** 10611 (1988).
9. F. Cerdeira, C.J. Buchenauer, F.H. Pollak and M. Cardona, *Phys. Rev. B* **5** 580 (1972).
10. B. Ranchoux, D. Jousse, J.C. Bruyere and A. Deneuville, *J. Non Cryst. Solids*, **53 & 60**, 185 (1983).
11. J. Hanna, H. Azuma, H. Shirai, M. Azumaard, and I. Shimizu, *J. Non. Cryst. Solids* **114** 804 (1989).
12. A.H. Mahan, J. Carapella, B.F. Nelson, R.S. Crandall and I. Balberg, *J. Appl. Phys.* **69** (1991).
13. S.T. Kshirsagar, N.J. Khaladkar, J.B. Mamdapurkar and A.P.B. Sinha, *Japanese J. Appl. Phys.* **25** 1788 (1986).
14. Y. Hishikawa, S. Tsuda, N. Nakamura, S. Nakano and Y. Kuwanto, *Appl. Phys. Lett.* **57** 771 (1990).
15. Y. Hishikawa, K. Wantabe, S. Tsuda, M. Ohnishi and Y. Kuwanto, *Japanese J. Appl. Phys.* **24** 385 (1985).
16. Y. Hishikawa, K. Wantabe, S. Tsuda, S. Nakano, M. Ohnishi and Y. Kuwanto, *J. Non Cryst. Solids* **97 & 98** 399 (1987).
17. Y.M. Li, B.F. Fieselmann and A. Catalano, Proc. of the XXII IEEE PVSC (IEEE, New York, 1991), p. 1231.
18. L. Yang, I. Balberg, A. Catalano and M. Bennett, *Mat. Res. Soc. Symp. Proc.* **192** 243 (1990).
19. F. Adar in Materials Characterization for Systems Performance and Reliability, edited by J.W. McCauley and V. Weiss (Plenum Publishing Corp., 1986) p. 339.
20. M. Favre, H. Curtins and A.V. Shah, *J. Non Cryst. Solids* **97 & 98** 731 (1987).
21. S. Hasegawa, S. Shimizu and Y. Kurata, *Phil. Mag. B* **49** 511, 521 (1984).

# T-matrix approach for calculating local fields around clusters of rotated spheroids

William Vargas, Luis Cruz, Luis F. Fonseca, and Manuel Gómez

A T-matrix formalism is used to calculate local electric fields around clusters of prolate spheroids in the long-wavelength regime. The calculations are performed as a function of interparticle distance as well as angle of orientation. The observed red shifts in the resonant wavelengths of the characteristic peaks are shown to obey an exponential relationship as a function of interparticle separation and a sinusoidal relationship as a function of angle of rotation of the spheroid. The behavior of the cluster is discussed and the two effects of separation and rotation are compared.

## 1. Introduction

Optical properties of systems of particles whose size is smaller than the wavelength of the incident electromagnetic radiation have been studied for a long time,<sup>1,2</sup> but the effect of the clustering of such particles is not yet well understood. Recent interest has developed in this subject because clustering is essential to the understanding of many physical processes of interest. Moreover, the current calculations of local scattered electric fields are directly applicable to fields such as surface-enhanced Raman scattering and light scattering and absorption from metallic colloids in alkali halide crystals.<sup>3-8</sup>

Clusters of spheres have been analyzed, primarily in the radiation zone<sup>9-12</sup> or with the use of an electrostatic approach.<sup>10,13</sup> The purpose of this study is to calculate the local electrodynamic field around clusters of two prolate spheroids in the long-wavelength regime as a function of the separation between them and of their relative orientations by using a T-matrix approach, which describes electromagnetic scattering for a general wave that is incident on objects of arbitrary shape. Although the formalism can be used to calculate important parameters in the radiative regime, such as scattering cross sections, the local fields are the major concern here.

The T-matrix method permits an electrodynamic

approach that considers vectorial multipolar fields, in contrast to other recent electrostatic approaches that consider scalar multipolar potentials.<sup>10</sup> The extension to two scatterers is achieved by using an effective T matrix for more than one scatterer, which retains all the advantages of the T matrix for the single scatterer and also permits calculations for scatterers made up of clusters of metallic particles of arbitrary shape. The rotation of the individual T matrices corresponding to any given particle is achieved by using a transformation of the spherical harmonics under finite rotations. This study extends previous research on the calculations of the scattered electric field in the vicinity of clusters of metallic scatterers.<sup>14</sup> In this vicinity two-particle clusters of various configurations gave enhancements of up to  $10^3$  and demonstrated the existence of a critical distance greater than the touching distance between the scatterers at which maximum enhancement was obtained.

We demonstrate that because of clustering interactions the calculated spectrum shows two peaks for the case of clusters of two small prolate spheroids aligned in the direction of the incident electric field, in contrast to the spectrum of the isolated small prolate spheroid that has only one peak. The principal peak decreases in intensity and shifts exponentially as a function of interparticle distance to the value of the resonance for the isolated spheroid, whereas the secondary peak has a vanishing intensity that decreases exponentially as a function of interparticle distance. A decoupling interparticle distance  $d$  of  $4b$ , where  $b$  is the semimajor axis of the prolate spheroids that make up the cluster, is observed. At that distance the behavior of the cluster near any one of the two constituent particles equals that of one

W. Vargas is with the Escuela de Física, Universidad de Costa Rica, San José, Costa Rica. The other authors are with the Department of Physics, University of Puerto Rico, Rio Piedras, Puerto Rico 00931.

Received 13 August 1991.  
0003-6935/93/122164-07\$05.00/0.  
© 1993 Optical Society of America.

isolated spheroid. It is shown that there is also a shift in wavelength to the red as a result of the rotation of the spheroids and that this shift varies sinusoidally as a function of orientation.

For all the calculations herein, silver was taken as a model metal by using the complex frequency-dependent dielectric function reported in the literature for the bulk material,<sup>15</sup> although the method is applicable to any material for which the complex dielectric constant is known. For the range of sizes used in these calculations, an electronic mean free path reduced by the boundary of the scatterer or quantum size effects could introduce some modifications to the data for silver used here.

Section 2 presents the T-matrix formalism developed for isolated particles and its modification for metallic clusters. The calculations are done as expansions in vector spherical harmonics  $\Psi_n$ , whose number  $n$  corresponds to terms in the multipolar expansion of the electromagnetic field. Because our main objective is to study clusters, spherical harmonics are used as a convenient basis. A rotation of the T matrix corresponding to a single scatter is performed, permitting consideration of geometries where the spheroids in the cluster have arbitrary relative orientations.

Section 3 presents the calculation of the local electric fields for these clusters. The clusters are analyzed as a function of separation between spheroids and as a function of angle of orientation with respect to the incident wave. The rate of change of the wavelength shift as a function of interparticle distance and angle of orientation is then discussed. In Section 4 conclusions are presented.

## 2. Formalism

### A. Single Scatterers

The T-matrix formalism developed by Waterman<sup>16</sup> takes into account multipolar contributions, which are essential for any valid calculation of local fields of single nonspherical particles as well as for all clusters even when they are in the long-wavelength regime. The formalism also takes into account phase-retardation effects caused by the size of the scatterers, which are important for particles and clusters whose sizes are comparable with the wavelength of the incident field.

In this method the scattered, internal, and incident fields are expanded in terms of the corresponding elementary fields that are a basis set of solutions for the vector Helmholtz equation,

$$\nabla \times \nabla \times \Psi - k^2 \Psi = 0. \quad (1)$$

The incident  $\epsilon_0$  and internal  $\epsilon_i$  fields are expanded in terms of the basis that is regular at the origin  $\text{Re } \Psi$  and the scattered  $\epsilon_s$  field in terms of the nonregular  $\Psi$

one,

$$\begin{aligned} \epsilon_0 &= \sum_n A_n \text{Re } \Psi_n, \\ \epsilon_i &= \sum_n D_n \text{Re } \Psi_n, \quad |\mathbf{r}| < r_{\min}, \\ \epsilon_s &= \sum_n F_n \Psi_n, \quad |\mathbf{r}| > r_{\max}, \end{aligned} \quad (2)$$

where  $A_n$  are known coefficients,  $D_n$  and  $F_n$  are unknown,  $r_{\min}$  is the radius of the maximum sphere inscribed in the scatterer, and  $r_{\max}$  is the minimum sphere inscribing the scatterer.

The elementary wave functions are expressed as

$$\Psi_{\sigma mn}(\mathbf{r}) = \gamma_{mn}^{1/2}(k^{-1}\nabla \times)^{\tau} [k \mathbf{r} Y_{\sigma mn}(\theta) h_n(kr)], \quad (3)$$

where  $\tau = 1, 2$ ,  $\sigma = \text{even}(e)$  or  $\text{odd}(o)$ ,  $n = 1, 2, \dots$ ,  $m = 0, 1, \dots, n$ ,

$$\gamma_{mn} = \epsilon_m \frac{(2n+1)(n-m)!}{4n(n+1)(n+m)!},$$

$$Y_{\sigma mn}(\theta) = \cos(m\phi) P_n^m(\cos \theta),$$

$$Y_{\sigma mn}(\theta) = \sin(m\phi) P_n^m(\cos \theta).$$

The index  $\tau = 1, 2$  describes the type of excitation, magnetic or electric;  $\epsilon_m$  is the Neumann symbol defined as  $\epsilon_0 = 1$  and  $\epsilon_m = 2$  otherwise;  $n$  is the order of the multipole; and  $\sigma$  gives the parity of the elementary functions. The regular form of the basis functions are obtained by substituting the Hankel functions with the Bessel functions.

The surface currents on the scatterers are used to express the expansion coefficients of the internal field with those of the scattered and incident fields, respectively, by the following relationships:

$$\mathbf{F} = -i \text{Re}(\mathbf{Q}') \mathbf{G}, \quad (4)$$

$$\mathbf{A} = i \mathbf{Q}' \mathbf{G}, \quad (5)$$

where  $\mathbf{G}$  represents the vector of the expansion coefficients of the internal field and  $\mathbf{Q}'$  represents the transpose of the  $\mathbf{Q}$  matrix. For a particle with a complex dielectric function,  $\mathbf{Q}$  is given by

$$\begin{aligned} \mathbf{Q}_{mn} = \frac{k_0}{\pi} \int_s d\mathbf{s} & [(\nabla \times \text{Re } \Psi_n(kr)) \times \Psi_n(k_0 r) \\ & + \text{Re } \Psi_n(kr) \times (\nabla \times \Psi_n(k_0 r))], \end{aligned} \quad (6)$$

where  $k_0^2 = \epsilon_{\text{ext}} \omega^2 / c^2$  and  $k^2 = \epsilon_{\text{int}} \omega^2 / c^2$ ,  $s$  is the surface of the scatterer, and  $\Psi_n(kr)$  is substituted by  $\text{Re } \Psi_n(kr)$  wherever  $\text{Re } Q$  appears. In our case  $\epsilon_{\text{ext}} = 1$  (vacuum) and  $\epsilon_{\text{int}}$  is the corresponding value for silver.

Equation (5) permits the calculation of the internal field, at least when  $|\mathbf{r}| < r_{\min}$ . Eliminating  $\mathbf{G}$  from Eqs. (4) and (5), we obtain a relation between the coefficients of the scattered and incident fields:

$$\mathbf{F} = \mathbf{T} \mathbf{A}, \quad (7)$$

where  $\underline{T}$  is the T matrix of the single scatterer defined as

$$\underline{T} = -\underline{Q}^{-1} \operatorname{Re} \underline{Q}. \quad (8)$$

With Eq. (2) the local fields can be calculated for  $|\mathbf{r}| < r_{\min}$  by using the Q matrix and for  $|\mathbf{r}| > r_{\max}$  by using the T matrix, but the region  $r_{\max} > |\mathbf{r}| > r_{\min}$  is forbidden because the convergence of the expansions of Eq. (2) is not ensured. Some research has been done to improve on this shortcoming; Bringi and Seliga<sup>17</sup> proposed a mathematical procedure that used the T-matrix framework to calculate fields inside this forbidden zone. Barber *et al.*<sup>18</sup> used a method based on the T-matrix approach to evaluate local fields not only at the tips but at any place on the surface of the spheroids.

### b. Rotation of the T Matrix

For the rotation of the T matrix, two coinciding coordinate systems are considered. With respect to the origin of both systems, the Euler angles  $\alpha$ ,  $\beta$ , and  $\gamma$  are used to rotate one of the systems relative to the other.<sup>19</sup> The rotation of the basis functions is accomplished by transforming the spherical harmonics under finite rotations. These transformation properties are given in the quantum mechanics literature (e.g., Ref. 20).

Explicitly, if  $\Psi_{mn\alpha}$  and  $\Psi_{mn'\alpha'}$  are the vector spherical functions in the rotated and nonrotated coordinate systems, respectively, then one can write

$$\Psi_{mn\alpha} = \sum_{m' n'} D_{m' n' m\alpha}(\alpha, \beta, \gamma) \Psi_{mn'\alpha'},$$

where the index  $n$  is invariant under rotations and the rotation matrix D is a function of the Euler angles that define the relative orientation of the two coordinate system.<sup>20</sup>

The incident and scattered electric fields in Eq. (2) are then expanded with respect to the two coordinate systems. A relationship between the expansion coefficients for  $\epsilon_0$  and  $\epsilon_s$  in the two systems can be established by using the orthogonality of the vector spherical functions. Using the definition of the T matrix, we finally obtain

$$\underline{T}' = \underline{D}^{-1}(\alpha, \beta, \gamma) \underline{T} \underline{D}(\alpha, \beta, \gamma), \quad (9)$$

where  $\underline{T}'$  is the T matrix for the rotated coordinate system.

### C. Clusters

The T-matrix formalism has been extended to systems with more than one scatterer by Peterson and Ström<sup>9</sup> by using the translation theorems for the vector spherical functions.<sup>21</sup> The translation properties of  $\Psi_n$  and  $\operatorname{Re} \Psi_n$  are summarized by Ref. 22:

$$\operatorname{Re} \Psi_m(\mathbf{r} + \mathbf{a}) = \sum_{n'n} R_{m'n'n}(\mathbf{a}) \operatorname{Re} \Psi_{n'n}(\mathbf{r}),$$

$$\Psi_m(\mathbf{r} + \mathbf{a}) = \sum_{n'n} \sigma_{m'n'n}(\mathbf{a}) \operatorname{Re} \Psi_{n'n}(\mathbf{r}), \quad |\mathbf{a}| > |\mathbf{r}|,$$

$$\Psi_m(\mathbf{r} + \mathbf{a}) = \sum_{n'n} R_{m'n'n}(\mathbf{a}) \Psi_{n'n}(\mathbf{r}), \quad |\mathbf{a}| < |\mathbf{r}|,$$

where  $\sigma_{m'n'n}$  and  $R_{m'n'n}$  are the elements of the translation matrices as defined in Ref. 9.

Peterson and Ström obtained a T matrix for the cluster of two particles in terms of the T matrices of each single scatterer,

$$\begin{aligned} \underline{T}(1, 2) = & \underline{R}(\mathbf{a}_1) [\underline{T}(1) [\underline{1} - \underline{\sigma}(-\mathbf{a}_1 + \mathbf{a}_2) \\ & \times \underline{T}(2) \underline{\sigma}(-\mathbf{a}_2 + \mathbf{a}_1) \underline{T}(1)]^{-1} \\ & \times [\underline{1} + \underline{\sigma}(-\mathbf{a}_1 + \mathbf{a}_2) \underline{T}(2) \underline{R}(\mathbf{a}_1 - \mathbf{a}_2)]] \\ & \times \underline{R}(-\mathbf{a}_1) + \underline{R}(\mathbf{a}_2) [\underline{T}(2) [\underline{1} - \underline{\sigma}(-\mathbf{a}_2 + \mathbf{a}_1) \\ & \times \underline{T}(1) \underline{\sigma}(-\mathbf{a}_1 + \mathbf{a}_2) \underline{T}(2)]^{-1} [\underline{1} + \underline{\sigma}(-\mathbf{a}_2 + \mathbf{a}_1) \\ & \times \underline{T}(1) \underline{R}(\mathbf{a}_2 - \mathbf{a}_1)]] \underline{R}(-\mathbf{a}_2), \end{aligned} \quad (10)$$

where  $\mathbf{a}_1$  and  $\mathbf{a}_2$  are the distances from the origin to the center of scatterers 1 and 2, respectively.

The scattered field can be expressed in terms of the incident field by using the T-matrix with the following relationship:

$$\epsilon_s = \underline{T} \epsilon_0.$$

Most of the results presented herein will be expressed in terms of the total electric field given by

$$\epsilon_t = \epsilon_s + \epsilon_0. \quad (11)$$

It is important to remember that the local fields can only be calculated by starting from a minimum circumscribing sphere around the scatterers to ensure convergence of the spherical wave expansions.

With these two transformations, rotation and translation, it is then possible to consider clusters with variables separation and arbitrary orientation of the constituent metallic spheroids.

### 3. Discussion

The quantities discussed here are the normalized local field intensities  $|\epsilon_s/\epsilon_0|^2$  in the neighborhood of the clusters of two prolate spheroids. These have been calculated by inserting the individual T matrices of each spheroid, Eq. (8), into Eq. (10), thus yielding the effective T matrix for the cluster as a function of interparticle distance. In the case of a different orientation between the spheroids, their rotation has been taken into account by applying Eq. (9) and substituting the rotated T matrix into Eq. (10). Finally, the total electric field vector has been calculated from Eq. (11), from which the enhancement of the intensity of the field was obtained by taking the square of the magnitude of that vector.

To illustrate the general results from this type of calculation, we use two identical prolate spheroids with an aspect ratio  $a/b = 0.9$  and  $a = 5$  nm, where  $a$  and  $b$  are the semiminor and semimajor axes of the prolate spheroid, respectively. The formalism permits the treatment of spheroids of any eccentricity, but because of computational time and memory limitations only the described size is considered. Although the clusters of spheroids used here are in the long-wavelength regime, the calculations are elec-

trodynamic in nature because the formalism is developed from the vector Helmholtz Eq. (1); results can and have been obtained for other sizes and aspect ratios.<sup>14</sup>

The calculations were done by taking the direction of propagation of the incident wave front to be along the  $y$  axis. The polarization of the electric field is parallel to the direction of the interparticle distance, which is the  $x$  axis. By testing other directions of incidence and polarizations, we have determined that the latter orientation gives the highest scattered-intensity enhancement (of the order of  $10^3$ ) for the configuration of the clusters considered; we therefore choose these as our working parameters. The calculations of the electric field are performed as a function of interparticle separation and relative orientation of the spheroids.

Two resonant peaks are exhibited by the spectra of all the geometrical configurations considered. It is worth noting that this behavior is due to the interparticle multipolar interactions, because only one peak is observed when the spheroids are sufficiently far apart (when  $d$ , the interparticle distance, is of the order of  $4b$ ).

The two resonant peaks experience a characteristic red shift as a function of decreasing distance between spheroids for all the clusters considered. This shift reflects the interaction among the spheroids in the cluster, which becomes stronger as the distance between the centers of the particles decreases, thereby resulting in maximum shift for touching spheroids. Figure 1 shows the calculated spectrum for the cluster of two spheroids whose semimajor axes are aligned with the incident electric field. Because this is the more elongated cluster, it exhibits the highest enhancement shown in this paper (of the order of  $10^3$ ). The closer the spheroids the higher the interac-

tion between them and the more multipolar terms are required in the calculation. As the interparticle distance decreases, the low-energy peak shifts more rapidly toward the red than the high-energy peak. This behavior is related to higher multipolar terms, other than the dipolar, which become more important as the spheroidal constituents of the cluster approach each other. As the interparticle distance diminishes, the low-energy peak decreases rapidly in energy while its intensity increases. The high-energy peak disappears when  $d = 3b$ , the decoupling distance, whereas the low-energy peak shifts to the resonant wavelength corresponding to the isolated particle.

The effect of rotation has been analyzed by rotating only one spheroid and by examining the local field at opposite points on the exclusion sphere on the axis that joins the centers of the particles, because for this case the cluster is asymmetric. The analysis is also performed by rotating both spheroids, thus maintaining the mirror symmetry of the cluster. In both cases the interparticle distance is held constant. Figures 2(a) and 2(b) show the behavior of the local field observed at the two previously indicated points on the  $x$  axis when only one spheroid is rotated. Figure 2(a) describes the field near the nonrotated spheroid and Fig. 2(b) describes that near the rotated spheroid. The difference between the two observation points is in the intensity of the local field, whereas the position of the resonance peaks remains constant. This constance is to be expected because the resonant peaks are phenomena associated with surface plasmons of the cluster that depend on the configuration of the whole cluster and not on the point of observation. Figure 3 shows the spectrum of the simultaneously rotated spheroids. The configuration  $\theta = 90^\circ$  coincides with the cluster of Fig. 1, which exhibits the highest enhancement in this paper. The rotation of the spheroids does not affect the number of peaks observed in the spectrum, although their energies are shifted toward the red as a function of increasing angle measured with respect to the  $y$  axis. For this case the red shift of the peaks is also attributed to the increase in interaction between the spheroids, because for an isolated spheroid the shift in energy as a function of angle of rotation is negligible for slightly eccentric spheroids. The maximum enhancement is obtained in Figs. 2(a) and 2(b) when the rotated spheroid is at an angle of  $\theta = 90^\circ$ . This occurrence is reasonable because the semimajor axis of the rotated spheroid is perpendicular to the polarization of the incident electric field at  $\theta = 0^\circ$  and is parallel at  $\theta = 90^\circ$ , thereby enhancing the field by its geometry and directing the energy more efficiently toward the other radiating spheroid. As we expected, the largest red shift and enhancement occurs in Fig. 3 where both spheroids are simultaneously rotated.

The resonant wavelengths for the cases shown in Figs. 1 and 3 have been studied as functions of interparticle distance  $d$  and orientation  $\theta$ , respectively. Figures 4(a) and 4(b) display the behavior of the

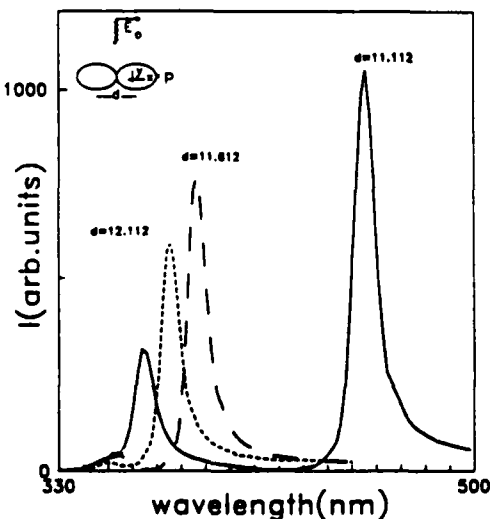


Fig. 1. Intensity of the total electric field at the point of observation  $P$  as a function of wavelength for a cluster of aligned spheroids with  $a/b = 0.9$  and  $a = 5$  nm for three interparticle distances ( $d = 11.112$  nm =  $2b$ , touching spheroids,  $11.612$  nm, and  $12.112$  nm). The direction of the incident radiation is along the  $y$  axis and the polarization is parallel to the  $x$  axis.

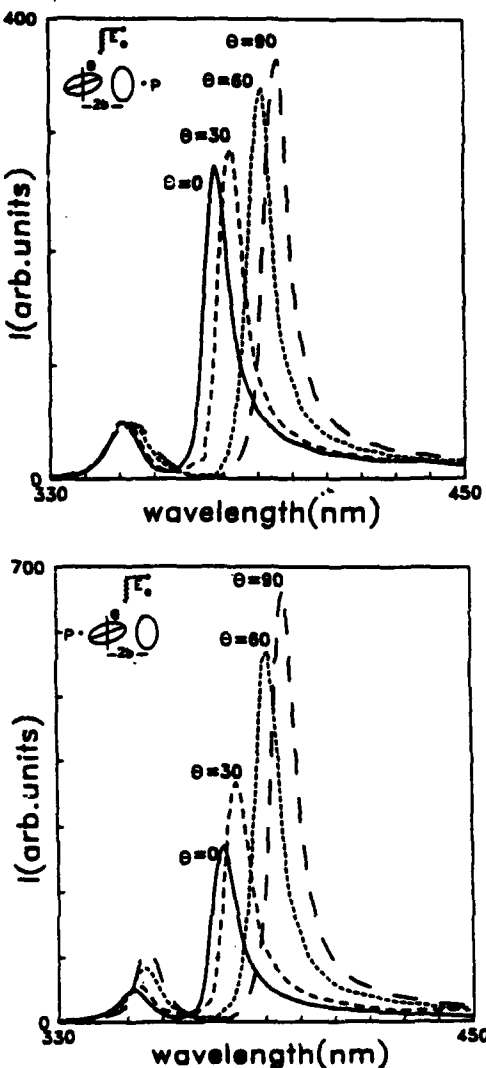


Fig. 2. (a), (b) Intensity of the total electric field at the point P as a function of wavelength for a cluster of spheroids with  $a/b = 0.9$  and  $a = 5$  nm for different angles of orientation of the spheroids with respect to the vertical axis. The directions of the incident radiation and the polarization are as shown.

low-energy peaks as a function of orientation angle and of interparticle separation. Figures 5(a) and 5(b) provide this same analysis for the high-energy peak. A least-squares fit to the data was made for all four cases to determine the behavior of the red shifts as a function of interparticle separation and also as a function of orientation. The spread of calculated resonance wavelengths about the smooth curves is due to the fact that all resonant wavelengths analyzed in Figs. 4 and 5 were obtained from a spline interpolation of the calculated cluster spectra. The uncertainty introduced by this interpolation in determining the resonant wavelengths is of the order of  $\pm 2$  nm.

In the case of both the low- and high-energy peaks for the rotated spheroids, the shift toward the red shows a sinusoidal behavior, as is illustrated in Figs. 4(a) and 5(a). A least-squares fit of this data gives a functional behavior for the shift that is governed by

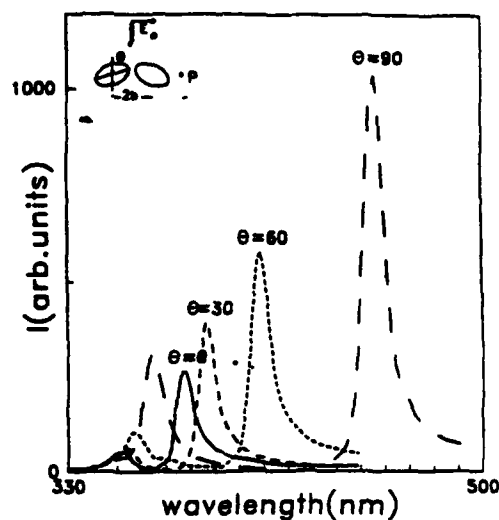


Fig. 3. Intensity of the total electric field at the point P as a function of wavelength for a cluster of simultaneously rotated spheroids with  $a/b = 0.9$ ,  $a = 5$  nm for different angles of rotation of the two spheroids. The directions of the incident radiation and the polarization are as shown.

the simple relationship  $\lambda(\theta) = A + B \sin^2(\theta)$ . For Fig. 4(a),  $A = 376.7$  nm and  $B = 47.8$  nm; for Fig. 5(a),  $A = 351.8$  nm and  $B = 7.2$  nm.

From Figs. 4(b) and 5(b), it appears that the position of the peaks have an exponential behavior as a function of increasing interparticle distance. A curve fitting gives the functional relationship  $\lambda(d) = \lambda' + \delta\lambda \exp[-(d - d_0)/\eta]$ . For the case of the low-energy peak,  $\lambda'$  was taken to be the resonant wavelength for the decoupled cluster, i.e., the resonant frequency of an isolated spheroid. Here  $\delta\lambda$  is the difference between the resonant wavelength of the touching spheroids and the resonant wavelength with no coupling and  $d_0$  is the touching distance  $2b$ . The

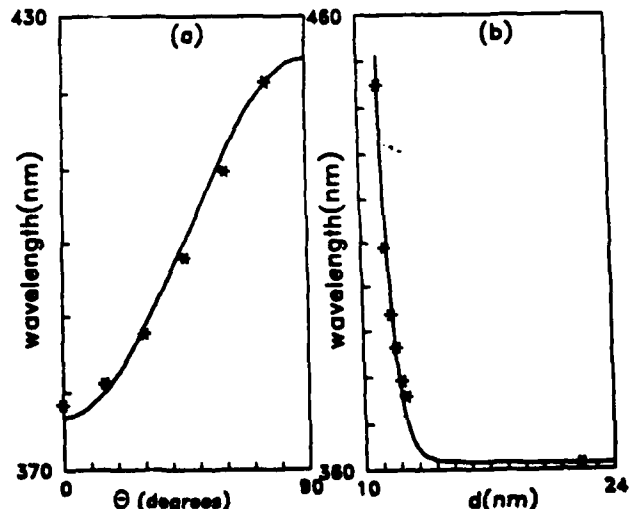


Fig. 4. Shift in the resonant wavelength for the low-energy peak as a function of (a) the rotation angle  $\theta$  of the simultaneously rotated spheroids, and (b) interparticle separation  $d$  for the aligned spheroids. The solid curve represents a least-squares fit to the calculated points.

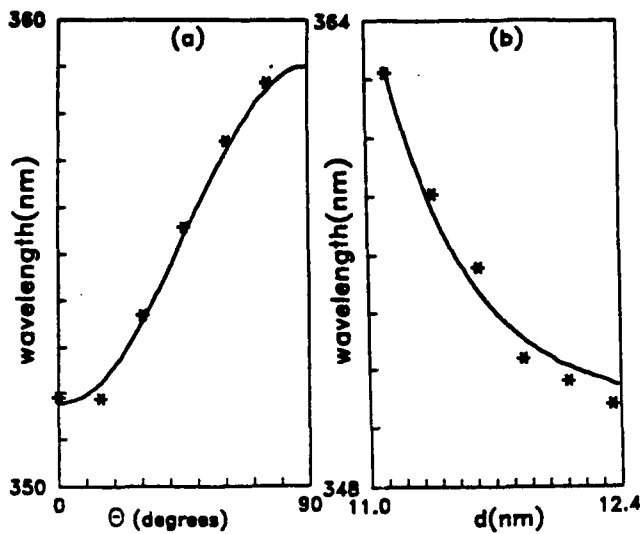


Fig. 5. Shift in the resonant wavelength for the high-energy peak as a function of (a) the rotation angle  $\theta$  of the simultaneously rotated spheroids, and (b) interparticle separation  $d$  for the aligned spheroids. The solid curve represents a least squares fit to the calculated points.

only fitting parameter used is  $\eta$ , which corresponds to a decay factor. For Fig. 4(b),  $\lambda' = 361.5$  nm,  $\delta\lambda = 94$  nm, and the fitted parameter is  $\eta = 0.57$  nm. For the case of the high-energy peak it is also necessary to fit  $\lambda'$ ; the resulting fitted curve for Fig. 5(b) yields  $\lambda' = 350$  nm,  $\delta\lambda = 13.6$  nm, and  $\eta = 0.32$  nm. From the analysis it is evident that the low-energy peak suffers a considerably larger shift in wavelength than the high-energy peak as a function of both angle and interparticle distance.

The decoupling distance for the cases discussed here occur at  $d \approx 3b$ . For all other cases studied by us the decoupling distance has been found to be  $d = 4b$ , which is twice the distance of touching spheroids.

#### 4. Conclusions

A T-matrix formalism has been used to calculate the local electric field near clusters of metallic spheroids, and the influence of clustering on their spectrum has been investigated as a function of interparticle distance  $d$  and relative orientation  $\theta$  in the long-wavelength regime. The calculations show two resonant peaks in the spectrum caused by interparticle interactions, which is in contrast with one peak in the spectrum of the single spheroid. The high-energy peak disappears and the low-energy peak becomes the peak of the isolated spheroid for interparticle distances of  $4b$ . This fact should prove useful in the analysis of clusters of more than two ellipsoidal particles.

As a result of the interaction among the spheroids that form the cluster, enhancements of up to  $10^3$  are observed. Higher enhancements should be observed for more eccentric ellipsoidal constituents of the cluster. The enhancement is shown to be sensitive to the relative orientation of the spheroids and the interparticle distance. Both resonant peaks are red shifted as a function of reduced interparticle distance

and of increasing angle of rotation with respect to the  $y$  axis.

The position of the higher-energy peak is less sensitive to interparticle distance than the lower-energy one, and rotations are less effective in shifting the peaks than the separation of the spheroids. Through a least-squares fit, we demonstrated that the shifting of the low-energy peak obeys an exponential relationship as a function of the varying interparticle distance that decays to the value of an isolated spheroid for values of  $d \approx 3b$ , whereas the red shift obeys a sinusoidal relationship as a function of the angle of rotation of the spheroids.

For experimental systems composed of a collection of scatterers with a random distribution of interparticle distances and orientations, these calculations will be important in predicting the estimated effective width of the observed resonances. The predicted width is expected to be greater than the ones shown here because such a system will have contributions from clusters with a wide variety of interparticle distances and relative orientations. A rough estimate suggests that the resonant peak of that system should have a width of the same order as the difference between the resonant energy of the cluster of touching spheroids and the resonant energy of a decoupled cluster.

Recently some efforts have appeared in the literature that treat clusters of spheroids by using ellipsoidal harmonics,<sup>23</sup> but to our knowledge only calculations restricted to the far zone have been performed. We do not expect that the use of ellipsoidal harmonics will simplify in any significant manner the calculation of the field in the near zone, because a cluster does not have either spherical or ellipsoidal symmetry; therefore, we do not anticipate any advantage of one expansion over the other.

This research was partially supported by the National Science Foundation grant INT-8509185 and by the U. S. Army Research Office grant DAAL03-89-G-0114.

#### References

1. Lord Rayleigh, "The incidence of light upon a transparent sphere of dimensions comparable with the wave-length," Proc. R. Soc. London Ser. A 84, 25-46 (1910).
2. G. Mie, "Beiträge zur optik trüber medien, speziell kolloidaler metallösungen," Ann. Phys. (Leipzig) 25, 377-445 (1908).
3. R. P. Devatty and A. J. Sievers, "Single-particle collective-mode coupling and the Mie resonance in small metallic particles: optical properties of colloidal Na in NaCl," Phys. Rev. B 24, 1079-1082 (1981).
4. J. M. Calleja and F. Agullo-Lopez, "Photoconductivity of potassium colloids in KCl single crystals," J. Phys. Chem. Solids 37, 363-367 (1976).
5. E. Rzepka, L. Taurel, and S. Lefrant, "First-order Raman scattering induced by Na and Ag colloids in NaCl, NaBr and NaI," Surf. Sci. 106, 345-349 (1981).
6. M. Moskovits, "Surface-enhanced spectroscopy," Rev. Mod. Phys. 57, 783-826 (1985).
7. H. Reimer and F. Fischer, "SERS from Ag colloids in alkali halide crystals," Phys. Status Solidi B 124, 61-67 (1984).

8. W. Kleeman, "Absorption of colloidal silver in KCl," *Z. Phys.* **215**, 113-120 (1968).
9. B. Peterson and S. Ström, "T-matrix for electromagnetic scattering from an arbitrary number of scatters and representations of  $E(3)$ ," *Phys. Rev. D* **8**, 3661-3678 (1973).
10. F. Claro, "Theory of resonant modes in particulate matter," *Phys. Rev. B* **30**, 4989-4999 (1984).
11. R. Fuchs and F. Claro, "Multipolar response of small metallic spheres: nonlocal theory," *Phys. Rev. B* **35**, 3722-3727 (1987).
12. Z. Chen, P. Sheng, D. A. Weitz, H. M. Lindsay, M. Y. Lin, and P. Meakin, "Optical properties of aggregate clusters," *Phys. Rev. B* **37**, 5232-5235 (1988).
13. N. Liver, A. Nitzan, and J. I. Gersten, "Local fields in cavity sites of rough dielectric surfaces," *Chem. Phys. Lett.* **111**, 449-453 (1984); N. Liver, A. Nitzan, and K. F. Freed, "Radiative and nonradiative decay rates of molecules absorbed on clusters of small dielectric particles," *J. Chem. Phys.* **82**, 3831-3840 (1985).
14. L. Cruz, L. Fonseca, and M. Gomez, "T-matrix approach for the calculation of local fields in the neighborhood of small clusters in the electrodynamic regime," *Phys. Rev. B* **40**, 7491-7500 (1989).
15. P. B. Johnson and R. W. Christy, "Optical constants of noble metals," *Phys. Rev. B* **6**, 4370-4379 (1972).
16. P. C. Waterman, "Symmetry, unitarity, and geometry in electromagnetic scattering," *Phys. Rev. D* **3**, 835-839 (1971).
17. V. N. Bringi and T. A. Seliga, "Surface currents and 'near' zone fields," in *Acoustic, Electromagnetic and Elastic Wave Scattering—Focus on the T-Matrix Approach*, V. K. Varadan and V. V. Varadan, eds. (Pergamon, New York, 1979), pp. 79-90.
18. P. W. Barber, R. K. Chang, and H. Massoudi, "Electrodynamic calculations of the surface-enhanced electric intensities on large Ag spheroids," *Phys. Rev. B* **27**, 7251-7260 (1983).
19. G. Arfken, *Mathematical Methods for Physicists* (Academic, New York, 1985), p. 198.
20. A. R. Edmonds, *Angular Momentum in Quantum Mechanics* (Princeton U. Press, Princeton, N.J., 1957).
21. O. R. Cruzan, "Translational addition theorems for spherical vector wave functions," *Q. Appl. Math.* **20**, 33-40 (1962).
22. V. K. Varadan, "Elastic wave scattering," in *Acoustic, Electromagnetic and Elastic Wave Scattering—Focus on the T-Matrix Approach*, V. K. Varadan and V. V. Varadan, eds. (Pergamon, New York, 1979), pp. 33-59.
23. M. F. R. Cooray and I. R. Ceric, "Electromagnetic wave scattering by a system of two spheroids of arbitrary orientation," *IEEE Trans. on Antennas and Propag.* **37**, 608-618 (1989).

# The dependencies of the two carriers mobility-lifetime products on the position of the Fermi level in a-Si:H

Y. Lubianiker<sup>a</sup>, I. Balberg<sup>a</sup>, S.Z. Weisz<sup>b</sup> and M. Gomez<sup>b</sup>

<sup>a</sup>The Racah Institute of Physics, The Hebrew University, Jerusalem 91904, Israel

<sup>b</sup>Department of Physics, University of Puerto Rico, Rio Piedras 00931, P.R.

In this presentation we report results obtained by the first combined application of the Metal Oxide Semiconductor and the Photocarrier Grating configurations. This combination enabled the first simultaneous study of the two carriers mobility-lifetime products and their light intensity exponents as a function of the position of the Fermi level, in undoped a-Si:H. We found that anticorrelations and correlations prevail between these two sets of quantities. The conclusion we derive from these behaviors is that the "defect pool" model accounts for the phototransport data much better than any other model.

## 1. INTRODUCTION

One of the methods [1,2] used to determine the energetic location of the defect states in hydrogenated amorphous silicon, a-Si:H, is finding the dependence of measurable phototransport properties on the energy separation between the conduction band edge in the bulk,  $E_c$ , and the equilibrium (or "dark") Fermi level,  $E_F$ . Predictions for the dependencies of the two carriers mobility-lifetime,  $\mu\tau$ , products on  $\Delta E = E_c - E_F$  have been given recently by various researchers for both, the "standard" [3,4] and the "defect pool" [4], models of a-Si:H. While the models proposed were for undoped a-Si:H, the experimental results were limited thus far to data obtained on doped materials [2,4,5] in which a different distribution of recombination centers may exist [6,7]. In the present work we report the first determination of the above dependencies, in undoped a-Si:H, applying a combination of Metal-Oxide-Semiconductor (MOS) and PhotoCarrier Grating (PCG) configurations. Previously either the MOS configuration [8] or the PCG configuration [9] have been used for the study of phototransport parameters. The novel application of the combined configuration enables a simultaneous study of both the majority and minority carrier

phototransport properties as a function of  $\Delta E_s = E_c(s) - E_F$ , where  $E_c(s)$  is the energy of the conduction band edge at the semiconductor-oxide interface. In particular we are able to present the first simultaneous results of the dependencies of the light intensity exponents on  $\Delta E_s$ , and to show that these dependencies on  $\Delta E_s$  yield a more convincing proof for the "defect pool" recombination-centers model than "quantitative" fits of the theoretical predictions to the measured  $\mu\tau$  products [4]. Since the majority carriers in undoped a-Si:H are the electrons we define their light intensity exponent by the relation  $(\mu\tau)_e \propto G^{Y-1}$ , where  $(\mu\tau)_e$  is the electrons  $\mu\tau$  product and  $G$  is the carriers generation rate. Correspondingly for the holes, we define the exponent  $S$  by the relation  $(\mu\tau)_h \propto G^{-2S}$ . The main conclusion of the comparison of our experimental data with the presently available theoretical results is that the "defect pool" is the best description given thus far for the deep recombination-level distribution in a-Si:H. This conclusion applies for both undoped and slightly doped (a fraction of a ppm) a-Si:H.

## 2. THEORETICAL BACKGROUND

Following the many data which indicate the presence of three charged states of a dangling

bond [10], the presently accepted models of the deep states (i.e. the recombination centers) in a-Si:H do consider these states [2-4]. Correspondingly, the most common model used for interpreting the various data is the simplest possible model which is based on the presence of these states. In this model, known as the "standard" model [2-4] of a-Si:H, it is assumed that there are  $D^+$  and  $D^0$  dangling bond centers, the common energy level of which lies below  $E_F$ , and the  $D^-$  centers, the energy level of which lies above  $E_F$ . The most significant feature of this model is the correlated occupation statistics [11] of these states, i.e., that the occupations of the  $D^+$  and  $D^0$  centers also determine the occupation of the  $D^-$  centers. Very recently a numerical study of the "standard" model [3] has shown that in undoped a-Si:H,  $(\mu\tau)_e$  will increase with decreasing  $\Delta E$ , while  $(\mu\tau)_h$  will decrease with  $\Delta E$ . It was further found [3] that  $\gamma$  decreases from 1 to 1/2 with decreasing  $\Delta E$ , while  $S$  is independent of  $\Delta E$  having the value  $S = 0$ . Qualitatively these results are the same as those expected for a single recombination level in general [12,13] and for parameters which are appropriate for a-Si:H in particular [2]. It is important to note that the  $S=0$  prediction is independent of the particular parameters chosen for the above two models [13].

The more recently suggested model for a-Si:H is the so-called "defect pool" model in which one assumes three independent "sets" of levels, so that each set consists of a  $D^0/D^+$  level and a  $D^-$  level [6]. Thus far predictions based on this model were made [4] for the  $\Delta E$  dependencies of  $(\mu\tau)_e$  and  $(\mu\tau)_h$ , but not for  $\gamma$  and  $S$ . We argue however here that while  $\gamma$  will have qualitatively the same  $\Delta E$  dependence as in the "standard" model, it is very likely that in the "defect pool" model  $S$  has a non-zero value which decreases with  $\Delta E$ . Basically, the argument is based on the very simple picture [12] of the single recombination-center level. In this picture the variation of  $\gamma$  with increasing  $\Delta E$  is controlled by the charge neutrality condition which is fulfilled by the fact that the electron concentration is equal to the concentration of the positively charged deep recombination centers [12] ( $D^+$  centers in our

case). We argue [13], by symmetry, that the same condition holds for the holes and the negatively charged recombination centers ( $D^-$  centers in our case) provided (as assumed in the "defect pool" model) that no correlation exists between the occupation of the two types of centers [4]. Hence,  $S$  will vary in a way similar to  $\gamma$ , i.e. it will decrease from  $S = 1/4$  to  $S = 0$  with decreasing  $\Delta E$ . We find then that the  $S \neq 0$  observation is a signature of a system which has at least two occupation-independent levels. A more detailed discussion and the justification for considering recombination in the deep states rather than in the band tail states will be given elsewhere [13].

### 3. EXPERIMENTAL

The MOS structure used in the present study was almost the same as the one used previously [8,14] for the study of the photoconductivity and its dependence on  $\Delta E_s$  in a-Si:H. Since this structure has been described and discussed before, its description will not be repeated here. Let us mention only that our  $1\mu\text{m}$ -thick film of device-quality undoped a-Si:H has been deposited [15] using rf glow discharge decomposition of silane. The new experimental configuration which was used here was the application of the PCG technique to the MOS structure. We should point out that the common PCG measurement [9] actually yields the ambipolar diffusion length  $L$ , from which one derives  $(\mu\tau)_h$  using the well known relation [15] between them  $((\mu\tau)_h \propto L^2)$ . We can determine then both  $(\mu\tau)_e$  and  $(\mu\tau)_h$  as a function of  $\Delta E_s$ .

### 4. EXPERIMENTAL RESULTS AND DISCUSSION

Since the relation between the applied gate voltage,  $V_G$ , and  $\Delta E_s$  has been discussed in the past [8] we can scale  $V_G$ , which is in the range  $6 \geq V_G \geq -6\text{V}$ , with the band bending scale at the surface,  $\Delta E_s$ , which is in the range  $0.8 \geq \Delta E_s \geq 0.5\text{eV}$ . We note that it is essentially the forward bias ( $V_G > 0$ ) range which yields this variation [8,13]. An independent experimental proof for the above  $V_G-\Delta E_s$

scaling is derived from the fact that the presently found variation of  $\gamma$  between 1 and 0.5 (see below) with the above variation of  $V_G$  is in excellent agreement with the predictions made for this parameter in all the available theories [1-3] and all the available experimental results which either used doped materials [1,2] (i.e. the  $\gamma$  dependence on  $\Delta E$ ) or the MOS configuration [8,14] (i.e. the  $\gamma$  dependence on  $\Delta E_s$ ). Now that we have set the  $\Delta E = \Delta E_s$  scale we can compare our results with the predictions of the "standard" [3,4] and the "defect pool" [4] models.

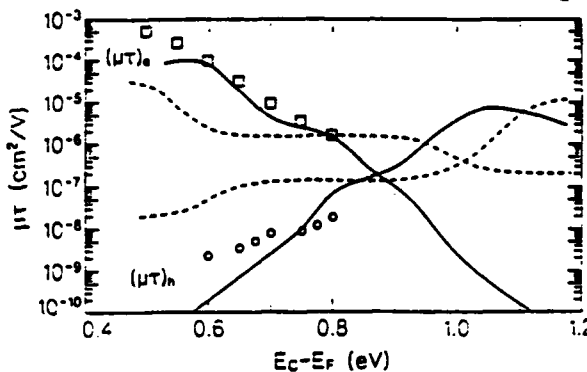


Figure 1. The measured two carriers  $\mu\tau$  products as a function of  $\Delta E_s$ . The results are compared with the predictions of Ref. 4 for the "standard" model (dashed curves) and the "defect pool" model (full curves).

Our experimental results for the dependencies of  $(\mu\tau)_e$  and  $(\mu\tau)_h$  on  $\Delta E_s$  are shown in Figure 1. For comparison with the theoretical predictions we also show the calculated results for the above two models [4], for a defect concentration of  $10^{15} \text{ cm}^{-3}$ . It is seen that the measured dependence of  $(\mu\tau)_e$  on  $\Delta E_s$  is in a much better agreement with the "defect pool" model than with the "standard" model predictions. By examining other "standard" model predictions [3] it appears that this conclusion goes beyond the choice of the parameters used in the calculations, since the  $(\mu\tau)_e$  dependence on  $\Delta E_s$  is much sharper for the "defect pool" model. On the other hand we see that the dependence of  $(\mu\tau)_h$  is in better

qualitative agreement with the "standard" model. These two behaviors indicate clearly that the true situation is more complicated than the "standard" model i.e. that there is at least a partial occupation-independence of the recombination levels involved (see below). We must note however that the agreement of the  $(\mu\tau)_e/(\mu\tau)_h$  value with the "defect pool" model prediction is simply a consequence of the parameters chosen, as can be seen from the predictions for the "standard" model when different parameters have been used [3]. Hence, while the agreement with the "defect pool" predictions is better, in view of the lack of parameter-effect-analysis it is not too convincing. An important observation is the fact that the present results are almost identical with the results obtained by variation of  $\Delta E$  by doping [4,5,16]. This has three consequences. First, it lends further support to our  $\Delta E_s = \Delta E$  scaling. Second, the slight doping necessary to move  $E_F$  from  $E_F - 0.8$  to  $E_F - 0.5$  eV does not yield a considerable change in the recombination level structure in comparison with the undoped material, and third (which is very important for the present experimental approach) the "vicinity to the surface" nature of the combined PCG-MOS configuration does not effect the results.

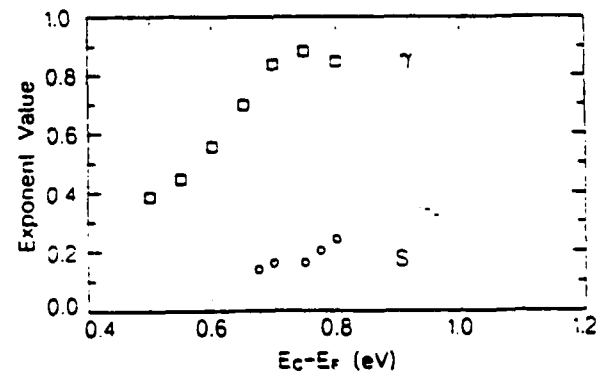


Figure 2. The measured light intensity exponent as a function of  $\Delta E_s$ .

In Figure 2 we show the  $\Delta E_s$  dependencies of the light intensity exponents. The results for  $\gamma$  in Figure 2 are in excellent agreement with those of previous experimental [8,14] and

theoretical [2,13] works on undoped a-Si:H, where  $\gamma$  was found to decrease quite sharply from  $\gamma \approx 1$  to  $\gamma \approx 0.4$  in the range of  $0.5 \leq \Delta E \leq 0.8$  eV.

So far all the data discussed above is consistent qualitatively with both the one level model [2,12] and the "standard" model [2,3] of a-Si:H. Let us turn then to the results of the  $S(\Delta E_s)$  dependence (reported here for the first time for undoped a-Si:H). As we see in Figure. 2,  $S$  decreases appreciably with decreasing  $\Delta E_s$ . This result is in agreement with the experimental finding of the behavior of  $S$  when boron doping was used [16]. While these and the present experimental observations of the behavior of  $S$  are consistent, the variation of  $S$ , and its high non-zero value, are inconsistent qualitatively with the expectations implied [13] by the one level [12] or the "standard" [3] model (see above). Hence the one-level model and the "standard" model cannot account for the  $S$  data, and consequently we should consider the next model in complexity for a-Si:H, i.e. the "defect pool" model. This model, as discussed above (Sec. 2), is most likely to yield a non-zero value for  $S$ . Hence, the behavior of  $S$  is a much more convincing tool than the  $(\mu\tau)_e$  and  $(\mu\tau)_h$  results [4] for the determination of the recombination level structure in a-Si:H.

## 5. CONCLUSIONS

We have followed the variation of the four phototransport properties  $(\mu\tau)_e$ ,  $(\mu\tau)_h$ ,  $\gamma$  and  $S$  as a function of the energy separation,  $\Delta E_s$ , in undoped a-Si:H. We found that the qualitative  $S(\Delta E_s)$  dependence excludes the one level model or the "standard" model as representative models for the recombination level structure in a-Si:H while it does not exclude the validity of the "defect pool" model. This conclusion is further supported by the better agreement of the  $\Delta E_s$  dependencies of  $(\mu\tau)_e$  and  $(\mu\tau)_h$  with the calculated predictions of the "defect pool" model.

**AKNOWLEDGEMENT:** This work was supported in part by the U.S.-Israel Binational Science Foundation, in part by NSF EPSCoR

Grant No. EHR-9108775, and in part by U.S.ARO Grant No. DAALO3-89-G-114. The authors are indebted to Dr. A. Catalano and Mr. J. Kane for the a-Si:H film deposition, and to Prof. J. Shappir for the oxidation of the crystalline silicon substrates.

## REFERENCES

1. M. Hack, S. Guha and M. Shur, Phys. Rev. B, 30 (1984) 6991.
2. D. Jousse, C.C. Chaussat, F. Vaillant, J.C. Bruyere and F. Lesimple, J. Non Cryst. Solids, 77&78 (1985) 627, and F. Vaillant and D. Jousse, Phys. Rev. B, 34 (1986) 4088.
3. E. Morgado, Mat. Res. Soc. Symp. Proc., 258 (1992), 765.
4. G.H. Bauer, G. Schumm and C.D. Abel, Proc. of the 6th Intl. Photovoltaic Science and Engineering Conf., B.K. Das and S.N. Singh (eds.), (Oxford & IBH, New Delhi, 1992), p. 443.
5. J. Kocka, C.E. Nebel and C.D. Abel, Phil. Mag. B, 63 (1991) 221.
6. H.M. Branz, Phys. Rev. B, 39 (1989) 5107, and H.M. Branz and M. Silver, Mat. Res. Soc. Symp. Proc., 192 (1990) 261.
7. K. Pierz, W. Fuhs and H. Mell, Phil. Mag. B, 63 (1991) 123.
8. T. Kagawa, N. Matsumoto and K. Kumabe, Phys. Rev. B, 28 (1983) 4570.
9. For a review see, I. Balberg, Mat. Res. Soc. Symp., 258 (1992) 693.
10. J. Ristein, J. Hautala and P.C. Taylor, J. Non Cryst. Solids, 144 (1988) 444.
11. D. Adler and E.J. Yoffa, Phys. Rev. Lett., 36 (1976) 1197.
12. A. Rose Concepts in Photoconductivity and Allied Problems. Wiley, New York, 1963, p. 22.
13. I. Balberg, unpublished.
14. H. Kakinuma, Phys. Rev. B, 39 (1989) 10473.
15. Y.-M. Li, B.F. Fiesellmann and A. Catalano, Proc. of the XXII PVSC IEEE, New York, 1991, p. 1231.
16. L. Yang, A. Catalano, R.R. Arva and I. Balberg, Appl. Phys. Lett., 57 (1990) 908.

## Study of the density of states in a-Si:H using the Si/electrolyte system

A. Many<sup>a</sup>, Y. Goldstein<sup>a</sup>, S.Z. Weisz<sup>b</sup>, J. Penalbert<sup>b</sup>, W. Munoz<sup>b</sup> and M. Gomez<sup>b</sup>

<sup>a</sup>Racah Institute of Physics, The Hebrew University, Jerusalem 91904, Israel.

<sup>b</sup>Department of Physics, University of Puerto Rico, Rio Piedras, PR 00931.

Localized states in a-Si:H are studied by pulsed measurements on the a-Si:H/electrolyte (S/E) system. The S/E interface is essentially blocking to current flow and, as a result, surface space-charge layers, ranging from large depletion to very strong accumulation conditions, can be induced and studied. Measurements in the depletion range under illumination yield directly the total density of occupied states in the entire energy gap. This is useful in obtaining a quick and reliable assessment of the quality of the amorphous films. In high-grade films we find that the total density of occupied states is around  $10^{18} \text{ cm}^{-3}$ . The data in the accumulation range, on the other hand, provide useful information on unoccupied states near the conduction band edge. The S/E system is utilized also to apply a sweep-out technique for an accurate determination of  $\mu\tau$ , the product of the electron mobility and lifetime, even when this value is very low.

### 1. INTRODUCTION

Considerable effort has been devoted to derive the density of states spectra in a-Si:H films [1]. In this paper use is made for this purpose of pulse measurements on the semiconductor/electrolyte (S/E) system. Such measurements, which proved to be very useful in the study of crystalline semiconductors [2], have been found to be equally effective when applied to a-Si:H films. The blocking nature of the S/E interface allows one to induce by an applied bias space-charge layers at the a-Si:H surface, ranging from large depletion to very strong accumulation conditions. In this manner, the entire energy gap in the space charge region, together with its localized states, can be swung below and above the Fermi level. At the same time, one can measure the surface space-charge density  $Q_{sc}$  as a function of the barrier height  $V_s$ . In a-Si:H,  $Q_{sc}$  resides predominantly in the localized states (except in strong accumulation conditions), so that the measurements yield, at least in principle, the energy distribution of the density of states.

High-grade, device-quality films are usually close to intrinsic (resistivity  $\sim 10^{10} \text{ ohm-cm}$ ). Such high-resistivity films cannot be

handled by our measurement technique because the surface space-charge capacitance cannot be charged within the short-duration applied pulse biases. Accordingly, most of the results to be reported here have been obtained under illumination, for which the photo resistivity is typically  $10^5 \text{ ohm-cm}$  or less. Our results in the depletion range are in remarkably good agreement with the theoretical curve that takes into account the presence of localized states. The data thus yield directly the total density of occupied states in the entire energy gap. This is very useful in obtaining a quick and reliable assessment of the quality of the amorphous films. In high-grade materials we find that the total density of occupied states is around  $10^{18} \text{ cm}^{-3}$ . The results in the accumulation range, on the other hand, provide useful information on the unoccupied states near the conduction-band edge. Analysis of the data in this case, however, is more difficult because surface states are apparently also involved.

The blocking nature of the a-Si:H/electrolyte interface is utilized also to apply a sweep-out technique for an accurate determination of  $\mu\tau$ , the product of the electron mobility and lifetime. The technique is effective over a very wide range of  $\mu\tau$ . In a rather poor-quality film, for example, we have measured a

$\mu\tau$  value as low as  $5 \times 10^{-8} \text{ cm}^2/\text{V}$ .

## 2. EXPERIMENTAL

Device quality a-Si:H films were prepared by rf glow-discharge decomposition of silane. First, a thin  $n^+$  layer was deposited on a conducting glass substrate, followed by a  $1 \mu\text{m}$  thick intrinsic film. The  $n^+$  layer provides an ohmic contact between the conducting glass and the intrinsic film. The conducting glass was cut into squares of about  $0.5 \text{ cm}^2$  in area and a contact attached to the conducting glass. The wire lead, contact area and the entire sample were masked by epoxy cement, except for a small area ( $\sim 2 \text{ mm}^2$ ) of the film's surface to be exposed to the electrolyte. The sample and a platinum electrode were immersed in an indifferent electrolyte such as  $\text{Ca}(\text{NO}_3)_2$  or  $(\text{NH}_4)_2\text{SO}_4$ . The sample was illuminated through the (transparent) electrolyte by a  $\sim 2 \text{ mW He-Ne laser}$ . The measurement technique has been described elsewhere [2], and will be reviewed only briefly here. A short ( $0.1-40 \mu\text{sec}$ ) voltage pulse applied between the Pt and the sample is used to charge up the semiconductor space-charge capacitance. The voltage drop across these electrodes, measured just after the termination of the pulse, represents to a very good approximation the change  $\delta V_s$  in barrier height across the film's space-charge layer induced by the applied pulse. The change  $\delta Q_{sc}$  in space-charge density is obtained from the voltage developed across a series capacitor, again at the termination of the pulse. Pulses of varying amplitude are applied singly, one per data point taken. In this manner damage to the amorphous film is minimized. We found that applying a large number of pulses degrades the material, drastically reducing its resistivity and introducing large trap densities.

The quiescent barrier height  $V_{so}$  is determined quite accurately (to within  $20 \text{ meV}$ ) from measurements in the depletion range. The entire  $Q_{sc}$  vs.  $V_s$  curve can then be constructed, on the basis of the  $\delta Q_{sc}$  vs.  $\delta V_s$  data [2]. In what follows the surface electron density  $N_s = Q_{sc}/q$ , where  $q$  is the electronic

charge, rather than  $Q_{sc}$ , is plotted against  $V_s$ .

The dark and photo resistance of each sample (between the a-Si:H/electrolyte interface and the  $n^+$  contact) was derived from current-voltage characteristics measured at the onset of the applied pulse, before the surface space-charge capacitance can be charged through the sample's resistance (see below). In this manner, the blocking interface is effectively shorted.

## 3. RESULTS AND DISCUSSION

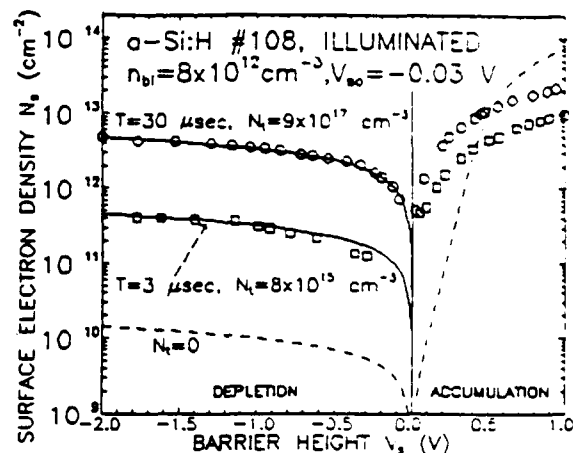


Figure 1. Surface electron density  $N_s$  vs. barrier height  $V_s$  in an illuminated sample of a-Si:H.

Typical results of  $N_s$  vs.  $V_s$ , obtained for an illuminated a-Si:H sample from measurements with a pulse of  $3\text{-}\mu\text{sec}$  (squares) and  $30\text{-}\mu\text{sec}$  (circles) duration, are displayed in the semilog plot of Fig. 1. In the depletion range ( $V_s < 0$ ), the  $N_s$  values are negative and, because of the logarithmic scale used, the plots are those of their absolute magnitudes. The free electron concentration under illumination  $n_{bi}$  in the amorphous film has been derived from the measured photoconductivity on the assumption that the electron mobility  $\mu$  is  $10 \text{ cm}^2/\text{Vsec}$  [3,4]. The corresponding theoretical dependence of  $N_s$  on  $V_s$ , as obtained from a solution of Poisson's equation in the absence of localized states, is shown by the dashed curve. The experimental points are seen to lie well above this curve indicating, as expected for amorphous films, that the space-charge layer in both the depletion and accumulation ranges is

dominated by localized states. Note that  $V_{SO}$  is, as expected, nearly zero since illumination tends to flatten the bands at the surface.

When a depletion layer is formed (by an applied negative pulse), free and trapped electrons are expelled from the surface region, leaving behind the positively-charged localized states that make up the immobile space-charge in the depletion layer. In an unilluminated sample only shallow states, down to 0.3-0.4 eV below the conduction band edge, are able to thermally emit their trapped electrons into the conduction band within the measurement time (the pulse duration) [2]. Under illumination, on the other hand, the situation is quite different. Hole-electron pairs are continuously generated by the light. The electrons are expelled from the surface region, while the holes are attracted to the surface where they can recombine with the trapped electrons. In this manner electrons in occupied states throughout the energy gap can be discharged and expelled from the space-charge layer, irrespective of the depth of the states. Referring to Fig. 1, we see that for a measurement time of 3  $\mu$ sec (squares) only a fraction of the trapped electrons are expelled, but when the pulse duration is extended to 30  $\mu$ sec (circles), practically all occupied states in the depletion layer are discharged and expelled (see below). The solid curves, passing in each case through the points, were calculated from Poisson's equation for the case in which localized states of densities  $N_l$  (as marked) are present. The agreement between theory and experiment is seen to be remarkably good, adding considerable confidence to our analysis. The total density of occupied states in the entire energy gap, as derived from the data for the 30  $\mu$ sec measurement time is about  $10^{18} \text{ cm}^{-3}$ , which is the expected value for the films studied.

When accumulation layers are formed, unoccupied states are filled up. Here again, the experimental points are seen to be initially well above the dashed curve calculated for the case of no localized states present, indicating that localized states dominate the space charge layer in this range as well. Surface states are probably also involved. At stronger accumulation,

however, the calculated curve crosses the experimental points and climbs above them. This is not understood at present, and more work is in progress to account for such a behavior. Further studies are needed also to distinguish between surface and bulk states.

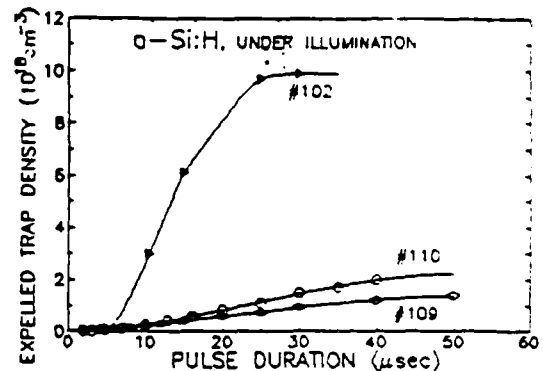


Figure 2. Expelled trap density vs. pulse duration (measurement time) for three a-Si:H samples under illumination.

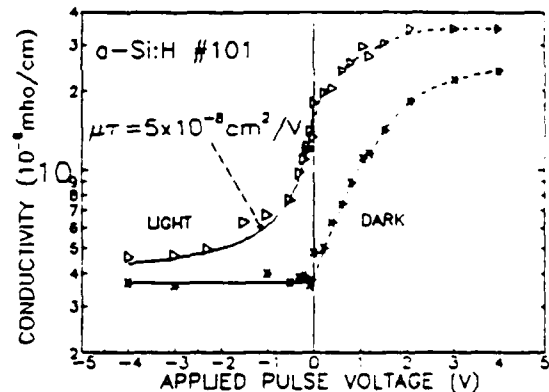


Figure 3. Dark and photo conductivity of a degraded a-Si:H sample vs. applied voltage pulse. Solid curve in the negative pulse range represents eq. (3) for  $\mu\tau = 5 \times 10^{-8} \text{ cm}^2/\text{V}$ .

The expelled trap density under depletion conditions, as derived from measurements such as those shown in Fig. 1, is plotted in Fig. 2 against pulse duration. The lower two curves were obtained for 2h-grade a-Si:H films, while the upper curve was obtained after a film has been degraded by the application of many

voltage pulses. In all cases, the expelled trap density increases with pulse duration, but tends to saturate at a pulse duration of 30-40  $\mu$ sec. We interpret the saturation level as representing the total density of occupied states in the energy gap. We are in the process of developing a model involving the hole trapping kinetics in order to account for the shape of the experimental curve.

The dark and photoconductivity of a degraded a-Si:H sample vs. applied pulse voltage is displayed in Fig. 3 on a semilog plot. The measurements were taken at the onset of the pulse, before the space-charge capacitance at the a-Si:H interface can charge up. For positive pulses (electrolyte positive with respect to the n+ contact), the conductivity in both the dark and under illumination is seen to increase with applied voltage. This is due to electron injection from the n+ layer. In the negative polarity, the dark conductivity is independent of voltage, as it should. The photoconductivity, on the other hand, is seen to decrease with pulse amplitude, approaching the dark conductivity at large negative voltages. We attribute this behavior to electron sweep-out by the applied fields, as shown by the following considerations. The continuity equation for the case of a blocking contact can be written as:

$$dN/dt = L - N/\tau - \mu EN/d, \quad (1)$$

where N is the total density of photo electrons in the sample per  $\text{cm}^2$ , L is the number of hole-electron pairs generated by the light per  $\text{cm}^2\text{sec}$ , E is the applied field and d is the film's thickness. Strictly speaking, the last term in eq. (1) should be  $\mu En_{bl}(d)$ , where  $n_{bl}(d)$  is the electron concentration at the n+ contact. For simplicity, we have replaced  $n_{bl}(d)$  by the average electron concentration  $N/d$ , which is a fairly good approximation. Space-charge effects are negligible in this polarity, even if all photo electrons are swept away from the sample (leaving behind the photogenerated holes). Hence the field is very nearly uniform at the value  $V/d$ . Solution of eq. (1), with the boundary condition that N assumes the zero-field density  $N_0 = L\tau$  at the onset of the pulse ( $t = 0$ ), yields

$$N = N_0 / (1 + \mu\tau E/d) + N_0 \exp[-(1/\tau + \mu E/d)t] / (1 + d/\mu\tau E). \quad (2)$$

Now  $d/\mu E$  is the electron transit time through the film and is typically  $10^{-8}$  sec for an applied voltage of 1 V. The measurement is taken about 1  $\mu$ sec following the pulse onset, so that the second term in eq. (2) can be neglected to a very good approximation. Re-writing eq. (2) in terms of the photoconductivity  $\sigma = q\mu N/d$  we then have

$$\sigma = \sigma_0 / (1 + \mu\tau V/d^2). \quad (3)$$

The solid curve fitted to the photoconductivity data at negative voltages in Fig. 3 is a plot of eq. (3) for  $\mu\tau = 5 \times 10^{-8} \text{ cm}^2/\text{V}$ . The fit with the experimental points is seen to be very good. The rather low value of  $\mu\tau$  is reasonable for the degraded sample used in the measurement. The method can be applied effectively even if  $\mu\tau$  is an order of magnitude lower. It should be noted that  $\mu$  in this context is the trap-controlled mobility [4].

#### ACKNOWLEDGMENTS.

The authors are indebted to Dr. A. Catalano for providing the a-Si:H samples. Special thanks are due to Prof. I. Balberg for many helpful discussions. This work was supported in part by the National Science Foundation EPSCoR grant EHR-9108775 and in part by the U.S. Army Research Office grant No. DAAL03-89-G-0114.

#### REFERENCES

1. See, for example, A. Madan and M.P. Shaw, Mat. Res. Soc. Symp. Proc. 258 (1992).
2. M. Wolovelsky, J. Levy, Y. Goldstein, A. Many, S.Z. Weisz and O. Resto, Surf. Sci. 171, 442 (1986).
3. D. Goldie, P.G. LeComber and W.E. Spears, Mat. Res. Soc. Symp. Proc. 119, 489 (1988).
4. T. Tiedje and A. Rose, Solid State Commun. 37, 48 (1981); E.A. Schiff and M. Silver in *Amorphous Silicon and Related Materials*, H. Fritzsche, Ed. (World Scientific, Singapore, 1988), p. 825.

## MOBILITY-LIFETIME PRODUCTS IN GLOW DISCHARGE AND RF SPUTTER DEPOSITED a-Si:H

M. H. Faras,<sup>\*</sup> A. Roche,<sup>\*</sup> S. Z. Weisz,<sup>\*</sup> H. Jia,<sup>†</sup> J. Shinar,<sup>†</sup> Y. Lubianiker,<sup>‡</sup> and I. Balberg<sup>‡</sup>

<sup>\*</sup>Department of Physics, University of Puerto Rico, Rio Piedras, PR 00931

<sup>†</sup>Ames Laboratory - USDOE and Department of Physics and Astronomy,  
Iowa State University, Ames, Iowa 50011

<sup>‡</sup>Racah Institute of Physics, Hebrew University, Jerusalem, 91904, Israel

### ABSTRACT

A comparative study of the deposition temperature ( $T_d$ ) dependence of the mobility-lifetime ( $\mu\tau$ ) products of the charge carriers in glow-discharge and rf sputter-deposited a-Si:H is described and discussed. The  $T_d$ -dependence of the  $\mu\tau$ s and the majority carrier light-intensity exponents of the two types of films are strikingly similar. These observations then lead to the conclusion that the structure of the recombination levels and the recombination processes are in accord with the "defect pool" model, in contrast to previous suggestions. The differences between the two types of films thus appear to be limited to the concentrations of dangling bonds.

### INTRODUCTION

Various techniques for depositing a-Si:H have been studied over the years, some of which were claimed to yield higher quality films than others [1]. The glow discharge (GD) decomposition of silane has been exhaustively investigated, and most of the applications employ this deposition method [2]. The study of films deposited by other techniques was usually limited to the description of their measurable properties and the comparison of these properties with those of undoped "device-quality" GD films [3]. All of the theoretical progress, devoted to the understanding of the electronic structure of a-Si:H, was achieved by comparing the theoretical predictions with the experimental results on GD films [4-9]. The question of whether the phototransport data on material produced differently indicate different electronic structures, transport mechanisms, or recombination processes has been addressed only rarely. One such study of the phototransport data associated with the majority carriers in GD and rf sputtered (RFS) was reported by Jousse et al. [10], who monitored the effects of boron doping on the phototransport parameters. They concluded that in RFS materials the recombination process is controlled only by the valence bandtail, but in GD films the recombination involves a defect center with either a single or two positively correlated energy states. This paper reexamines these conclusions in view of new phototransport data and the recent theoretical developments [6,9] in understanding the behavior of the minority carrier phototransport properties in GD device-quality material [6-9]. RFS films were of course extensively studied [11], and in contrast to GD deposition, enable a  $T_d$ -independent control of hydrogen incorporation.

The results on two sets of samples, a GD and an RFS deposited set are described in this paper. The variable deposition parameter used to obtain sequential films with continuously varying properties in both sets was  $T_d$ . Indeed, this parameter has been employed extensively for numerous purposes, e.g., in finding correlations between various structural [13] and/or electronic properties [3]. This parameter was conspicuous in establishing the relation between the deep states density and the width of the valence bandtail in GD a-Si:H [14]. In addition, it is probably the most convenient variable deposition parameter, and its effect on the films is

conceptually very clear and uncontested: A higher  $T_s$  enhances the "order" and density of the distorted tetrahedral network on the one hand [13] and the effusion of the hydrogen on the other hand [14]. Since the former process improves the transport and the passivation of the dangling bonds while the latter increases their density, it is not surprising that the charge carrier lifetimes peak around  $T_s \approx 250^\circ\text{C}$ . However, the details of the dynamical processes and their dependence on the substrate temperature are obviously complex. For example, the relative roles of  $T_s$  in hydrogen diffusion [17] and incorporation [18] are still unsettled. Similarly, its direct effect on the network relaxation and indirect effect on the relaxation via hydrogen effusion [19] are also not well understood. This paper, which is devoted to phototransport data, makes no attempt to correlate the data with the structural properties of the materials since the transport properties of semiconductors are very sensitive to small variations in the structural and compositional details of the material. Hence, a very comprehensive study will be needed in order to discuss that correlation. However, the basic nature of the recombination mechanism does not have to depend on those details. This basic mechanism is the subject of this paper.

## EXPERIMENTAL PROCEDURE

The GD films that were deposited at Solarex [21] at  $250^\circ\text{C}$  and at a typical deposition rate of  $4 \text{ \AA/s}$  onto Corning 7059 glass substrates were  $\sim 5000 \text{ \AA}$  thick. The RFS films prepared at the Ames Laboratory [22] were deposited by sputtering a 6" diameter polycrystalline Si target located  $\sim 1.5$ " above the heated substrate at  $13.56 \text{ MHz}$  and an rf power of  $400 \text{ W}$ . The partial pressures of the Ar and  $\text{H}_2$  gases were  $10$  and  $1 \text{ mT}$ , resp. The thickness and deposition rates of the films ranged from  $0.8$  to  $1.5 \mu\text{m}$  and  $1.5$  to  $2.9 \text{ \AA/s}$ , resp. The contacts were coplanar  $\text{NiCr}$  or  $\text{Au}$  contacts separated by  $0.4 \text{ mm}$ . While the optoelectronic properties of GD films barely change upon annealing at  $250^\circ\text{C}$  [16], those of the RFS samples, which were annealed at that temperature in air for  $2 \text{ h}$ , indeed improved.

The phototransport properties were studied by the photocarrier grating (PCG) technique [23-25] using a  $\text{H}_2\text{-Ne}$  laser, i.e., with illumination that can be considered to be "uniformly" absorbed in the films. The results were obtained under ambipolar conditions [24] so the minority carrier (hole) mobility-lifetime product  $(\mu\tau)_h$  could be derived directly from the measured ambipolar diffusion length  $L$  via the relation

$$(\mu\tau)_h = (q/2kT)L^2. \quad (1)$$

The majority carrier (electron)  $(\mu\tau)_e$  product was derived directly from the measured photoconductivity  $\sigma_{ph}$  and the relation

$$(\mu\tau)_e = \sigma_{ph}/(qG) \quad (2)$$

where  $G$ , the photogeneration rate of electron-hole pairs, was determined by assuming unit quantum efficiency of generation by the absorbed photons. As mentioned above, however, the most significant parameters for interpretation of the data are the so-called light intensity exponents [26], defined by the relations

$$(\mu\tau)_e \propto G^{\gamma-1} \quad (3)$$

$$(\mu\tau)_h \propto G^{-2\beta}. \quad (4)$$

The  $\mu\tau$  results shown below were obtained at  $10 \text{ mW/cm}^2$  illumination, and the exponents were derived from the behavior in the  $0.8$  -  $10 \text{ mW/cm}^2$  range. The analysis of these data was described in previous reports [20,23].

conceptually very clear and uncontested: A higher  $T_s$  enhances the "order" and density of the distorted tetrahedral network on the one hand [13] and the effusion of the hydrogen on the other hand [14]. Since the former process improves the transport and the passivation of the dangling bonds while the latter increases their density, it is not surprising that the charge carrier lifetimes peak around  $T_s \approx 250^\circ\text{C}$ . However, the details of the dynamical processes and their dependence on the substrate temperature are obviously complex. For example, the relative roles of  $T_s$  in hydrogen diffusion [17] and incorporation [18] are still unsettled. Similarly, its direct effect on the network relaxation and indirect effect on the relaxation via hydrogen effusion [19] are also not well understood. This paper, which is devoted to phototransport data, makes no attempt to correlate the data with the structural properties of the materials since the transport properties of semiconductors are very sensitive to small variations in the structural and compositional details of the material. Hence, a very comprehensive study will be needed in order to discuss that correlation. However, the basic nature of the recombination mechanism does not have to depend on those details. This basic mechanism is the subject of this paper.

## EXPERIMENTAL PROCEDURE

The GD films that were deposited at Solarex [21] at  $250^\circ\text{C}$  and at a typical deposition rate of  $4 \text{ \AA/s}$  onto Corning 7059 glass substrates were  $\sim 5000 \text{ \AA}$  thick. The RFS films prepared at the Ames Laboratory [22] were deposited by sputtering a 6" diameter polycrystalline Si target located  $\sim 1.5$ " above the heated substrate at  $13.56 \text{ MHz}$  and an rf power of  $400 \text{ W}$ . The partial pressures of the Ar and  $\text{H}_2$  gases were  $10$  and  $1 \text{ mT}$ , resp. The thickness and deposition rates of the films ranged from  $0.8$  to  $1.5 \mu\text{m}$  and  $1.5$  to  $2.9 \text{ \AA/s}$ , resp. The contacts were coplanar NiCr or Au contacts separated by  $0.4 \text{ mm}$ . While the optoelectronic properties of GD films barely change upon annealing at  $250^\circ\text{C}$  [16], those of the RFS samples, which were annealed at that temperature in air for  $2 \text{ h}$ , indeed improved.

The phototransport properties were studied by the photocarrier grating (PCG) technique [23-25] using a He-Ne laser, i.e., with illumination that can be considered to be "uniformly" absorbed in the films. The results were obtained under ambipolar conditions [24] so the minority carrier (hole) mobility-lifetime product  $(\mu\tau)_h$  could be derived directly from the measured ambipolar diffusion length  $L$  via the relation

$$(\mu\tau)_h = (q/2kT)L^2. \quad (1)$$

The majority carrier (electron)  $(\mu\tau)_e$  product was derived directly from the measured photoconductivity  $\sigma_{ph}$  and the relation

$$(\mu\tau)_e = \sigma_{ph}/(qG) \quad (2)$$

where  $G$ , the photogeneration rate of electron-hole pairs, was determined by assuming unit quantum efficiency of generation by the absorbed photons. As mentioned above, however, the most significant parameters for interpretation of the data are the so-called light intensity exponents [26], defined by the relations

$$(\mu\tau)_e \propto G^r \quad (3)$$

$$(\mu\tau)_h \propto G^{-2s} \quad (4)$$

The  $\mu\tau$  results shown below were obtained at  $10 \text{ mW/cm}^2$  illumination, and the exponents were derived from the behavior in the  $0.8$  -  $10 \text{ mW/cm}^2$  range. The analysis of these data was described in previous reports [20,23].

## RESULTS

Figure 1(a) displays the well-known behavior of  $(\mu\tau)_e$  in GD a-Si:H [10,14]. It increases significantly with increasing  $T_s$  up to  $\sim 200^\circ\text{C}$ , and decreases considerably at  $T_s \geq 300^\circ\text{C}$ . The behavior of  $(\mu\tau)_h$  is similar (Figure 1(b)), but it decreases at  $T_s \geq 350^\circ\text{C}$ . The behavior of  $\gamma$  (Figure 1(c)) appears to be correlated with  $(\mu\tau)_e$  in some ranges of  $T_s$ , but anticorrelated to it in other ranges of the deposition temperature. On the other hand, the behavior of  $S$  (Figure 1(d)) appears to be anticorrelated with  $(\mu\tau)_h$  over the entire range of  $T_s$ .

Due to their poor photoconductivity,  $(\mu\tau)_h$  of the as-deposited RFS films could not be measured by the PCG technique. Although  $\sigma_{ph}$  improved after annealing, it was still insufficient to enable the determination of  $S$  (Eq. (4)), which required attenuated illumination. Figure 2(a) displays the dependence of  $(\mu\tau)_e$  on  $T_s$ ; it is strikingly similar to the dependence in GD films (Fig. 1(a)). On the other hand, the peak of  $(\mu\tau)_h$  vs  $T_s$  is much narrower peak in the RFS samples than in the GD films. The behavior of  $\gamma$  (Figure 2(c)) is interesting. A priori the behavior of the annealed films appears to be anticorrelated with that of the unannealed. However, comparison with  $\gamma(T_s)$  of the GD films (Fig. 1(c)) indicates that all of the  $T_s$  dependences can be matched by appropriate displacements along the  $T_s$  axis. This approach is adopted in analysing and interpreting the results.

## DISCUSSION AND CONCLUSIONS

As mentioned above, the general qualitative dependence of  $\mu\tau$  on  $T_s$  is well understood: At low  $T_s$ , two factors are responsible for the high defect concentration and consequent short lifetime of both types of charge carriers: (i) H diffusion during deposition is too slow to passivate many of the dangling bonds and (ii) the bandtails are broad, due to the unrelaxed network, which yields shallower recombination centers [14]. At high  $T_s$ , hydrogen effusion increases the density of dangling bonds [14,15] and may also lower the network order [19] which is improved by its incorporation. These effects are confirmed by various measurements [14], notably the constant photocurrent method (CPM) [3]. Hence, the results on the GD films shown in Figs. 1(a) and 1(b) can be understood simply within this picture. The detailed behavior of  $(\mu\tau)_e$  at  $180 \leq T_s \leq 300^\circ\text{C}$  can be attributed to the competition between the competing processes. This may also explain the variations in the  $(\mu\tau)_e$  behavior in films deposited under different conditions [3].

While the  $\mu\tau$  behavior cannot disclose more specific information on the basic recombination mechanism, the light intensity exponents  $\gamma$  and  $S$  (as shown for photoconductors in general [26] and for a-Si:H in particular [9,20]) can. Turning to the former, we see that  $\gamma \geq 0.9$ . "The Rose model" of bandtail recombination [26] does not allow  $\gamma > 1$ , and suggests that the characteristic width of the exponential conduction bandtail is given by

$$E_{co} = [\gamma/(1 - \gamma)]kT. \quad (5)$$

If recombination occurs only in the bandtail states  $1 \geq g \geq 0.9$  implies that  $E_{co} \geq 0.2 \text{ eV}$ . This width is far larger than any previous, more direct estimate of  $E_{co}$  ( $\approx 25 \text{ meV}$ ). Indeed, application of the "Rose model" [26] for a-Si:H led to the conclusion that the recombination occurs not in a bandtail but in a deep localized state [27]. Another interpretation of the the Rose model was suggested for the recombination dominating the minority carriers (holes) [28]. In

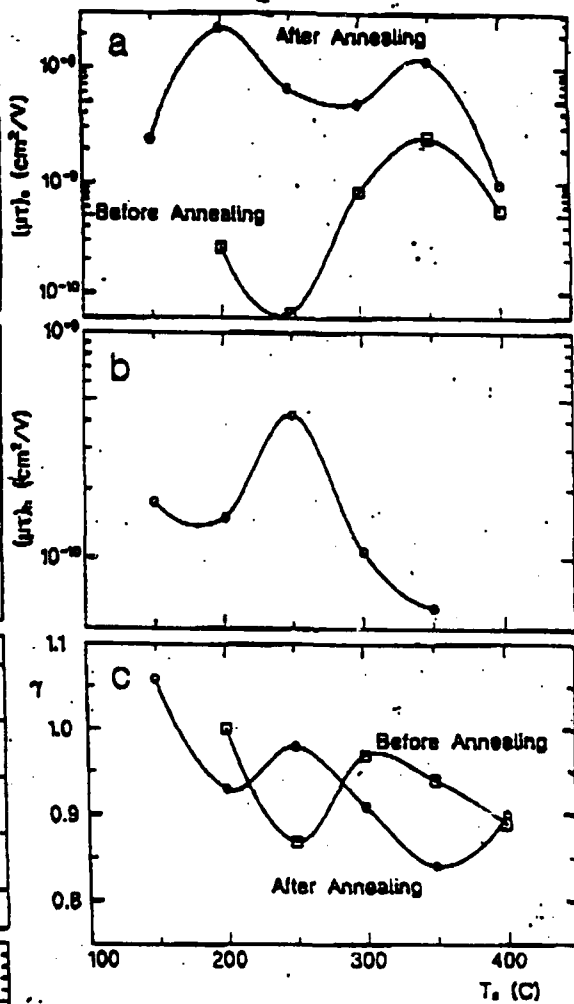
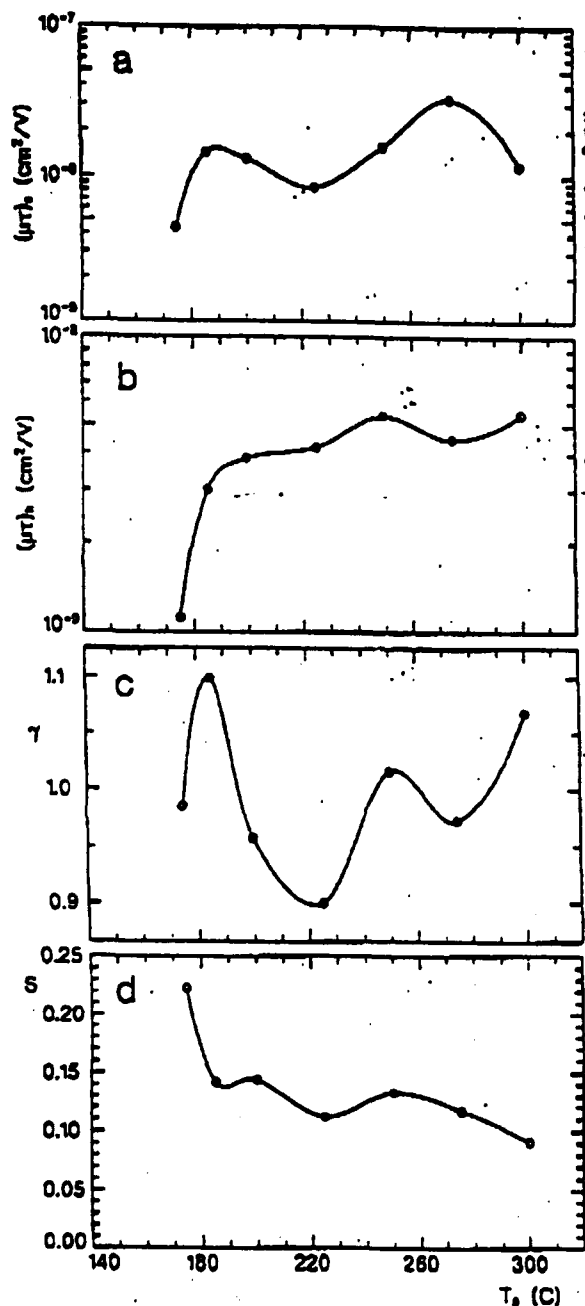


Figure 2. The deposition temperature  $T_d$  dependence of the phototransport parameters of the rf sputter-deposited films: The mobility-lifetime  $\mu\tau$  product of the electrons (a) and holes (b), and the dependence of the light intensity exponents  $\gamma$  (c) (see eq. (3)).

Figure 1. The deposition temperature  $T_d$  dependence of the phototransport parameters of the GD films: The mobility-lifetime  $\mu\tau$  product of the electrons (a) and holes (b), and the corresponding dependences of the light intensity exponents  $\gamma$  (c) and  $S$  (d) (see eqs. (3) and (4)).

this case the model yields

$$E_{vo} = [(1 - 2S)/2S]kT. \quad (6)$$

Unlike the case of  $E_{co}$ , the values shown in Fig. 1(d) are not in sharp contrast with our knowledge of  $E_{vo}$  [3]. For example, for  $S = 0.15$  we get  $E_{vo} = (7/3)kT$  at room temperature. However, this model is still inappropriate since  $S$  decreases (i.e.,  $E_{vo}$  increases) as  $T_d$  increases from 200 to 300°C, while CPM data clearly indicate a narrowing valence bandtail [3,14]. The increasing  $E_{vo}$  also sharply contrasts with the above picture of enhanced network order at higher  $T_d$ .

The foregoing discussion leads to an interpretation in terms of deep recombination centers which, in a-Si:H, must consist of various dangling bonds. The simple single recombination level model is easily ruled out in the range  $\gamma > 1$ , since these values require at least two levels, the occupation of which is a priori uncorrelated [26]. For  $\gamma < 1$  the results shown in Fig. 1(c) can indeed be interpreted as due to a single level. However, Fig. 1(d) rules this out since a single level system was shown to yield  $S = 0$  [9]. For a-Si:H it is reasonable to consider the correlated occupancy or "standard" model of dangling bonds [5,7,10] which assumes a singly ( $D^0$ ) or unoccupied ( $D^+$ ) level lying below the Fermi level  $E_F$  and a doubly occupied ( $D^-$ ) level above  $E_F$ . The correlated occupancy of these levels was recently argued to yield the same behavior as a single recombination level [9]. Indeed, the "standard" model [5] yields  $S = 0$  for this picture as well. In summary, while Figs. 1(a) - 1(c) are consistent with the "standard" model, Fig. 1(d) is not. Thus, another independently occupied level must be added to account for all of the results. One possibility is to add such a level to the "standard" model. Calculations which essentially consider the valence bandtail states as another recombination center indeed yielded positive values of  $S$  in accordance with Fig. 1(d) [7,8]. Yet these calculations yield  $S > 0$  only when  $\gamma > 1$  [8], in contrast to the data shown in Fig. 1(c) in the most interesting range of  $T_s$ , namely  $200 \leq T_s \leq 300^\circ\text{C}$ .

In contrast to the above models, the recent "defect pool" model of essentially uncorrelated dangling bond bands, where a  $D^-$  band lies below a  $D^0$  band which lies below a  $D^+$  band [5], is consistent with all of the data shown in Figs. 1(a) - 1(d). The uncorrelated nature of the bands enable  $S \neq 0$  values, while their number and energetic order relieve the correlation between  $\gamma > 1$  and  $S > 0$ . Indeed, for the light intensities used in this work the values of  $\gamma = 0.95$  and  $S = 0.18$  are to be expected from this model [6]. Therefore, the  $S > 0$  values exclude the earlier model [10] for GD material and show that the the "defect pool" model is to date the simplest which can account for all of the phototransport data.

The annealed RFS films (Fig. 2) exhibit close similarities with the GD samples (Fig. 1). In particular, the two-peak behavior of Figs. 1(a) and 2(a) indicates a similar electronic structure and recombination mechanism for electrons in the two types of a-Si:H. It is further interesting that the as-deposited  $(\mu\tau)_e$  values of the low- $T_s$  films are much lower than the values of the annealed or GD samples. On the other hand, the  $(\mu\tau)_e$  values of all the high- $T_s$  samples are close. This implies that for sufficiently high  $T_s$ , but lower than that yielding poor phototransport properties, the H content and network disorder are independent of the initial deposition process.

The behavior of  $(\mu\tau)_h$  in the RFS films is similar to that in the GD films around the peak at  $T_s = 250^\circ\text{C}$ , but that peak is much narrower in the RFS samples (Figs. 1(b) and 2(b)). If  $(\mu\tau)_h$  is controlled mainly by the  $D^-$  centers, then the results indicate that their content is more dependent on the deposition method than the density of the electron traps, which are presumably the  $D^0$  and  $D^+$  centers. The similar behavior of  $(\mu\tau)_e$  suggests that the  $\gamma$  values of the annealed RFS films (Fig. 2(c)) are essentially the same as those of the GD films (Fig. 1(c)) if the curves are shifted to match the  $\gamma > 1$  regions in the two types of samples. The  $\gamma > 1$  value of the RFS film at  $T_s = 150^\circ\text{C}$  again rules out the bandtail-only [10], the single recombination level, or the "standard" model without bandtails. For  $\gamma < 1$  the data are inconsistent with the "bandtail only" model (see above) but consistent with all of the other models in which the approach of  $E_F$  to the dominant recombination level (say, the  $D^0$ ) will decrease  $(\mu\tau)_e$  and increase  $(\mu\tau)_h$  and  $\gamma$ . However, the striking similarity of the  $T_s$ -dependence of  $(\mu\tau)_e$  and  $\gamma$  in the annealed RFS and GD films strongly suggests that the "defect pool" model is applicable to the annealed RFS films as well. In particular, the decreasing  $\gamma(T_s)$  from  $\gamma > 1$  and its detailed

behavior provide strong evidence for the similarity of the recombination processes in the two types of materials.

In conclusion, the  $T_g$ -dependence of the phototransport parameters of glow-discharge (GD) a-Si:H indicated the presence of at least two significant occupation-independent recombination levels. The results are consistent with the "defect pool" model. The closely similar behavior of the majority carrier phototransport parameters of GD and annealed rf sputter-deposited (RFS) films suggest similar recombination processes. The differences are apparently due to higher dangling bond contents as well as different relative densities of the various types of dangling bonds in the RFS films.

#### ACKNOWLEDGEMENTS

The authors are indebted to Dr. A. Catalano and Mr. G. Wood for the glow-discharge samples used in this study. This work was supported in part by NSF EPSCoR Grant No. EHR-9108775 and US ARO Grant no. DAAL03-89-6.00114. Ames Laboratory is operated by Iowa State University for the USDOE under Contract W-7405-Eng-82. This work was supported by the Director for Energy Research, Office of Basic Energy Sciences.

#### REFERENCES

1. *Amorphous Silicon Technology - 1992*, edited by M. J. Thompson, Y. Hamakawa, P. G. LeComber, A. Madan, and E. Schiff, *Mat. Res. Soc. Symp. Proc.* **258** (1992).
2. *J. Non Cryst. Sol.* **114** (1989).
3. A. H. Mahan et al., *J. Appl. Phys.* **69**, 6728 (1991).
4. H. M. Branz, *Phys. Rev. B* **39**, 5107 (1989).
5. E. Morgado, in ref. 1, p. 765.
6. G. Schumm, W. B. Jackson, and R. A. Street, *Phys. Rev. B* **48**, 14198 (1993).
7. F. Wang and R. Schwarz, *J. Appl. Phys.* **73**, 1082 (1993).
8. E. Morgado, *J. Non Cryst. Sol.*, in press.
9. I. Balberg, *J. Appl. Phys.* **xxx** (1994).
10. D. Jousse et al., *J. Non Cryst. Sol.* **77 & 78**, 627 (1985).
11. M. J. Thompson, in *The Physics of Hydrogenated Amorphous Silicon*, Vol. I, edited by J. Joannopoulos and G. Lucovsky (Springer, NY, 1984), Chapter 4.
12. M. Pinchasi, M. J. Kushner, and J. R. Abelson, *J. Appl. Phys.* **68**, 2255 (1990).
13. Y. Hishikawa et al., *Jpn. J. Appl. Phys.* **24**, 385 (1985).
14. M. Stutzmann, *Phil. Mag. B* **60**, 531 (1989).
15. A. H. Mahan et al., in *Amorphous Silicon Technology*, edited by A. Madan et al., *Mat. Res. Soc. Symp. Proc.* **149**, 539 (1989).
16. F. Wang and R. Schwarz, *J. Appl. Phys.* **71**, 791 (1992).
17. X. M. Tang, J. Weber, Y. Baer, and F. Finger, *Phys. Rev. B* **41**, 7945 (1990).
18. K. Winer, *Phys. Rev. B* **41**, 12150 (1990).
19. N. Maley and J. S. Lannin, *Phys. Rev. B* **36**, 1146 (1987).
20. I. Balberg and Y. Lubianiker, *Phys. Rev. B* **48**, 8709 (1993).
21. Y.-M. Li, B. F. Fieselmann, and A. Catalano, *Proc. of the XXII IEEE Photovoltaic Spec. Conf.* (IEEE, NY, 1991), p. 1231.
22. S. Mitra, K. K. Gleason, H. Jia, and J. Shinar, *Phys. Rev. B* **48**, 2175 (1993).
23. For a review of this technique, see I. Balberg in ref. 1, p. 693.
24. I. Balberg and S. Z. Weisz, *Appl. Phys. Lett.* **59**, 1726 (1991).
25. I. Balberg and S. Z. Weisz, *J. Appl. Phys.* **70**, 2204 (1991).
26. A. Rose, *Concepts in Photoconductivity and Allied Problems* (Wiley Interscience, NY, 1963).
27. D. Mendoza and W. Pickin, *Phys. Rev. B* **40**, 3913 (1989).
28. E. Souvain, J. Hubin, A. Shah, and P. Pipoz, *Phil. Mag. Lett.* **63**, 327 (1991).

Submitted to Symposium A

Symposium Title: Amorphous Silicon Technology - 1994

**EXCITING FREQUENCY-DEPENDENT RAMAN SCATTERING  
IN  $a\text{-Si}_{1-x}\text{C}_x\text{H}$  ALLOYS\***, Gerardo Morell, R.S. Katiyar, S.Z. Weisz,  
Department of Physics, University of Puerto Rico, San Juan, PR,  
00931, USA; and Isaac Balberg, The Racah Institute of Physics,  
The Hebrew University, Jerusalem 91904, Israel

We have measured the Raman spectra of  $a\text{-Si}_{1-x}\text{C}_x\text{H}$  alloys using three different frequencies of energies: 2.71, 2.41, and 2.14 eV. These alloys are characterized by their Tauc optical gap, that falls between 1.8 and 2.4 eV. As more carbon is incorporated into the  $a\text{-Si:H}$  matrix the width of the Si-Si TO band as well as the TA/TO band intensities ratio decrease indicating an increased order in the network. However, the degree of ordering in all samples is inhomogeneous. The surface layer is more disordered than the bulk, as can be concluded from the changes in the spectra of any given sample as a function of exciting energy. Spectra taken with the 2.14 eV line shows a systematically higher TO mode frequency of about  $5\text{ cm}^{-1}$  and a smaller width of about  $10\text{ cm}^{-1}$  than the ones measured with the 2.41 or 2.71 eV lines. Hydrogen dilution during the growth process is seen to have a limited effect on improving the degree of ordering in the alloys. Also, an intensity enhancement is observed in some samples that can be explained as a resonance effect.

\*Work supported in part by EPSCoR-NSF grant EHR-9108775 and by U.S. Army Research Office grant No. DAAL03-89-G-0114.

**Contact Author:**

Ram S. Katiyar  
University of Puerto Rico  
Department of Physics  
P.O. Box 23343  
San Juan  
Puerto Rico 00931  
USA  
Tel. (809) 751-4210  
Fax (809) 751-0625

**Co-Author:**

Isaac Balberg  
The Hebrew University  
The Racah Institute of Physics  
Jerusalem 91904  
Israel  
Tel. (972) 258-4676  
Fax (972) 258-4437

**Presenting Author:**

Gerardo Morell  
University of Puerto Rico  
Department of Physics  
P.O. Box 23343  
San Juan  
Puerto Rico 00931  
USA  
Tel. (809) 764-0000 ext.5187  
Fax (809) 751-0625

**Co-Author:**

Zvi Weisz  
University of Puerto Rico  
Department of Physics  
P.O. Box 23343  
San Juan  
Puerto Rico 00931  
USA  
Tel. (809) 767-0940  
Fax (809) 751-0625

## **Infrared and Raman Studies on a-Ge<sub>1-x</sub>Sn<sub>x</sub>:H Thin Films**

**E. Ching-Prado, R.S. Katiyar, W. Muñoz, O. Resto, and S.Z. Weisz**

**Department of Physics, University of Puerto Rico**

**Rio Piedras, P.R. 00931 USA**

### **Abstract**

Infrared and Raman measurements were carried out on a-Ge<sub>1-x</sub>Sn<sub>x</sub>:H thin films grown on Si substrates. The hydrogen concentration is found to decrease with increasing tin content. Preferential formation of monohydride groups (GeH) is observed with increasing Sn concentration. Tin dependence of the GeH and GeH<sub>2</sub> stretching modes are explained due to the lower electronegativity of Sn in comparison to that of Ge. The study reveals that the stability-ratio electronegativity of germanium must be revised or its value should be smaller than 3.59 for the a-Ge:H system. Also, the GeH wagging and GeH<sub>2</sub> roll modes show that there is a large bond angle variation with increasing Sn concentration. Additionally, the changes in the frequency, width and intensity of the Ge-Ge(TO) like phonon, clearly indicate that the structural disorder increases with increasing tin content. Auger electron microprobe and Raman study with different excitation laser lines show differences near the surface in comparison to the bulk, which is produced by the partial segregation of tin atoms, formation of Sn-clusters in the surface, and reduction of the germanium concentration near the surface, as well as preferential attachment of hydrogen to Ge than to Sn.